

IDŐJÁRÁS

QUARTERLY JOURNAL OF THE HUNGARIAN METEOROLOGICAL SERVICE

*Special issue: Scale-dependent numerical simulation of the
micro- and mesoscale atmospheric processes*

Guest Editors: István Geresdi and Tamás Weidinger

CONTENTS

<i>Editorial</i>	I
<i>István Faragó, Ágnes Havasi, and Zahari Zlatev:</i> Richardson extrapolation for space-time discretization methods with application to the advection equation	135
<i>Eszter Lábó and István Geresdi:</i> Numerical modelling of the transfer of longwave radiation in water clouds	147
<i>Róbert Lovas, Péter Kardos, András Zénó Gyöngyösi, and Zsolt Bottyán:</i> Weather model fine tuning with software container based simulation platform.....	165
<i>Balázs Szintai, Eric Bazile, and Yann Seity:</i> Improving wintertime low level cloud forecasts in a high resolution numerical weather prediction model	183
<i>Attila Kovács, Ádám Leelőssy, Róbert Mészáros, and István Lagzi:</i> Online coupled modelling of weather and air quality of Budapest using the WRF-Chem model.....	203
<i>Csaba Torma:</i> Detailed validation of EURO-CORDEX and Med-CORDEX regional climate model ensembles over the Carpathian Region.....	217
<i>Anikó Cséplő, Noémi Sarkadi, Ákos Horváth, Gabriella Schmeller, and Tünde Lemler:</i> Fog climatology in Hungary	241

IDŐJÁRÁS

Quarterly Journal of the Hungarian Meteorological Service

Editor-in-Chief

LÁSZLÓ BOZÓ

Executive Editor

MÁRTA T. PUSKÁS

EDITORIAL BOARD

- | | |
|---------------------------------------|--|
| ANTAL, E. (Budapest, Hungary) | MIKA, J. (Eger, Hungary) |
| BARTHOLY, J. (Budapest, Hungary) | MERSICH, I. (Budapest, Hungary) |
| BATCHVAROVA, E. (Sofia, Bulgaria) | MÖLLER, D. (Berlin, Germany) |
| BRIMBLECOMBE, P. (Hong Kong, SAR) | PINTO, J. (Res. Triangle Park, NC, U.S.A.) |
| CZELNAI, R. (Dörcicse, Hungary) | PRÁGER, T. (Budapest, Hungary) |
| DUNKEL, Z. (Budapest, Hungary) | PROBÁLD, F. (Budapest, Hungary) |
| FERENCZI, Z. (Budapest, Hungary) | RADNÓTI, G. (Reading, U.K.) |
| GERESDI, I. (Pécs, Hungary) | S. BURÁNSZKI, M. (Budapest, Hungary) |
| HASZPRA, L. (Budapest, Hungary) | SZALAI, S. (Budapest, Hungary) |
| HORVÁTH, Á. (Siófok, Hungary) | SZEIDL, L. (Budapest, Hungary) |
| HORVÁTH, L. (Budapest, Hungary) | SZUNYOGH, I. (College Station, TX, U.S.A.) |
| HUNKÁR, M. (Keszthely, Hungary) | TAR, K. (Debrecen, Hungary) |
| LASZLO, I. (Camp Springs, MD, U.S.A.) | TÁNCZER, T. (Budapest, Hungary) |
| MAJOR, G. (Budapest, Hungary) | TOTH, Z. (Camp Springs, MD, U.S.A.) |
| MÉSZÁROS, E. (Veszprém, Hungary) | VALI, G. (Laramie, WY, U.S.A.) |
| MÉSZÁROS, R. (Budapest, Hungary) | WEIDINGER, T. (Budapest, Hungary) |

Editorial Office: Kitaibel P.u. 1, H-1024 Budapest, Hungary

P.O. Box 38, H-1525 Budapest, Hungary

E-mail: journal.idojaras@met.hu

Fax: (36-1) 346-4669

**Indexed and abstracted in Science Citation Index Expanded™ and
Journal Citation Reports/Science Edition**

Covered in the abstract and citation database SCOPUS®

Included in EBSCO's databases

Subscription by mail:

IDŐJÁRÁS, P.O. Box 38, H-1525 Budapest, Hungary

E-mail: journal.idojaras@met.hu

Special issue: Scale-dependent numerical simulation of the micro- and mesoscale atmospheric processes

The theme of the 43th Meteorological Scientific Days was about the micro- and mesoscale processes. The one and half days' scientific program was organized by two subcommittees of the Meteorological Scientific Committee of the Hungarian Academy of Sciences (Atmospheric Dynamics and Synoptic Meteorology, furthermore, Atmospheric Physics and Chemistry).

The micro- and mesometeorology is becoming more and more important in research, services, and innovation. The 27 oral presentations and 10 posters covered wide range of topics, such as biosphere-atmosphere interactions, modeling of cloud microphysics, and air pollution transport processes. The progress about storm warnings at Lake Balaton or the applications in aviation meteorology were also presented in the conference. Furthermore, some presentations focused on the parametrization of micro- and mesoscale processes and on their application in the optimization of weather and climate models.

In this special issue seven papers were submitted, and they were accepted after the review process. Most of the papers present results of the numerical simulation of processes with different time and spatial scale:

- The successes in the development of the Richardson extrapolation methods allow the reduction of the model errors caused by numerical methods.
- The longwave radiation plays important role in the evolution of the clouds and fogs. Results about the application of the detailed microphysical scheme shows the importance of the accurate simulation of the radiative cooling at the cloud top and that of the radiative warming at the cloud base.
- We can get an insight into the software container-based simulation platforms, which can promote the goal-oriented application (in our case, aviation meteorology) of the WRF model.
- Based on results of the high-resolution NWP model, an application-oriented study is presented about the wintertime low-level cloud forecasts. The main goal was to optimize the parametrization settings.
- The transport and deposition of different pollutant trace gases (O₃, NO, NO₂ and CO) were simulated by the WRF-CHEM model. The initial conditions for the trace gases were retrieved from the National Emission Inventories database.

- A paper presents results about validation of EURO-CORDEX and Med-CORDEX regional climate model ensembles over the Carpathian Region. The results confirm the distinct capabilities of RCMs to simulate the local features of the climate in the Carpathian Region.
- The last paper in this thematic issue is about the study of the Hungarian fog-climatology, results about the analysis of fog data observed in the last 60 years were published.

Finally, the guest editors would like to thank the authors for their valuable scientific work, furthermore, the Editor in Chief of IDŐJÁRÁS and to the anonymous reviewers for their efforts to publish this special issue.

István Geresdi and Tamás Weidinger
Guest Editors

IDŐJÁRÁS

Quarterly Journal of the Hungarian Meteorological Service
Vol. 123, No. 2, April – June, 2019, pp. 135–146

Richardson extrapolation for space-time discretization methods with application to the advection equation

István Faragó^{1,2}, Ágnes Havasi^{1,3*}, and Zahari Zlatev⁴

¹*MTA-ELTE Numerical Analysis and Large Networks Research Group
Pázmány Péter sétány 1/C, H-1117 Budapest, Hungary*

²*Institute of Mathematics, Budapest University of Technology and Economics
Egry J. u. 1., H-1111 Budapest, Hungary*

³*Department of Applied Analysis and Computational Mathematics
Eötvös Loránd University
Pázmány Péter sétány 1/C, H-1117 Budapest, Hungary*

⁴*Department of Environmental Science – Atmospheric Modeling
Aarhus University
Frederiksborgvej 399, 4000 Roskilde, Denmark*

**Corresponding author E-mail: havasia@cs.elte.hu*

(Manuscript received in final form July 8, 2018)

Abstract—Richardson extrapolation is a numerical procedure which enables us to enhance the accuracy of any convergent numerical method in a simple and powerful way.

In this paper we overview the theoretical background of Richardson extrapolation in space and time, where two numerical solutions, obtained on a coarse and a fine space-time grid are combined by a suitable weighted average. We show that when the Crank-Nicolson method is appropriately combined with this extrapolation technique for the solution of the one-dimensional advection equation, then the order of accuracy increases by two both in time and space. The theoretically derived consistency order and the necessity of the smoothness conditions for the exact solution and for the advection velocity are illustrated by numerical experiments, performed by the advection module of the Danish Eulerian Model (DEM).

Key-words: Richardson extrapolation, convergence order, truncation error, advection equation, Crank–Nicolson method

1. Introduction

L.F. Richardson proposed extrapolation as a powerful tool to accelerate the convergence of a sequence of approximations (see *Richardson*, 1911, 1927). The main idea is to apply the same convergent numerical algorithm, depending on some parameter, by using two different values of this parameter, and combine the obtained numerical solutions to eliminate the leading error term and achieve better accuracy. Its main area of application is the numerical solution of time-dependent ordinary differential equations (see e.g., *Marchuk and Shaidurov* 1983; *Bulirsch and Stoer*, 1966; *Bader and Deuflhard*, 1983, *Zlatev et al.*, 2017). In this case the problem is solved by the same numerical method using two different time-step sizes, and the obtained numerical solutions are combined at each time layer of the coarser grid. In this manner, under certain smoothness conditions, the order of the numerical scheme increases by one. (We remark that by using more than two numerical solutions, even higher order accuracy can be achieved.) In *Faragó et al.* (2013) it is proved that the combination of any diagonally implicit Runge–Kutta method with active Richardson extrapolation is consistent and zero-stable, and consequently it is convergent. In *Zlatev et al.* (2012), the stability of the θ -method combined with the active Richardson extrapolation is investigated on a fixed mesh, and among others it is shown that the combined method is strongly A-stable for the values of θ in the range $[2/3, 1]$. The extrapolated solution is only calculated at the nodes of the coarse grid. *Roache and Knupp* (1993) extended the technique so that the extrapolated solution can also be calculated at the fine grid points. Interesting details about some of the scientists, who initiated the work on different extrapolation methods (including here the Richardson extrapolation) can be found in *Brezinski and Redivo Zaglia* (1993).

The idea of Richardson extrapolation can be applied during the numerical solution of partial differential equations (PDEs) as well. In the majority of the applications, the equations are first discretized in space, which results in a system of time-dependent ordinary differential equations (ODEs), and the Richardson extrapolation is applied with the aim of increasing the order of the time integration method only (see e.g., *Havasi et al.*, 2013; *Mona et al.*, 2015). However, it is also possible to apply this technique with spatial and temporal step sizes refined simultaneously, and the numerical solutions obtained on the coarse and fine space-time grids are then combined with appropriate weight coefficients. This procedure for the case of one spatial dimension has been elaborated in *Richards* (1997). In this paper we apply the idea of Richardson extrapolation in space and time to the one-dimensional advection equation, when the underlying space-time discretization method is the Crank–Nicolson scheme.

The structure of the paper is as follows. In Section 2, we present the general idea of Richardson extrapolation as a convergence acceleration method

and go into more details about the application of this idea during the numerical solution of ODEs. In Section 3, the Richardson extrapolation in space and time is presented for the numerical solution of PDEs with one spatial dimension as proposed by *Richards* (1977), who specified the condition of a proper grid refinement. In Section 4, this idea is applied to the one-dimensional advection equation when solved by the Crank–Nicolson scheme as an underlying method. We will see that in this particular application, the gain in the accuracy is even better than expected, if certain smoothness conditions are satisfied by the exact solution of the advection problem and by the advection velocity. Our theoretical results are illustrated with three numerical experiments, performed by the advection module of UNI-DEM (the Unified Danish Eulerian Model).

2. The principle of Richardson extrapolation

Consider a numerical algorithm depending on parameter τ , which tends to the exact value A^* when τ tends to zero. Typically, τ denotes the mesh size of the discretization. If the method is convergent to the order p , then by solving the problem with the parameter values $\tau_1 = \tau$ and $\tau_2 = \tau/2$, the equalities

$$A^* - A(\tau) = K\tau^p + O(\tau^{p+1}), \quad (1)$$

and

$$A^* - A(\tau/2) = K(\tau/2)^p + O(\tau^{p+1}), \quad (2)$$

hold, where the quantity K is independent of the value of the parameter τ . During Richardson extrapolation, the two numerical solutions are combined by suitable weight coefficients according to the formula

$$A_{RE}(\tau) = -\frac{1}{2^p - 1} A(\tau) + \frac{2^p}{2^p - 1} A(\tau/2) = \frac{2^p A(\tau/2) - A(\tau)}{2^p - 1}, \quad (3)$$

see *Richardson* (1911, 1927).

This procedure is rather general, and it can be applied in combination with any convergent numerical method. It is primarily used during the numerical solution of Cauchy problems for ordinary differential equations, where $A(\tau)$ denotes the numerical solution of the problem by using time step τ . Consider the Cauchy problem

$$\begin{cases} y'(t) = f(t, y), & t \in [0, T] \\ y(0) = y_0, \end{cases}, \quad (4)$$

where $f: \mathfrak{R}^{M+1} \rightarrow \mathfrak{R}^M$, $y_0 \in \mathfrak{R}^M$ is a given initial vector, and the unknown function y is of type $\mathfrak{R} \rightarrow \mathfrak{R}^M$. Let us define the following two grids on the time interval $[0, T]$:

$$\Omega_\tau := \{t_n = n\tau, n = 0, 1, \dots, N_t\}, \quad (5)$$

and

$$\Omega_{\tau/2} := \{t_k = k\tau/2, k = 0, 1, \dots, 2N_t\}, \quad (6)$$

with $N_t \tau = T$. Denote by $z(t_n)$ the numerical solution obtained at time t_n of the coarse grid, and $w(t_n)$ that obtained at the same time layer t_n on the fine grid. (Note that in the second case twice as many steps are taken than in the first case.) Then, following the principle of Richardson extrapolation, the approximation

$$y_{RE}(t_n) := \frac{2^p w(t_n) - z(t_n)}{2^p - 1} \quad (7)$$

provides a numerical solution, accurate to the order $p+1$, in case the exact solution $y(t)$ is $p+1$ times continuously differentiable. During the so-called passive Richardson extrapolation, the combined solution is never used during the further computations, while in the case of the active Richardson extrapolation always the combined solution is propagated, both on the coarse grid and on the fine grid.

3. Richardson extrapolation in space and time

The above idea can be extended to PDEs depending on time and on one space dimension as follows. Two space-time grids are defined on the solution domain $0 \leq x \leq L$, $0 \leq t \leq T$ of the problem. Denote by Δx and Δt the spatial and temporal step sizes of the fine grid, respectively. On the coarse grid, the step sizes $m\Delta x$ and $m^\beta \Delta t$ will be used by certain integers $m \geq 1$ and $\beta \geq 1$, such that both grids cover the solution domain.

One can prove by using some simplifying assumptions (*Richards, 1997*) that the exponent β needs to satisfy a certain requirement in order that higher order of accuracy can be achieved, provided that the exact solution is sufficiently smooth. Let us fix a grid point \tilde{x} which is an element of both the fine and the coarse spatial grid, and denote the truncation error of the method at point $(\tilde{x}, t_n) = (\tilde{x}, n\Delta t)$ by $E_T(\tilde{x}, t_n, \Delta x, \Delta t)$. For a numerical method that has order p_x in space and order p_t in time, the truncation error can be given as

$$E_T(\tilde{x}, t_n, \Delta x, \Delta t) = O((\Delta x)^{p_x}, (\Delta t)^{p_t}) = K_x (\Delta x)^{p_x} + K_t (\Delta t)^{p_t} + O((\Delta x)^{q_x}, (\Delta t)^{q_t}). \quad (8)$$

Here q_x and q_t are integers for which $q_x > p_x$ and $q_t > p_t$, and K_x and K_t depend on the problem and on the solution, but are independent of Δx and Δt . One can show that on a time interval of length Δt , an error of the size $\Delta t E_T$ arises. Denote by $u(\tilde{x}, t)$ the exact solution of the problem at the point (\tilde{x}, t) , by y_f^n the numerical solution on the fine grid, and by y_c^n the numerical solution on the coarse grid, both at the point $(\tilde{x}, n\Delta t)$. Then the error arising during the computation of u on the fine grid, by the assumption that we use the exact solution at time $n\Delta t$, can be written as

$$u(\tilde{x}, (n+1)\Delta t) - y_f^{n+1} = K_x \Delta t (\Delta x)^{p_x} + K_t (\Delta t)^{p_t+1} + O(\Delta t (\Delta x)^{q_x}, (\Delta t)^{q_t+1}). \quad (9)$$

The error of the coarse grid solution after a time step of length $m^\beta \Delta t$ is

$$\begin{aligned} & u(\tilde{x}, (n+m^\beta)\Delta t) - y_c^{n+m^\beta} \\ &= m^\beta \Delta t (m\Delta x)^{p_x} K_x + (m^\beta \Delta t)^{p_t+1} K_t + O(\Delta t (\Delta x)^{q_x}, (\Delta t)^{q_t+1}) \\ &= m^{p_x+\beta} \Delta t (\Delta x)^{p_x} K_x + m^{\beta(p_t+1)} (\Delta t)^{p_t+1} K_t + O(\Delta t (\Delta x)^{q_x}, (\Delta t)^{q_t+1}). \end{aligned} \quad (10)$$

The error on the fine grid at time $(n+m^\beta)\Delta t$ can be expanded as follows, by assuming that the errors of successive time steps add up, moreover, that the coefficients K_x and K_t do not change:

$$\begin{aligned} & u(\tilde{x}, (n+m^\beta)\Delta t) - y_f^{n+m^\beta} \\ &= m^\beta \Delta t (\Delta x)^{p_x} K_x + m^\beta (\Delta t)^{p_t+1} K_t + O((\Delta t)^2 (\Delta x)^{q_x}, \Delta t (\Delta x)^{q_x}, (\Delta t)^{p_t+2}, (\Delta t)^{q_t+1}). \end{aligned} \quad (11)$$

During Richardson extrapolation in space and time, a linear combination of the numerical solutions $y_c^{n+m^\beta}$ and $y_f^{n+m^\beta}$ is determined at the points of the coarse grid as

$$y_{RE}^{n+m^\beta} = \gamma_1 y_c^{n+m^\beta} + \gamma_2 y_f^{n+m^\beta}, \quad (12)$$

where γ_1 and γ_2 are real constants, to be chosen appropriately. By substitution from Eqs. (10) and (11) we are led to the equality

$$\begin{aligned} y_{RE}^{n+m^\beta} &= (\gamma_1 + \gamma_2) u(\tilde{x}, (n+m^\beta)\Delta t) \\ &+ (\gamma_1 m^\beta + \gamma_2 m^{p_x+\beta}) \Delta t (\Delta x)^{p_x} K_x + (\gamma_1 m^\beta + \gamma_2 m^{\beta(p_t+1)}) (\Delta t)^{p_t+1} K_t \\ &+ O((\Delta t)^2 (\Delta x)^{p_x}, \Delta t (\Delta x)^{q_x}, (\Delta t)^{p_t+2}, (\Delta t)^{q_t+1}). \end{aligned} \quad (13)$$

Our aim is to eliminate the leading error terms, containing the coefficients K_x and K_t . Obviously, this can only be achieved if

$$\gamma_1 + \gamma_2 = 1; \quad (14)$$

$$\gamma_1 m^\beta + \gamma_2 m^{p_x + \beta} = 0, \quad (15)$$

and

$$\gamma_1 m^\beta + \gamma_2 m^{\beta(p_t + 1)} = 0. \quad (16)$$

Subtracting (16) from (15), one can easily see that

$$\gamma_2 (m^{p_x + \beta} - m^{\beta(p_t + 1)}) = 0 \quad (17)$$

should hold, which in case of $\gamma_2 \neq 0$ can only be satisfied if $p_x + \beta = \beta(p_t + 1)$, i.e., if $\beta = p_x / p_t$.

Thus, it has been shown that provided the underlying space-time discretization method has order p_x in space and order p_t in time, then, for the increase of the order of accuracy, β should be chosen such that it is equal to the ratio of p_x and p_t . The convergence order of the method obtained in this manner is increased to $O((\Delta t)^2 (\Delta x)^{p_x}, \Delta t (\Delta x)^{q_x}, (\Delta t)^{p_t + 2}, (\Delta t)^{q_t + 1})$, which corresponds to a method with truncation error of $O(\Delta t (\Delta x)^{p_x}, (\Delta x)^{q_x}, (\Delta t)^{p_t + 1}, (\Delta t)^{q_t})$.

4. Application to the 1D advection equation

In this section we present an application of the above approach. Consider the one-dimensional advection equation

$$\partial_t u = -c \partial_x u, \quad x \in [0, L], \quad t \in [t_0, T] \quad (18)$$

with appropriate initial and boundary conditions, where $c = c(x, t)$. Assume that we want to solve this problem with the Crank–Nicolson method

$$\frac{u_i^{n+1} - u_i^n}{\Delta t} = \frac{1}{2} \left(-c_i^{n+0.5} \frac{u_{i+1}^{n+1} - u_{i-1}^{n+1}}{2\Delta x} \right) + \frac{1}{2} \left(-c_i^{n+0.5} \frac{u_{i+1}^n - u_{i-1}^n}{2\Delta x} \right). \quad (19)$$

As it is known, the Crank–Nicolson method has second order both in space and time, i.e., $p_x = p_t = 2$ (Strikwerda, 2004). According to the previous section, the proper choice of β is $\beta = p_x / p_t = 1$. Consequently, if the stepsize of the coarse grid is twice the stepsize Δx of the fine grid (i.e., $m = 2$), then Δt should also by

multiplied by 2 to generate the coarse time grid. Further, we need the coefficients γ_1 and γ_2 . From condition (15), by substitution of the values $m = 2$, $p_x = 2$ and $\beta = 1$, the equation

$$\gamma_1 + 4\gamma_2 = 0$$

is obtained, from which, in view of Eq. (14), we get the coefficients $\gamma_1 = -1/3$, and $\gamma_2 = 4/3$. (Note that these weights are the same as those applied when Richardson extrapolation is performed only in time for a method of order 2.) Moreover, since $\Delta t = \Delta x$, therefore by Eq. (13) one can expect that the order of accuracy increases by one, both in space and time. However, in this case we get an even better acceleration, as it is shown by direct expansion into Taylor series in Zlatev et al., 2011: If the advection velocity $c = c(x, t)$ is twice continuously differentiable both by x and t , and the exact solution $u(x, t)$ is four times continuously differentiable both by x and t , then the combination of the Crank–Nicolson method with the active Richardson extrapolation has order four both in space and time for problem Eq. (18). (For details of the proof see the given reference.)

4.1. Numerical experiments

Our theoretical results were tested by using different parameter choices and initial conditions together with periodic boundary conditions in the advection problem Eq. (18). Note that in order that the active Richardson extrapolation can be applied, at all time layers of the coarse grid interpolation is needed to the fine grid so that we have the combined solution on the fine grid before the next time step.

4.2. Test problem 1

In the first experiment performed by the advection module of UNI-DEM, the following parameter values were specified: $L = 50000000$, $t_0 = 43200$, $T = 129600$, $c(x, t) = 320$, and we used the initial function

$$u_0(x) = 1.4679 \cdot 10^{12} (1 + 99e^{-10^{-12}(x-10000000)^2}).$$

This is a smooth function with sharp gradients, see *Fig. 1*.

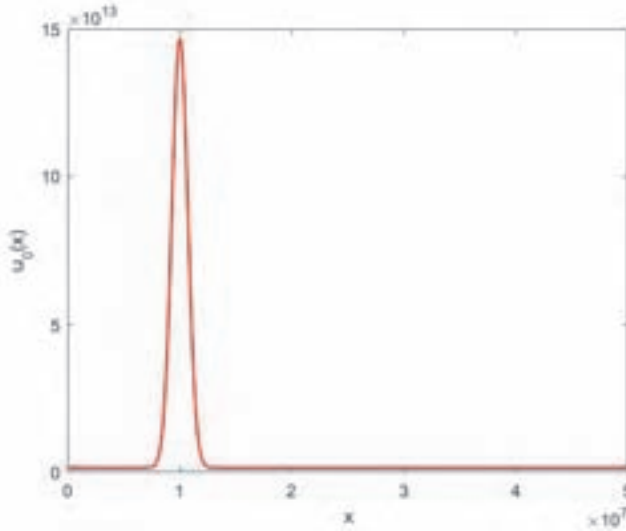


Fig. 1. The initial function in Test problem 1.

The exact solution has the form $u(x, t) = u_0(x - 320(t - 43200))$, which has the same smoothness property as the initial function. Table 1 shows the global errors obtained by spatial and time steps, halved several times simultaneously. When the Crank–Nicolson method is applied alone, the error is reduced by a factor of four to a good approximation, i.e., the method behaves as a fourth-order one, as expected. Moreover, when combined with the active Richardson extrapolation, the errors roughly decrease by a factor of 16, so the theoretically obtained fourth-order convergence is obtained.

Table 1. Global errors obtained in Test problem 1 by the Crank–Nicolson method alone (CN) and by its combination with the active Richardson extrapolation (CN + RE). N_t : the number of time steps; N_x : the number of spatial steps. In parentheses the factors are given by which the global error decreased in comparison with the error in the previous row.

N_t	N_x	CN	CN + RE
168	160	7.373E-01	1.454E-01
336	320	4.003E-01 (1.842)	1.741E-02 (8.350)
672	640	1.254E-01 (3.142)	1.224E-03 (14.220)
1344	1280	3.080E-02 (4.135)	7.730E-05 (15.837)
2688	2560	7.765E-03 (3.967)	4.841E-06 (15.970)
5376	5120	1.954E-03 (3.974)	3.026E-07 (15.999)
10752	10240	4.892E-04 (3.994)	1.891E-08 (16.004)
21504	20480	1.224E-04 (3.999)	1.181E-09 (16.011)

4.3. Test problem 2

In this experiment, the parameters were chosen as $L=2\pi$, $t_0=0$, $T=2\pi$, $c(x,t)=0.5$, and the initial function was the highly oscillatory function shown in Fig. 2:

$$u_0(x) = 1.4679 \cdot 10^{12} (100 + 99 \sin(10x)).$$

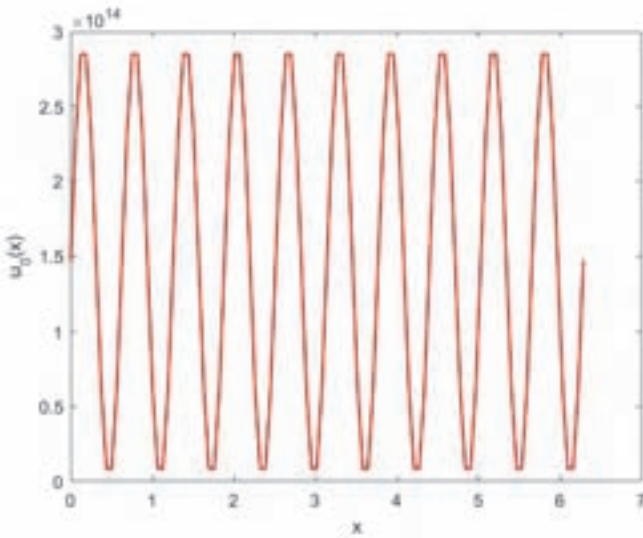


Fig. 2. The initial function in Test problem 2.

The exact solution is $u(x,t) = u_0(x - 0.5t)$.

The global errors are shown in Table 2. With the Crank–Nicolson method applied alone, similar results were obtained as before. However, when combined with the active Richardson extrapolation, the convergence is slower than fourth (but faster than third) order. The reason for this is probably the fact that the third-order interpolation polynomial, applied for interpolation of the coarse grid solution to the fine grid, cannot be applied at the boundary of the space domain, so here a second-order formula was used.

Table 2. Global errors obtained in Test problem 2 by the Crank–Nicolson method alone (CN) and by its combination with the active Richardson extrapolation (CN + RE). N_t : the number of time steps; N_x : the number of spatial steps. In parentheses the factors are given by which the global error decreased in comparison with the error in the previous row

N_t	N_x	CN	CN + RE
168	160	7.851E-01	1.560E-02
336	320	2.160E-01 (3.635)	1.227E-03 (12.713)
672	640	5.317E-02 (4.062)	1.072E-04 (11.432)
1344	1280	1.327E-02 (4.007)	1.150E-05 (9.333)
2688	2560	3.319E-03 (3.997)	1.193E-06 (9.641)
5376	5120	8.299E-04 (4.000)	1.478E-07 (8.071)
10752	10240	2.075E-04 (4.000)	1.618E-08 (9.136)
21504	20480	5.187E-05 (4.000)	1.965E-09 (8.233)

4.4. Test problem 3

In this case, the parameters of the first test problems were used with the exception that the initial function was changed to the following one:

$$u_0(x) = \begin{cases} 1.4679 \cdot 10^{12} & \text{if } x \leq 5000000 \quad \text{or} \quad x \geq 15000000 \\ 1.4679 \cdot 10^{12} \left(1 + 99 \frac{x - 5000000}{5000000} \right) & \text{if } 5000000 < x \leq 10000000 \\ 1.4679 \cdot 10^{12} \left(1 + 99 \frac{15000000 - x}{5000000} \right) & \text{if } 10000000 < x \leq 15000000 \end{cases}$$

see Fig. 3. This initial function is continuous, but its first derivative is discontinuous, and so none of the sufficient conditions for the fourth-order convergence of the combined method is satisfied. As Table 3 shows, the theoretically derived order is not obtained for any of the two methods, however, the Richardson extrapolated method is still more accurate.

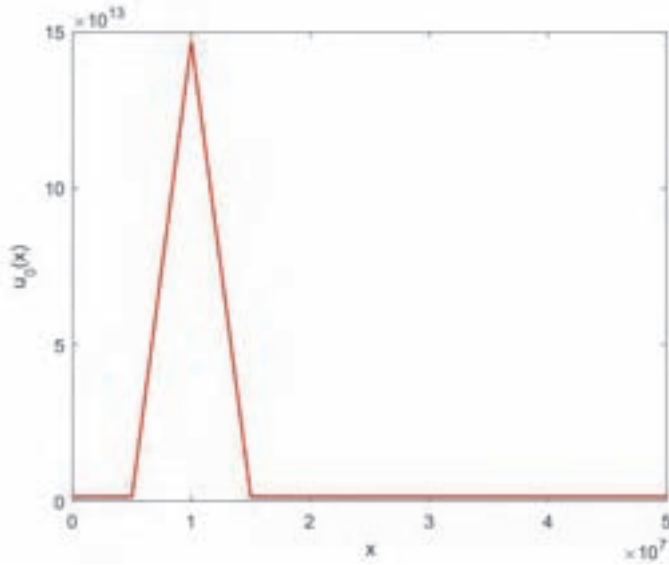


Fig. 3. The initial function in Test problem 3.

Table 3. Global errors obtained in Test problem 3 by the Crank–Nicolson method alone (CN) and by its combination with the active Richardson extrapolation (CN + RE). N_t : the number of time steps; N_x : the number of spatial steps. In parentheses the factors are given by which the global error decreased in comparison with the error in the previous row

N_t	N_x	CN	CN + RE
168	160	1.353E-01	4.978E-02
336	320	7.687E-02 (1.760)	2.761E-02 (1.803)
672	640	4.424E-02 (1.737)	1.551E-02 (1.780)
1344	1280	2.555E-02 (1.732)	8.570E-03 (1.810)
2688	2560	1.636E-02 (1.561)	4.590E-03 (1.867)
5376	5120	1.051E-02 (1.552)	2.318E-03 (1.980)
10752	10240	5.551E-03 (1.899)	1.188E-03 (1.951)
21504	20480	2.921E-03 (1.900)	6.575E-04 (1.807)

5. Conclusion

Richardson extrapolation is a powerful tool to accelerate the convergence of numerical methods, and it can be applied not only to ordinary differential equations, but also to partial differential equations. In the latter case we either use the extrapolation after space discretization, or we apply Richardson extrapolation in space and time. In this paper we presented how the latter method works on the one-dimensional advection equation when the underlying numerical scheme is the Crank–Nicolson method. Our numerical experiments confirmed the theoretically derived order increase, and showed that satisfying the smoothness conditions is important to get this high order convergence.

References

- Bader, G. and Deuffhard, G., 1983: A semi-implicit midpoint rule for stiff systems of ordinary differential equations, *Numer. Math.* 41, 373–398. <https://doi.org/10.1007/BF01418331>
- Bulirsch, R. and Stoer, J., 1966: Numerical treatment of ordinary differential equations by extrapolation methods, *Numer. Math.* 8, 1–13. <https://doi.org/10.1007/BF02165234>
- Brezinski, C. and Redivo Zaglia, M., Extrapolation Methods. Theory and Practice. Amsterdam etc., North-Holland 1991. X, 464 pp., Dfl. 225.00. ISBN 0-444-88814-4 (Studies in Computational Mathematics 2).
- Faragó, I., Havasi, Á. and Zlatev, Z., 2013: The convergence of diagonally implicit Runge-Kutta methods combined with Richardson extrapolation. *Comput. Math. Appl.* 65, 395–401. <https://doi.org/10.1016/j.camwa.2012.04.016>
- Havasi Á., Horváth R, and Szabó T., 2013: Comparison of Some Parameter Estimation Techniques Applied to Proton Exchange Membrane Fuel Cell Models. *J. Fuel Cell Sci. Technol.* 10(5) Paper 051001.
- Marchuk, G.I. and Shaidurov, V.V., 1983: Difference Methods and Their Extrapolations, Springer-Verlag, New York. <https://doi.org/10.1007/978-1-4613-8224-9>
- Mona T., Lagzi I., and Havasi Á., 2015: Solving Reaction-Diffusion and Advection Problems with Richardson Extrapolation. *J. Chem.* Paper 350362.
- Richards, S.A., 1997: Completed Richardson extrapolation in space and time. *Commun. Numer. Methods Engin.* 13, 573–582. [https://doi.org/10.1002/\(SICI\)1099-0887\(199707\)13:7<573::AID-CNM84>3.0.CO;2-6](https://doi.org/10.1002/(SICI)1099-0887(199707)13:7<573::AID-CNM84>3.0.CO;2-6)
- Richardson, L.F., 1911: The Approximate Arithmetical Solution by Finite Differences of Physical Problems Including Differential Equations, with an Application to the Stresses in a masonry dam. *Philosoph. Transact. Roy. Soc. London, Series A* 210, 307–357.
- Richardson, L.F., 1927: The Deferred Approach to the Limit, I. Single Lattice, *Philosoph. Transact. Roy. Soc. London, Series A*, 226, 299–349.
- Roache, J.R. and Knupp, P.M., 1993: Completed Richardson extrapolation, *Commun. Numer. Methods in Engin.* 9, 365–374.
- Strikwerda, J. C., 2004: Finite Difference Schemes and Partial Differential Equations, Second edition, SIAM, Philadelphia.
- Zlatev, Z., Dimov, I., Faragó, I., Georgiev, K., Havasi, Á., and Ostrowsky, Tz., 2011: Solving Advection Equations by Applying the Crank-Nicolson Scheme Combined with the Richardson Extrapolation, *Int. J. Different. Equat.* 2011, Article ID 520840. <http://dx.doi.org/10.1155/2011/520840>
- Zlatev, Z., Faragó, I., and Havasi, Á., 2012: Richardson extrapolation combined with the sequential splitting procedure and theta-method, *Cent. Eur. J. Math.* 10, 159–172. <https://doi.org/10.2478/s11533-011-0099-7>
- Zlatev, Z., Dimov, I., Faragó, I., and Havasi, Á., 2017: Richardson Extrapolation - Practical Aspects and Applications. De Gruyter. <https://doi.org/10.1515/9783110533002>

IDŐJÁRÁS

Quarterly Journal of the Hungarian Meteorological Service
Vol. 123, No. 2, April – June, 2019, pp. 147–163

Numerical modeling of the transfer of longwave radiation in water clouds

Eszter Lábó¹ and István Geresdi²

¹*Hungarian Meteorological Service*
Kitaibel Pál u. 1., H-1024 Budapest, Hungary

²*Faculty of Science, University of Pécs*
Ifjúság u. 6., H-7626 Pécs, Hungary

**Corresponding author E-mail: labo.e@met.hu*

(Manuscript received in final form March 13, 2019)

Abstract—The strong interaction between the radiation, cloud microphysics, and cloud dynamics requires more advanced radiation schemes in numerical calculations. Detailed (bin) microphysical schemes, which categorize the cloud particles into bin intervals according to their sizes, are useful tools for more accurate simulation of evolution of the hydrometeors. Our research aimed at the development of a new bin radiation scheme based on a commonly used bin microphysical scheme and the implementation of this new scheme into the RRTMG LW longwave radiation-transfer model. We have applied the MADT approximation method to evaluate radiation interaction. The absorption coefficients are calculated by using bin resolved size distribution of water droplets, which is the output of a bin microphysical scheme.

The longwave absorption coefficients applied in this new method are in tune with those of a bulk radiation scheme, which is currently used in operational numerical weather prediction models. However, the two schemes gave reasonably different results for longwave radiation cooling rates at stratocumulus cloud tops and fog layers. Unfortunately, only few observation data are available to check our results directly. Indirect evaluation can be based on outputs of numerical radiative transfer models published in various studies since the nineties. Achievements of our research enable more precise calculation of longwave radiation profiles, and better prediction of dynamic and thermodynamic processes in water clouds (e.g., lifetime of stratocumulus clouds, fog evolution, and precipitation formation).

Key-words: longwave radiation, bin microphysical scheme, numerical modeling, longwave cooling rates, stratocumulus clouds

1. Introduction

Both longwave and shortwave radiation play an important role in the development of atmospheric processes. They basically determine the temperature distribution in the atmosphere, and thus impact the processes from cloud and precipitation formation on microphysical scale to air mass motion on continental scale. Therefore, many studies have focused on the understanding of radiation budget of the Earth, including, e.g., spatial distribution of cloud-radiation interactions. Large number of these studies have used satellite measurements since the mid-eighties (*Ramanathan et al., 1989*). They concluded that the global average of shortwave (SW) radiation reaching the surface is reduced by 44.5 W/m^2 due to the presence of clouds; and about 31.3 W/m^2 is absorbed by the clouds in the longwave (LW) region. Thus, the presence of clouds results in a net decrease of 13.2 W/m^2 of total longwave flux. This estimation has been confirmed by contemporary results of the Clouds and the Earth's Radiant Energy System (CERES) sensors onboard the polar orbiting Terra and Aqua satellites (*Allan, 2011*). *Fig. 1* shows the mean effect of clouds on radiation fluxes in shortwave (a) and longwave (b) range, furthermore, their net impact (c) for a 7 years period. We can observe that the net effect of the clouds varies mainly between -20 W/m^2 and 10 W/m^2 , yielding an average around -10 W/m^2 (*Fig. 1c*). Similar results have been provided by numerical simulations. For the Mediterranean Basin, *Pyrina et al. (2015)* calculated that in the case of outgoing SW radiation, the effect of cloud ranged between -60 and -10 W/m^2 on top of atmosphere; whereas in the case of outgoing LW radiation this effect was between 6 and 22 W/m^2 on top of atmosphere (*Fig. 2*). Their result about the net average of around -21 W/m^2 , however, overestimates the total net impact of clouds on radiation fluxes observed by CERES. This bias, order of 10 W/m^2 between numerical simulations and satellite measurements has been often reported in other publications as well (*Fairall et al., 2008*).

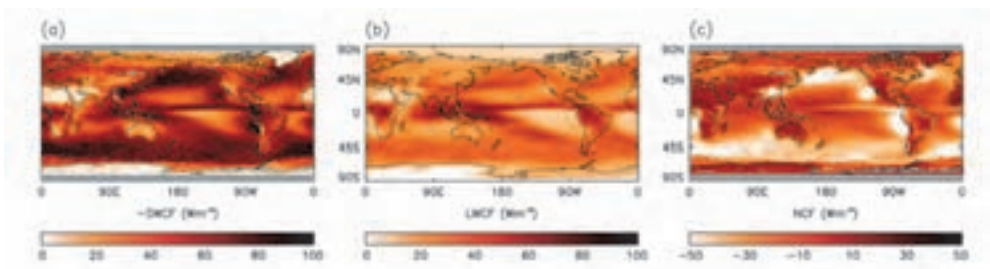


Fig. 1. CERES satellite data on the effect of clouds on the top of atmosphere (TOA) radiation budget between 2001–2007 in the shortwave (a) and longwave (b) region, and the net effect in these two regions (c).

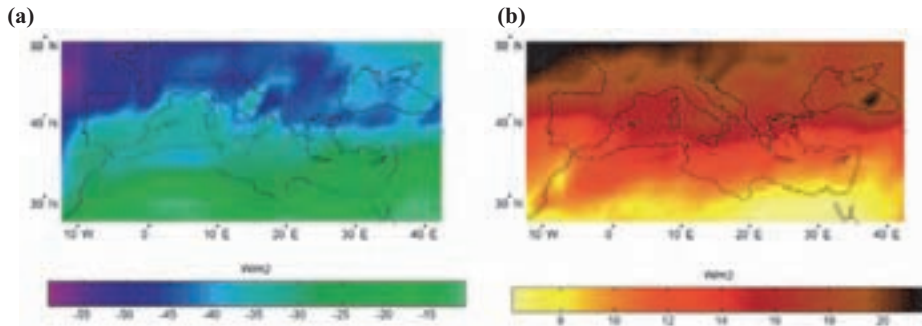


Fig. 2. 24-year (1984–2007) model computed cloud radiative effects on the Mediterranean region for shortwave TOA (a) and longwave TOA (b) radiation.

1.1. Longwave radiation and cloud interaction

More precise assessment of the impact of clouds on radiation budget becomes possible by the classification of clouds. It was demonstrated that at the top of the atmosphere, the outgoing longwave radiation is mostly modified by high-level cirrus, nimbostratus, and convective clouds; whereas longwave fluxes at the surface are controlled by low-level altostratus, cumulus, and stratocumulus clouds (McFarlane *et al.*, 2013). Our studies concentrated on stratocumulus clouds as they cover approximately one-fifth of the Earth’s surface as an annual average (Wood, 2012). Moreover, longwave radiation is the main driver to stratocumulus cloud formation and life-cycle; because cooling rates due to large longwave radiation emission at the top of these clouds cause the instability that maintains the convective updraft in stratocumulus clouds. Reduced entrainment because of cooling at cloud top can even result in significant extension of cloud lifetime (Petters *et al.*, 2012). Similarly to stratocumulus clouds, longwave cooling at the top of a fog layer influences significantly the evolution of the fog (Gultepe and Milbrandt, 2007). Also, it is the main factor in mixing with the air above the foggy layer (Mazoyer *et al.*, 2017).

Longwave radiation cooling occurs within a 20–50 m thick layer at the cloud top, and its value varies mainly between -7 K/h and -13 K/h (Austin *et al.*, 1995; Koracin *et al.*, 2001) for stratocumulus clouds and a lower value for the fog (Wærsted *et al.*, 2017), depending on the liquid water content. Cloud base heating at stratocumulus cloud base is spread over a 100m thick layer, and only reaches a magnitude between 0.5 – 1 K/h (Wood, 2012). Moreover, microphysical processes like diffusional growth of water droplets, turbulent entrainment, supersaturation, and precipitation formation are also affected by the

rate of longwave cooling at the top of the cloud and the fog (*Wærsted et al., 2017*). Therefore, it is important to study the interaction on a microphysical scale containing information of cloud-size distribution. This can only be done by numerical models as radiation measurement campaigns fail to provide sufficient accuracy especially in the case of pyrgeometers (*Ackerman et al., 1995*).

2. Numerical methods to describe radiation-cloud processes

Numerical weather prediction models apply parameterization tools to simulate physical processes. These parameterizations imply application of simplified mathematical formulas to describe natural phenomena, otherwise it would need large computer capacity and would take very long time to numerically reproduce these processes. In our case, two different parameterizations are considered: radiation schemes involving calculation of absorption coefficients, and microphysical schemes determining concentration and mixing ratio of water droplets. Thus, enhancement of radiation scheme can be either achieved by enhancement of input parameters from more precise microphysical parameterization (e.g., two-moment or even bin scheme instead of one-moment schemes, *Lee and Donner, 2011*); or by improvement of radiation absorption parameterization itself. We have developed a method to combine both, that is, we have implemented a method to calculate the absorption coefficients by incorporating the bin microphysical scheme in new equations. This modification is made within the radiative transfer model RRTMG LW (rapid radiative transfer model for the longwave radiation) (*Mlawer et al., 1997; Clough et al., 2005*), a high accuracy numerical radiation tool implemented in several global numerical weather prediction models like ECMWF (*Morcrette et al., 2008*) or GFS (*Sun et al., 2010*), as well as in limited area weather forecasting models like ALADIN (*Yessad, 2014*) or WRF (*Deng et al., 2009*). It divides the longwave spectra into 16 bands.

Detailed bin microphysical schemes are characterized by a number of size intervals of the water droplets (in our case, 36), where the concentration and mixing ratio of water droplets are calculated separately; therefore, arbitrary size distribution of droplets can be converged. Otherwise, in one-moment and two-moment schemes, we need an assumption for the size distribution function, which is normally a gamma-function (*Lee and Donner, 2011*). These latter approximations are called bulk-schemes.

If size distribution is known, volume absorption coefficients can be calculated by the following formula:

$$\beta_{abs,\lambda}(z'') = \pi \int_0^{\infty} n(r, z'') r^2 Q_{abs}(\lambda, r) dr \quad , \quad (1)$$

where $n(r, z'')$ is the size distribution at location z'' , r is the radius of the droplet, λ is the wavelength, and Q_{abs} is the absorption efficiency (Petty, 2006).

Longwave radiation interaction with clouds includes both absorption and scattering (which together produce longwave extinction). However, the whole process is dominated by the absorption (Delamere et al., 2000) for water droplets; scattering is non-negligible in case of high cirrus clouds (Fu et al., 1997). Since in the RRTMG LW model only absorption coefficients are used for the bulk scheme, in the present publication we have used the bin absorption coefficient to study effects of this new bin radiation scheme for water clouds. Studies applying the bin extinction coefficient (β_{ext}) as approximation for longwave interactions were published in Lábó and Geresdi (2016).

2.1. Bin method to calculate the radiation coefficients

If we use a bin scheme, we have $N_{bins}=36$ bins in which different size distributions are labeled as $n_k(M)$, and so the volume coefficients can be calculated for a wavelength interval $\Delta\lambda$ as a weighted average according to the E_λ Planck-function:

$$\beta_{abs} = \sum_{k=2}^{N_{bins}} \left[\int_{\Delta\lambda} E_\lambda \int_{M_{k-1}}^{M_k} A(D) Q_{abs}(D, m, \lambda) n_k(M) dM d\lambda \right] / \int_{\Delta\lambda} E_\lambda d\lambda \quad (2)$$

where M_{k-1} and M_k are the mass of droplets at the edges of the k th bin, $A(D)$ is the cross section ($A(D) = \pi r^2$), D is the diameter of droplet, and m is the refraction index.

In bulk numerical models, the absorption coefficients are given by an empirical formula, such as:

$$\frac{\beta_{abs}}{LWC} = a \cdot r_{eff}^b + c, \quad (3)$$

where a , b , and c coefficients are fixed according to empirical data; and can be evaluated for different size-intervals of water drops (Hu and Stamnes, 1993).

Nevertheless, it is possible to solve Eq.(2) if Q_{abs} is given by analytical formula. For this, we have used the *Modified Anomalous Diffraction Theory* (MADT, Mitchell, 2000). The MADT approximation is based on the propagation of electromagnetic waves as it is plotted in Fig. 3.

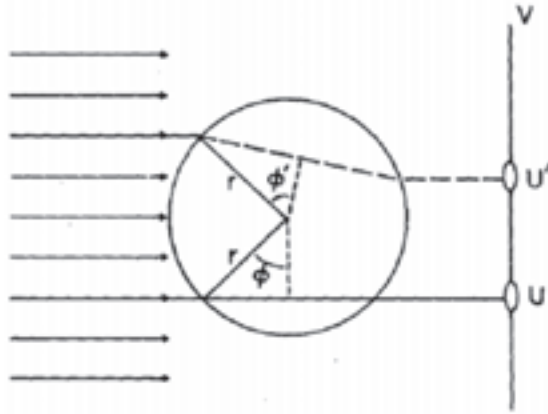


Fig. 3. Trajectories of incoming electromagnetic wave on a water droplet symbolized by the circle (Ackerman and Stephens, 1987).

In addition to absorption coefficients calculated by the *Anomalous Diffraction Theory* method ($Q_{ext,ADT}$), the MADT method also takes into account reflection and refraction (C_{res}) of the electromagnetic waves, and the correction for internal reflection and refraction (C_{ir}):

$$Q_{abs}(D, \lambda, m) = (1 + C_{ir}(D, \lambda, m) + C_{res}(D, \lambda, m)) Q_{abs,ADT}(D, \lambda, m) \quad (4)$$

The MADT method provides analytical formulas for Q_{abs} as a function of D , λ , and m (Harrington and Olson, 2001). If we put these equations into Eq.(2), along with the linear formula for the size distribution of the number concentration in the k th bin $n_k(M) = A_k + M \cdot B_k$, we have the following expression for β_{abs} :

$$\beta_{abs} = \sum_{k=2}^{N_{bins}} A_k \cdot \sum_{j=1}^{16} K_{A_{kj}}(M_{k-1}, M_k, \Delta \lambda_j) + \sum_{k=2}^{N_{bins}} B_k \cdot \sum_{j=1}^{16} K_{B_{kj}}(M_{k-1}, M_k, \Delta \lambda_j) \quad (5)$$

In Eq.(5), j denotes the band (and $\Delta \lambda_j$ is the bandwidth) used in the RRTMG LW model.

Because the elements of $K_{A_{kj}}(M_{k-1}, M_k, \Delta \lambda_j)$ and $K_{B_{kj}}(M_{k-1}, M_k, \Delta \lambda_j)$ matrixes can be pre-calculated (without knowing the actual $n_k(M)$ distribution itself) and the A_k and B_k coefficients are evaluated by the microphysics scheme, the β_{abs} can be calculated very efficiently (Lábó, 2017).

3. Comparison of results for the two schemes

Before application of the new scheme with the RRTMG LW radiation transfer model for a stratocumulus cloud, we have compared solely the bulk and bin absorption coefficients that will be used in the RRTMG model.

3.1. Comparison of longwave absorption coefficients evaluated by bulk and bin schemes

The absorption coefficients calculated by current bin scheme (using Eq.(5)) are compared to that of calculated by bulk scheme using Eq.(3) (Hu and Stammes, 1993). The absorption coefficients averaged over the wavelength-bands defined in RRTMG LW model were compared (Fig. 4). The bulk data can be found in the lookup table of RRTMG LW model, bin data were calculated by using Eq.(5). The comparison of the plots shows that variations between these absorption coefficients are higher mainly in case of smaller effective radius ($r_{eff} < 5 \mu\text{m}$) and at larger wavelengths ($> 10 \mu\text{m}$). The difference reaches a factor of 2 around $10 \mu\text{m}$ (close to the peak of the Planck-function), out of this interval the divergence decreases rapidly. For larger effective radius ($r_{eff} \sim 8 \mu\text{m}$) the differences are significantly smaller (maximum 20%). Large deviation occurs only in the band of $5.55\text{--}6.76 \mu\text{m}$, however, at these wavelengths the value of Planck function is low.

Besides the absorption coefficients, we have compared the extinction coefficients for individual wavelengths in our previous study, published in Lábó and Geresdi (2013). In that study, similar results were found: the difference between the extinction coefficients based on the bulk and bin schemes was relatively small, about 10–20% if $r_{eff} < 12 \mu\text{m}$, and even smaller ($< 10\%$) for the larger effective radius.

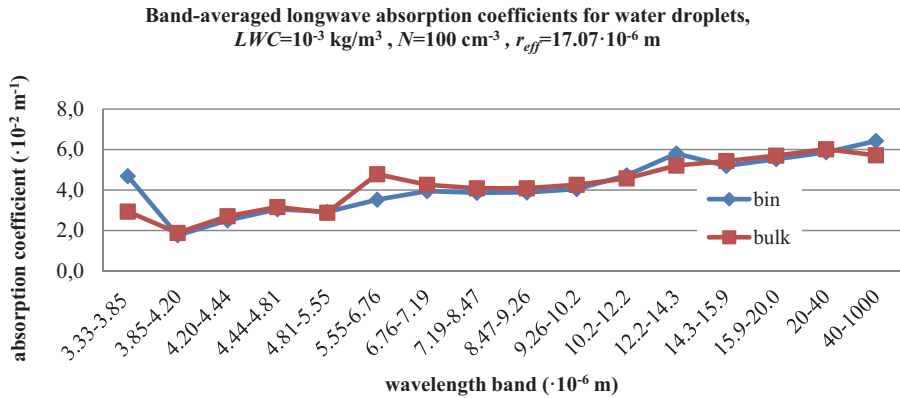
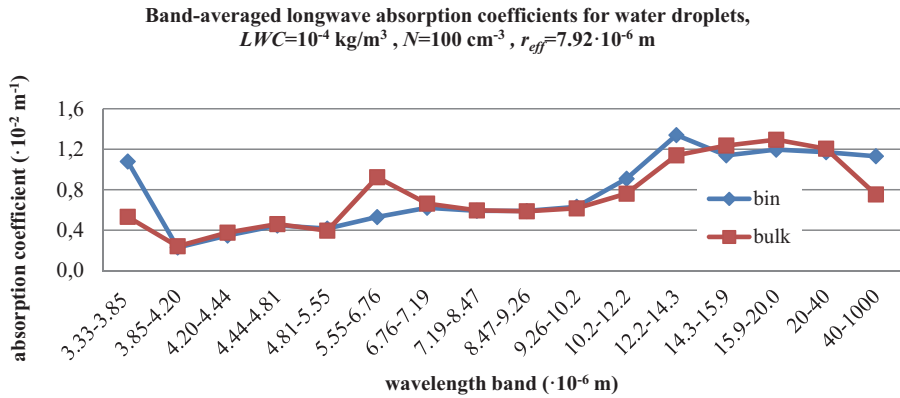
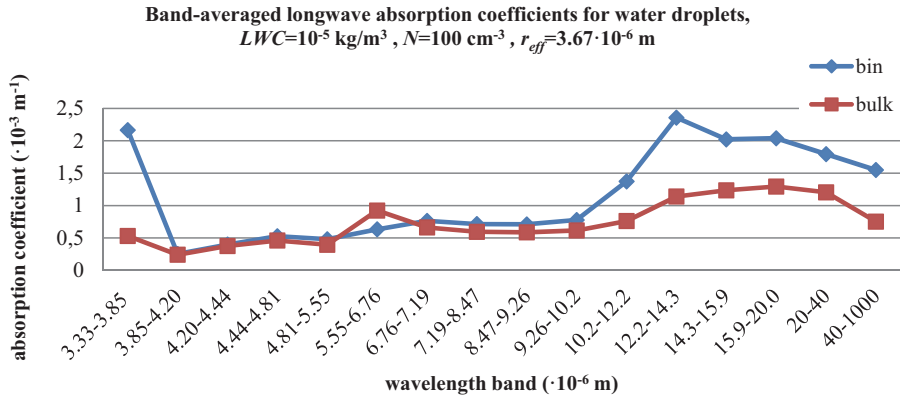


Fig. 4. Band-averaged volume absorption coefficients, calculated by bin and bulk radiation schemes for three given effective radii.

3.2. New results for longwave heating rates

The band-averaged bin absorption coefficients were implemented in the RRTMG LW radiative transfer model (named bin radiation scheme in the present publication). The results of this bin radiation scheme were compared to the results of initial RRTMG LW bulk scheme. The original version of RRTMG LW (called bulk radiation scheme in the present publication) uses Eq.(3) in computing the absorption coefficient.

A two-dimensional kinematic model was used to simulate the formation of shallow stratocumulus clouds. In this model, a detailed bin microphysical scheme was applied (Lábó and Geresdi, 2016) to prepare the vertical profile of the liquid drops for application in the bin radiation scheme. Vertical transfer of longwave radiation was calculated in each vertical column throughout a domain which included the cloud. The domain had an extent of 2 km horizontally and 1 km vertically, and a grid resolution of 20 m in both directions.

Fig. 5a shows the size distributions related to the bin and bulk microphysical schemes in one of the grid points in the downdraft region of the cloud; furthermore, *Fig. 5b* shows the calculated longwave heating rates in the column containing this grid point. It can be observed that the bin cooling rate is higher at the cloud top, as well as the bin heating rate is higher at the cloud base than the bulk rates. The differences are about 20% at both for cloud top and base. Note that cooling occurs in a narrower layer in the case of the bin scheme. Similar results for the bin radiation scheme compared to the bulk scheme were found for higher CCN concentrations (Lábó and Geresdi, 2016). Contrary to the comparison of the absorption coefficients (*Fig. 4*), for which we have assumed that the size-distributions of water droplets are the same for both bulk and bin schemes, the two microphysical schemes applying different description of the microphysical processes resulted in distinct size distributions (see *Fig. 5a*). This difference must have contributed to the divergence between the heating/cooling rates calculated by the two schemes.

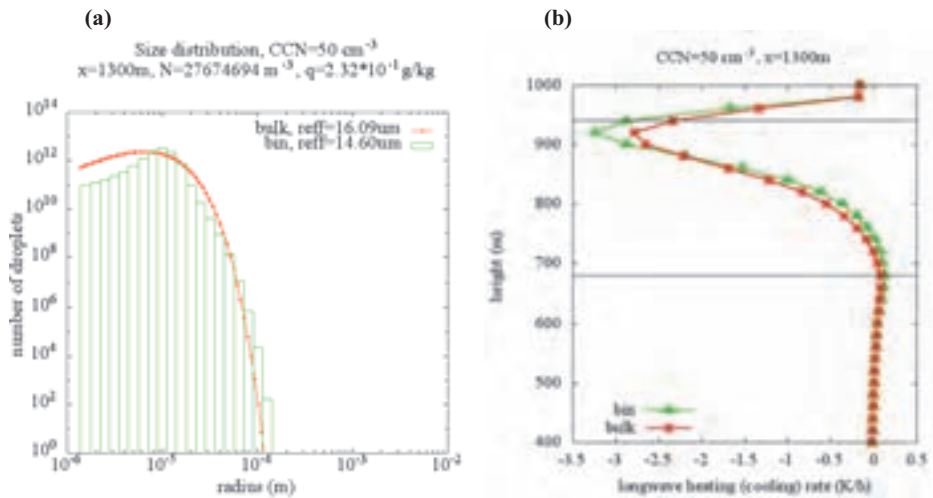
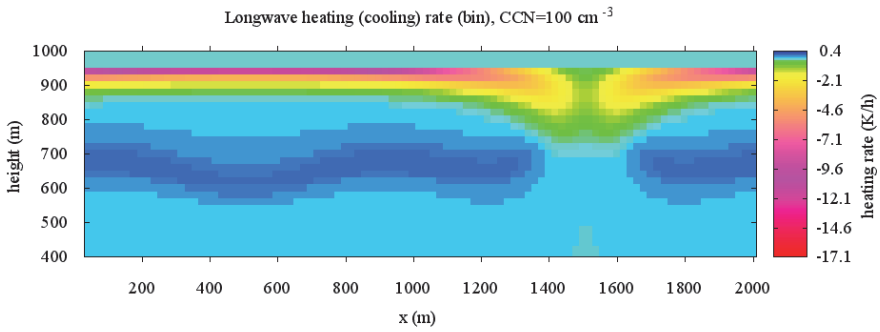


Fig. 5. Size distribution and effective radius in a given grid point of the stratocumulus cloud (a); and vertical longwave flux profiles in the same column($x=1300$ m) (b); for the bin and bulk radiation schemes. The horizontal lines show the cloud top and base.

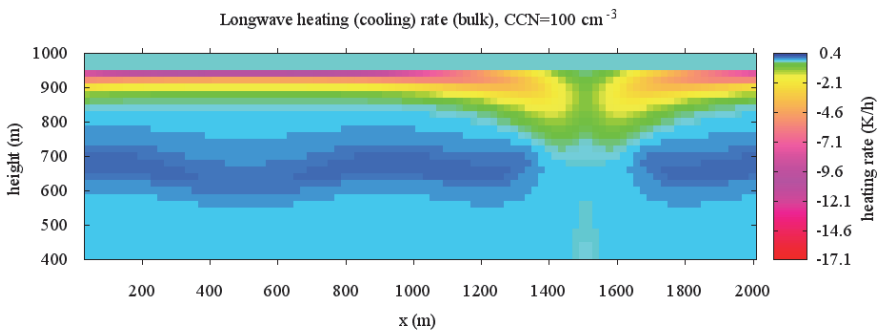
Fig. 6 shows the 2D cross section of the evaluated cooling rates in case of a maritime stratocumulus cloud if cloud condensation nuclei concentration was equal to 100 cm^{-3} ($\text{CCN}=100 \text{ cm}^{-3}$).

Comparison of Fig. 6a and Fig. 6b shows that the bin longwave cooling rates at cloud top always exceed the rates calculated by the bulk scheme (Fig. 6c). This cooling always occurs in a thinner layer in the case of bin scheme (about 80 m) than in the case of bulk scheme (about 100 m). The heating rate at cloud base is also slightly larger in the case of bulk scheme. The difference between the highest cooling rates remains around 20%.

(a)



(b)



(c)

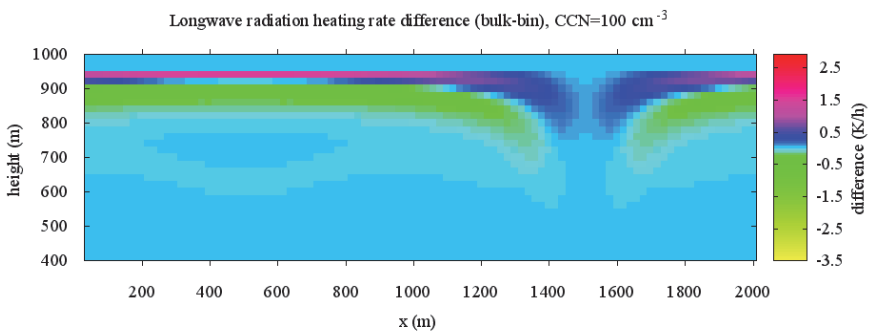


Fig. 6. Longwave heating (cooling) rates calculated for a maritime stratocumulus cloud for bin (a) and bulk (b) radiation schemes, and their difference (c).

3.3. Comparison with longwave cooling rates in other studies

Measurement of longwave cooling rates in stratocumulus clouds has always been a challenging task, which demonstrated large uncertainties of the measurements of radiation fluxes by Eppley pyrgeometers ($\pm 10 \text{ W/m}^2$) (Duda *et al.*, 1991). Therefore, from the nineties, cooling rates were derived mostly by numerical modeling simulations. These studies dealt with clouds formed over maritime areas (as 80% of stratocumulus clouds occur in these regions), so we have used the results of numerical simulations of condensation nuclei concentration of $CCN=100 \text{ cm}^{-3}$ for comparison.

Because longwave cooling rates strongly depend on the liquid water concentration (*LWC*) profiles (Lábó and Geresdi, 2016), the maximum liquid water contents are also summarized in *Table 1*.

Table 1. Comparison of values of longwave cooling rates at cloud base and cloud top of maritime stratocumulus ($CCN \sim 100 \text{ cm}^{-3}$) in different publications, and results for the $CCN100$ cloud in our studies (bin and bulk schemes)

Published study and method	Heating (cooling) rate (K/h)		<i>LWC</i> (g/kg)
	at cloud base	at cloud top	
<i>Oliver et al.</i> (1978) model	0.7	-6.8	0.38
<i>Curry</i> (1986) model	-	(-4.0) - (-7.5)	0.5 - 0.7
<i>Duda et al.</i> (1991) measurement	-	-5.0	0.5
<i>Duda et al.</i> (1991) model	0.5	-9.5	0.5
<i>Ackerman et al.</i> (1995) model	-	-8.5	0.4
<i>Austin et al.</i> (1995) model	-	(-8.0) - (-8.7)	0.58
<i>Olsen</i> (1996) model	0.8 - 1.0	(-6.2) - (-7.0)	0.3 - 0.6
<i>Koracin et al.</i> (2001) model	0.6 - 1.7	(-10.4) - (-12.5)	-
<i>Chai et al.</i> (2003) measurement	-	(-7.0) - (-20.0)	0.4
<i>Larson et al.</i> (2007) model	0.6	-13.0	0.55
bin model	0.21	-8.4	0.48
bulk model	0.19	-7.6	0.48

It can be seen from *Table 1*, that the simulated heating rates at cloud base for both of our bin and bulk simulations are lower than that of the published values. However, the bin values are a bit (+10%) closer to these results. For the cloud top cooling rates, we can see that the bulk result (-7.6 K/h) is in better agreement with the values published before the 90s, as they are as well below

-8 K/h. Contrary, the bin result (-8.4 K/h) is more in line with recently reported values, as these values mostly exceed 8 K/h in terms of absolute rate.

It has to be noted as well, that there is a large variance in the values of cooling rates published in *Table 1.*, which is much higher than the difference observed between the bin and bulk schemes (~10%). Nevertheless, it can be stated that there is a persistent underestimation of the published rates by the bulk scheme; whereas the bin scheme gives a rate well within the range of dispersion of the reported values. The extremes of the cooling rates at cloud top are recorded by those studies based on measurements: *Duda et al.* (1991) gives the lowest, and *Chai et al.* (2003) gives the highest number in absolute terms. This can be explained by the large errors due to observation equipment (pyrometers, *Stevens et al.*, 2003). In addition, the reason for this deviance might be in *Duda et al.* (1991) that they supposed that the shapes of net flux profiles in the clouds are similar even if liquid water contents are different, which is not correct (*Lábó and Geresdi*, 2016).

We also have to emphasize that the depth of the cooling layer at cloud tops is widely accepted to be between 20–50 m (*Ackerman et al.* 1995; *Bergot et al.*, 2007). In *Figs. 6a* and *b*, it is illustrated that the bin and bulk schemes both overestimate this range; nonetheless, the bin value is slightly closer (~80 m).

4. Application of the bin radiation scheme for fog

Whereas the liquid water content is around 0.5 g/kg in stratocumulus clouds, fogs contain less water, typically between 0.01 and 0.4 g/kg, with effective radius varying from 4 to 10 μm (*Chai et al.*, 2003; *Gultepe and Milbrandt*, 2007). As a result of lower *LWC*, longwave radiation profiles show a different profile inside the fog layer. We have examined this by assuming idealized gamma-profiles for both the bin and bulk schemes within a 1D fog layer, where the liquid water content was constant (0.1 g/kg), and the thickness of the layer was 100 m. The results of the simulations accomplished by the RRTMG LW model can be seen in *Fig. 7*.

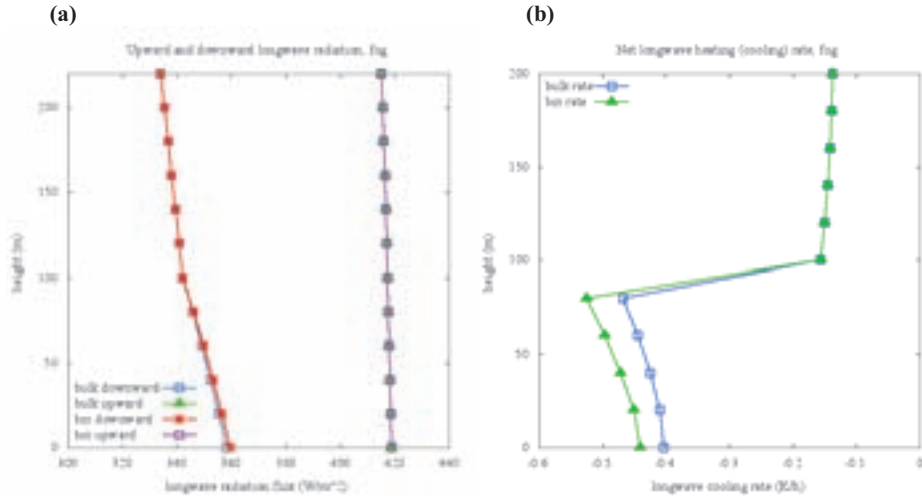


Fig. 7. Upward, downward (a) longwave radiation profiles and the cooling rates (b) in a fog layer for the bin and bulk radiation schemes.

We can see in *Fig. 7a*, that the difference of the net flux between the bin and bulk schemes at the surface is around $\sim 1.5 \text{ W/m}^2$, which is the consequence of larger absorbance by the bin method in the downward direction. The resulting maximum cooling rate within the cloud is -0.53 K/h for the bin scheme, and -0.47 K/h for the bulk scheme; which gives a total of 12% difference in the cooling rate. These rates are lower than published in *Koracin et al. (2001)* or *Wærsted et al. (2017)*, as they both studied fogs with much higher ($0.3\text{--}0.4 \text{ g/kg}$) liquid water content.

Because of the difference in bin and bulk rates, the absorption changes stronger with the altitude in case of the bin method, thus a more pronounced temperature inversion will form when using the bin model in a dynamical setting (*Gultepe et al., 2007*), which helps the fog to persist. Thus, longer lifetime of the fog can be predicted by the bin scheme in cold pool situations. Moreover, if the fog prevails, the energy balance at the surface is lower, as every minute $\sim 90 \text{ W/m}^2$ less energy reaches the ground in case of the bin scheme; which will considerably impact the soil-atmosphere interaction processes.

5. Conclusions

A new bin radiation scheme related to a bin microphysical scheme has been developed, and results about its application by using the RRTMG LW longwave radiation-transfer model are presented. The MADT approximation was used for calculation of radiation-water drop interaction in the new scheme to produce the bin longwave absorption coefficients for water clouds. The dependence of the coefficients on the wavelength confirmed that coefficients related to the bin scheme are in tune with the results of a so-called bulk radiation scheme currently used in operational numerical weather prediction models.

However, bin radiation scheme gave stronger radiation cooling rate than the bulk scheme at the top of the stratocumulus cloud. This distinction between the two schemes can be explained, partly, by the different approximation techniques used for calculation of absorption coefficients and mainly due to the different size distributions used in the two schemes. Even if same size distribution of water droplets was used in case of a fog layer, the cooling rates showed a divergence of 12%. We have also concluded that results of the new bin radiation scheme for marine stratocumulus clouds are improved compared to the bulk outcomes, as they are both closer to other published values of cooling/heating rates and those of depth of cooling region at cloud top.

The new method can currently be applied in simulations of fog occurrence and prediction of the lifetime of fog and water clouds. All numerical weather prediction models and their research versions which incorporate the RRTM LW radiation model are capable to use this new bin longwave radiation scheme, if number concentrations of water droplets in bin intervals are available as prognostic variable in the model. In such a case, the new radiation scheme does not require further computing resources. The new method can also be extended to other radiative transfer models, by calculation of relevant coefficients for the wavelength bands of the given radiative model.

Acknowledgements: The present study was supported by the Economic development and innovation operational program (project number: GINOP 2.3.2-15-2016-00055).

References

- Ackerman, A.S., Toon, O.B., and Hobbs, P.V., 1995: A Model for Particle Microphysics, Turbulent Mixing, and Radiative Transfer in the Stratocumulus-Topped Marine Boundary Layer and Comparisons with Measurements. *J. Atmos. Sci.*, 52, 1204–1236. [https://doi.org/10.1175/1520-0469\(1995\)052<1204:AMFPMT>2.0.CO;2](https://doi.org/10.1175/1520-0469(1995)052<1204:AMFPMT>2.0.CO;2)
- Allan, R.P., 2011: Combining Satellite Data and Models to Estimate Cloud Radiative Effect at the Surface and in the Atmosphere. *Meteorol. Apps.*, 18, 324–333. <https://doi.org/10.1002/met.285>
- Austin, P.H., Siems, S.T., and Wang, Y., 1995: Constraints on Droplet Growth in Radiatively Cooled Stratocumulus Clouds. *J. Geophys. Res. Atmos.*, 100(D7), 14231–14242. <https://doi.org/10.1029/95JD01268>

- Bergot, T., Terradellas, E., Cuxart, J., Mira, A., Liechti, O., Mueller, M., and Woetmann, N., 2007: Intercomparison of Single-Column Numerical Models for the Prediction of Radiation Fog. *J. Appl. Meteorol. Climatol.*, 46, 504–521. <https://doi.org/10.1175/JAM2475.1>
- Chai, S. K., Wetzel, M. A., and Koracin, D., 2003: Observed Radiative Cooling in Nocturnal Marine Stratocumulus. Fifth Conf. Coast. Atmos. Ocean. Predict. Process.
- Clough, S.A., Shephard, M.W., Mlawer, E.J., Delamere, J.S., Iacono, M.J., Cady-Pereira, K., Boukabara, S., and Brown, P. D., 2005: Atmospheric Radiative Transfer Modeling: A Summary of the AER codes, Short Communication. *J. Quant. Spectrosc. Radiat. Transf.*, 91, 233–244. <https://doi.org/10.1016/j.jqsrt.2004.05.058>
- Curry, J.A., 1986: Interactions among Turbulence, Radiation and Microphysics in Arctic Stratus Clouds. *J. Atmos. Sci.*, 43, 90–106. [https://doi.org/10.1175/1520-0469\(1986\)043<0090:IATRAM>2.0.CO;2](https://doi.org/10.1175/1520-0469(1986)043<0090:IATRAM>2.0.CO;2)
- Delamere, J.S., Mlawer, E.J., Clough, S.A., and Stammes, K.H., 2000: The impact of cloud optical properties on longwave radiation in the Arctic. In Tenth ARM Sci. Team Meet. Proc., San Antonio, Texas.
- Deng, A., Stauffer, D., Gaudet, B., Dudhia, J., Hacker, J., Bruyere, C., Wu, W., Vandenberghe, F., Liu Y., and Bourgeois, A., 2009: Update on WRF-ARW end-to-end multi-scale FDDA system. 10th Annu. WRF users' workshop. <http://www2.mmm.ucar.edu/wrf/users/workshops/WS2009/presentations/1-09.pdf>
- Duda, D.P., Stephens, G.L., and Cox, S.K., 1991: Microphysical and Radiative Properties of Marine Stratocumulus from Tethered Balloon Measurements. *J. Appl. Meteorol.*, 30, 170–186. [https://doi.org/10.1175/1520-0450\(1991\)030<0170:MARPOM>2.0.CO;2](https://doi.org/10.1175/1520-0450(1991)030<0170:MARPOM>2.0.CO;2)
- Fairall, C.W., Uttal, T., Hazen, D., Hare, J., Cronin, M.F., Bond, N., and Veron, D.E., 2008: Observations of Cloud, Radiation, and Surface Forcing in the Equatorial Eastern Pacific. *J. Clim.*, 21, 655–673. <https://doi.org/10.1175/2007JCLI1757.1>
- Fu, Q., Liou, K.N., Cribb, M.C., Charlock, T.P., and Grossman, A., 1997: Multiple scattering parameterization in thermal infrared radiative transfer. *J. Atmos. Sci.* 54, 2799–2812. [https://doi.org/10.1175/1520-0469\(1997\)054<2799:MSPITI>2.0.CO;2](https://doi.org/10.1175/1520-0469(1997)054<2799:MSPITI>2.0.CO;2)
- Gultepe, I. and Milbrandt, J.A., 2007: Microphysical Observations and Mesoscale Model Simulation of a Warm Fog Case During FRAM Project. *Pure Appl. Geophys.* 164, 1161–1178. <https://doi.org/10.1007/s00024-007-0212-9>
- Harrington, J. and Olsson, P.Q., 2001: A Method for the Parameterization of Cloud Optical Properties in Bulk and Bin Microphysical Models. Implications for Arctic Cloudy Boundary Layers. *Atmos. Res.*, 57, 51–80. [https://doi.org/10.1016/S0169-8095\(00\)00068-5](https://doi.org/10.1016/S0169-8095(00)00068-5)
- Hu, Y.X. and Stammes, K., 1993: An Accurate Parameterization of the Radiative Properties of Water Clouds Suitable for Use in Climate Models. *J. Clim.*, 6, 728–742. [https://doi.org/10.1175/1520-0442\(1993\)006<0728:AAPOTR>2.0.CO;2](https://doi.org/10.1175/1520-0442(1993)006<0728:AAPOTR>2.0.CO;2)
- Koracin, D., Lewis, J., Thompson, W.T., Dorman, C.E., and Businger, J.A., 2001: Transition of Stratus into Fog along the California Coast: Observations and Modeling. *J. Atmos. Sci.* 58, 1714–1731. [https://doi.org/10.1175/1520-0469\(2001\)058<1714:TOSIFA>2.0.CO;2](https://doi.org/10.1175/1520-0469(2001)058<1714:TOSIFA>2.0.CO;2)
- Lábó E. and Geresdi I., 2013: Application of a Detailed Bin Scheme in Longwave Radiation Transfer Modeling. *Időjárás* 117, 377–402.
- Lábó E. and Geresdi I., 2016: Study of Longwave Radiative Transfer in Stratocumulus Clouds by Using Bin Optical Properties and Bin Microphysics Scheme. *Atmos. Res.* 167, 61–76. <https://doi.org/10.1016/j.atmosres.2015.07.016>
- Lábó E., 2017: A hosszúhullámú sugárzás stratocumulus felhőben történő terjedésének numerikus modellezése, PhD dissertation, ELTE University, <https://edit.elte.hu/xmlui/handle/10831/35125>. (In Hungarian)
- Larson, V.E., Kotenberg, K.E., and Wood, N.B., 2007: An Analytic Longwave Radiation Formula for Liquid Layer Clouds. *Mon. Weather Rev.* 135, 689–699. <https://doi.org/10.1175/MWR3315.1>
- Lee, S.S. and Donner, L.J., 2011: Effects of Cloud Parameterization on Radiation and Precipitation: A Comparison between Single-Moment Microphysics and Double-Moment Microphysics. *Terr. Atmos. Ocean. Sci.* 22, 403–420. [https://doi.org/10.3319/TAO.2011.03.03.01\(A\)](https://doi.org/10.3319/TAO.2011.03.03.01(A))

- Mazoyer, M., Lac, C., Thouron, O., Bergot, T., Massonv, V., and Musson-Genon, L., 2017: Large eddy simulation of radiation fog: impact of dynamics on the fog life cycle. *Atmos. Chem. Phys.* 17, 13037–13035. <https://doi.org/10.5194/acp-17-13017-2017>
- McFarlane, S.A., Long, C.N., and Flaherty, J., 2013: A Climatology of Surface Cloud Radiative Effects at the ARM Tropical Western Pacific Sites. *J. Appl. Meteorol. Climatol.* 52, 996–1013. <https://doi.org/10.1175/JAMC-D-12-0189.1>
- Mitchell, D.L., 2000: Parameterization of the Mie Extinction and Absorption Coefficients for Water Clouds. *J. Atmos. Sci.* 57, 1311–1326. [https://doi.org/10.1175/1520-0469\(2000\)057<1311:POTMEA>2.0.CO;2](https://doi.org/10.1175/1520-0469(2000)057<1311:POTMEA>2.0.CO;2)
- Mlawer, E.J., Taubman, S.J., Brown, P.D., Iacono, M.J., and Clough, S.A., 1997: Radiative Transfer for Inhomogeneous Atmospheres: RRTM, A Validated Correlated-k Model for the Longwave. *J. Geophys. Res.*, 102(D14), 16,663–16,682. <https://doi.org/10.1029/97JD00237>
- Morcrette, J.-J., Barker, H., Cole, J., Iacono, M., and Pincus, R., 2008: Impact of a new radiation package, McRad, in the ECMWF Integrated Forecasting System. *Mon. Weather Rev.* 136, 4773–4798. <https://doi.org/10.1175/2008MWR2363.1>
- Oliver, D.A., Lewellen, W.S., and Williamson, G.G., 1978: The Interaction between Turbulent and Radiative Transport in the Development of Fog and Low-Level Stratus. *J. Atmos. Sci.*, 35, 301–316. [https://doi.org/10.1175/1520-0469\(1978\)035<0301:TIBTAR>2.0.CO;2](https://doi.org/10.1175/1520-0469(1978)035<0301:TIBTAR>2.0.CO;2)
- Olsen, L.D., 1996: Analysis of Infrared Heating Rates in Observed Cloud Layers. M. S. Thes., Colo. State Univ., Dept. of Atmos. Sci., Fort Collins. 620.
- Petters, J.L., Harrington, J.Y., and Clothiaux, E.E., 2012: Radiative–Dynamical Feedbacks in Low Liquid Water Path Stratiform Clouds. *J. Atmos. Sci.*, 69, 1498–1512. <https://doi.org/10.1175/JAS-D-11-0169.1>
- Petty, G.W., 2006: A First Course in Atmospheric Radiation. Madison, Wis., Sundog Pub.
- Pyrina, M., Hatzianastassiou, N., Matsoukas, C., Fotiadi, A., Papadimas, C.D., Pavlakis, K.G., and Vardavas, I., 2015: Cloud Effects on the Solar and Thermal Radiation Budgets of the Mediterranean Basin. *Atmos. Res.*, 152, 14–28. <https://doi.org/10.1016/j.atmosres.2013.11.009>
- Ramanathan, V., Cess, R.D., Harrison, E.F., Minnis, P., Barkstrom, B.R., Ahmad, E., and Hartmann, D., 1989: Cloud-Radiative Forcing and Climate: Results from the Earth Radiation Budget Experiment. *Science, New Series.*, 243, 4887, 57–63. <https://doi.org/10.1126/science.243.4887.57>
- Stevens, B., Lenschow, D.H., Vali, G., Gerber, H., Bandy, A., Blomquist, B., Brenguier, J.-L., Bretherton, C.S., Burnet, F., Campos, T., Chai, S., Faloona, L., Friesen, D., Haimov, S., Laursen, K., Lilly, D.K., Loehrer, S.M., Malinowski, S.P., Morley, B., Petters, M.D., Rogers, D. C. Russell, L., Savic-Jovicic, V., Snider, J.R., Straub, D., Szumowski, M.J., Takagi, H., Thornton, D.C., Tschudi, M., Twohy, C., Wetzell, M., and van Zanten, M.C., 2003: Dynamics and chemistry of marine stratocumulus—DYCOMS-II. *Bull. Amer. Meteor. Soc.*, 84, 579–593. <https://doi.org/10.1175/BAMS-84-5-Stevens>
- Sun, R., Moorthi, S., Xiao, H., and Mechoso, C.R., 2010: Simulation of low clouds in the Southeast Pacific by the NCEP GFS: sensitivity to vertical mixing. *Atmos. Chem. Phys.* 10, 12261–12272. <https://doi.org/10.5194/acp-10-12261-2010>
- Wærsted, E.G., Haeffelin, M., Dupont, J.-C., Delanoë, J., and Dubuisson, P.: Radiation in fog: quantification of the impact on fog liquid water based on ground-based remote sensing. *Atmos. Chem. Phys.* 17, 10811–10835. <https://doi.org/10.5194/acp-17-10811-2017>
- Wood, R., 2012: Stratocumulus Clouds. *Mon. Weather Rev.*, 140(8), 2373–2423. <https://doi.org/10.1175/MWR-D-11-00121.1>
- Yessad, K., 2014: Basics about ARPEGE/IFS, ALADIN and AROME in the cycle 41 of ARPEGE/IFS. <http://www.cnrm.meteo.fr/gmapdoc/IMG/pdf/ykarpbasics41.pdf>, 2014

IDŐJÁRÁS

Quarterly Journal of the Hungarian Meteorological Service
Vol. 123, No. 2, April – June, 2019, pp. 165–181

Weather model fine-tuning with software container-based simulation platform

Róbert Lovas¹, Péter Kardos², András Zénó Gyöngyösi*³, and Zsolt Bottyán⁴

¹*Institute for Computer Science and Control, Hungarian Academy of Sciences
H-1132 Budapest, Victor Hugo u. 18-22., Hungary*

²*HungaroControl, Hungarian Air Navigation Services Pte. Ltd. Co.
H-1185 Budapest, Igló u. 33-35., Hungary*

³*Department of Climatology and Landscape Ecology, University of Szeged
H-6722 Szeged, Egyetem u. 2., Hungary*

⁴*Institute of Military Aviation, National University of Public Service
H-1083 Budapest, Ludovika ter 2., Hungary*

*Corresponding Author E-mail: zeno@nimbus.elte.hu

(Manuscript received in final form October 26, 2018)

Abstract— Fine-tuning of a weather model requires immense computational resources, however, such capacities are usually available on non-homogeneous IT platforms. In addition, development and operational application are typically performed on different, heterogeneous systems (from laptops to dedicated HPC servers or cloud computing environments). To manage scalability and platform independent portability, a new layer – supporting state-of-the-art software container technology and batch processing – has been introduced. Encouraged by prior successful benchmark tests of the WRF model, the effect of model setup has been investigated over 10 different cases, tested on 30 different configurations. Including different parameterizations, the results of 300 different runs can be compared in a uniform database, yielding a sufficiently wide pool of samples in order to obtain the configuration of the modeling system optimal to the scope of our research, based on a relatively objective selection method. Continuously expanding database of near real-time preliminary outputs gives the opportunity for run-time steering of the experiments. This research currently benefits the development of an aviation meteorological support system, in the meanwhile, our contributions could be applied in an even wider aspect, either from the applicability of big data technology point of view, or with respect to the given best practice model setup.

Key-words: aviation meteorology, WRF model parameter optimization, docker software container technology, high performance computing, cloud computing

1. Introduction

All research that includes any kind of numerical weather modeling generally faced the nuisance of its immense computational requirement (see Section 2). This paper addresses the question whether there is a comfortable way to manage this computational background with significantly less manual effort instead of deep mining to benchmarking of various HPC (high performance computing) platforms, meanwhile the researchers can focus on their real expertise of meteorological details.

On the other hand, there is a fundamental change in the approach on HPC platform point of view. Many applications of such computing resources now based on cloud computing (*Mell and Grance, 2011*) environments that provide flexible and affordable solutions. Moreover, we are the witnesses of spreading of lightweight software container-based technologies (see Sections 3.1. and 3.2.). Such technologies enable easy portability, encapsulation, and management of complex software stacks and long-running simulation scenarios, such as fine-tuning of numerical weather modeling. The first part of the paper covers the meteorological modeling background and findings, followed by the description of the applied virtualized and container-based software and hardware platform in details (see Section 3.3.).

Meanwhile, there is a new challenge for meteorologist community, as there is a worldwide soaring of unmanned aerial systems (UAS) which includes various types of unmanned aerial vehicles (UAV) from the bee-sized to 10 meters wingspan drones, their ground based controllers, and finally, the two-way air-to-ground communication infrastructure as well. These systems need various meteorological information about several atmospheric features depending on specific operational threshold of the specific aerial vehicles (e.g., wind speed, humidity), or the details of their missions (e.g., visibility, cloud cover, sun radiation, etc.).

In the framework of the recent research activity, a meteorological support system has been developed for UAS operations (*Bottyán et al., 2013, 2014, 2015, 2017; Tuba et al., 2013; Bottyán, 2017; Tuba and Bottyán, 2018*). The information is represented in such a manner that the users (including UAV operators, decision makers, etc.) may interpret (or decode) them correctly and easily, such as diagrams, charts, and reports in common coded formats. Information is delivered to the user in a fast, convenient, and accessible way that does not require experience in the use of any special software or hardware. Products are published on the public domain of the computing server itself, through web applications. Outputs can be accessed by any web browser, with even hand-held mobile devices, or even on remote sites with low band data link coverage. Besides actual predictions, the server also provides archive NWP and observed data at each location (if available) for comparison by analogy purposes.

The weather engine of the system is the 3.9 version of the open source, community developed Weather Research and Forecasting (WRF) model (Skamarock *et al.*, 2008), since it is flexibly scalable, proved to be usable for (even UAS) aviation meteorology purposes (Passner *et al.*, 2009), and capable to assimilate UAS observed weather data (Passner *et al.*, 2012; Jonassen *et al.*, 2012; Reen and Dumais, 2018) besides other applications from its broad range of functionalities. WRF has multiple choices of parameter options. Planetary boundary layer schemes, that have significant effect on the flow structure and turbulence near the surface and in the lower troposphere, have 13, while surface layer sub-models have 8 different options, but each PBL option can handle only 2–4 different surface layer parameterization, which limits the number of possible combinations. Microphysics parameterization for the treatment of the atmospheric water content that is crucial in cloud and precipitation formation and icing processes could be selected from 27 different choices. Cumulus convection parameterizations that represent deep (and shallow) convection including thunderstorm development have 14 different options. Land surface model for the representation of processes in the soil layer, which provides lower boundary condition for the atmospheric variables has 7 choices available. Both long- and shortwave radiation have 8 different schemes, respectively, to consider radiation, which is crucial in the surface energy balance that governs processes close to the ground. Total count of all possible combinations (excluding unstable or prohibited combinations) is on the order of several hundred thousands.

However, the applicability of each scheme is well documented in the literature, and there are recommendations of working example combinations for given geographic locations (e.g., “CONUS” or “tropical” physics suites at the beginning of the WRF ARW Version 3.9) because of the complex interactions of all the parameterizations applied in the model, the optimal combination for a given location, application (or even meteorological situation) may be chosen by trial and error.

Although the operational weather prediction models of the Hungarian Meteorological Service are the ALADIN (Horányi *et al.*, 1996, 2006) and AROME (Seity *et al.*, 2011) models, WRF has also been extensively used and tested in various research projects in Hungary. WRF has been used in a diurnal analysis of shallow convection driven PBL height over dry soil in the Carpathian Basin (Acs *et al.*, 2014; Breuer *et al.*, 2014), in a comparison of microphysical schemes for the simulation of precipitation formation in convective clouds (Sarkadi, *et al.*, 2016), and in the evaluation of cloud seeding using a bin microphysics scheme (Geresdi *et al.*, 2017).

In addition, several additional studies were carried out to simulate severe storm activity in Hungary with the use of the WRF model (e.g., Csirmaz, 2015), but model sensitivity to horizontal resolution has mostly been tested and – according to our best knowledge – the effect of the choice of different parameterization setups and their interactions specifically in the Carpathian Basin

were not investigated yet, such as it has been done for the Continental US, Middle-East and North Africa (e.g., Zittis *et al.*, 2014), or for tropical regions (e.g., Pérez *et al.*, 2014; Noble *et al.*, 2014, 2017).

The actual parameter settings for our current (operational) setup has been obtained through an extensive testing and evaluation process using conventional HPC methods, i.e., model system has been run sequentially with different options, for different cases, and the scores of each run were evaluated afterwards in order to select the best setup (Gyöngyösi *et al.*, 2013). This process took for months and used the operative modeling platform prior to public deployment of the system. Operative application of the preliminary system is being run four times per day on the platform of the National University of Public Service, Institute of Military Aviation. In addition, the model system has been successfully set up and tested in our docker container-based virtual machine environment. This architecture provides additional computing resources for further calibration thereof.

2. Model setup and meteorological results

2.1. Applied model configurations

All tests were performed on the Version 3.9 of the WRF model. The initial and 3-hourly boundary conditions were preprocessed from 0.25 degree resolution GFS model outputs. The model domain and the applied high resolution nest have been tailored for the needs of an operative UAS meteorological support. Parent domain (d01) has 91×75 cells at 9 km horizontal resolution, centered at $N47.1^\circ$ and $E019.3^\circ$. Nested domain (d02) contains 196×136 cells at 3 km resolution, covering the territory inside the state border of Hungary. Vertical levels were explicitly set at 30 σ -levels, with $\sigma_1 = 0.999$ resulting in a lowest model level height $z_1 = 4$ meters AGL following the method suggested by Shin *et al.*, (2012). Time series output of only the d02 nested domain was evaluated against observation data. However, operational integrations are performed every 6 hours on a 96-hour lead time, test runs for evaluation were carried out for 36-hour lead time each, initialized at 12Z on the previous day of interest, and the first 12-hour output were dropped as spin-up.

To keep the number of possible model settings on a manageable level, we have focused on those parameters which have significant impact on results and are crucial for our present purpose. Therefore, microphysics (MP), planetary boundary layer physics (PBL), surface layer physics (SFC), and cumulus schemes (CU) were altered in an appropriate manner (see *Table 1* for the definitions of control file “*namelist*” options for each parameterization settings). In all cases, the very well established and widely used Noah Land Surface Model and RRTMG short- and longwave radiation schemes have been used. 14 different quality microphysics schemes were compared from the old and rather simplified representation of cloud and precipitation formation (such as Kessler or WSM3) to

the newest development of cloud microphysics (e.g., Thompson or P3). In addition, 4 cumulus and 3 PBL schemes were tested concurrently. Only those combinations were applied which are well documented, and that resulted in stable model run and results. The option for tropospheric wind (TOPO) is only available for the Yonsei University’s PBL scheme, which has also been tested in the fine-tuning. Remaining settings (domain configurations, spatial resolution, static inputs, soil texture and landuse, preprocessing methods, initialization, etc.) were kept identical for all ensemble members. Note that we do not refer hereby to the documentation of each single parameterizations, however, they are all well described in the already referenced description of WRF (*Skamarock et al., 2008*), or the corresponding source reference that can be found there. Altogether 30 different setups (treated as 30 members of an ensemble integration – ENS) have been loaded into our CQueue (i.e., container queue, see Sections 3.1 and 3.2 for more details) system for processing (*Table 2*). Note that ENS member # 1 corresponds to the operational model setup, that has been taken from previous test results (*Gyöngyösi et al., 2013*).

Table 1. Microphysics (MP), Cumulus (CU) and Planetary Boundary Layer (PBL) schemes (and their respective namelist options) applied for model fine-tuning

MP	# CU	# PBL	#		
Kessler	1	Kain-Fritsch	1	YSU	1
WSM 3-class simple ice	3	BMJ	2	MYNN 2.5 level	5
WSM 5-class	4	Grell-Freitas	3	Bretherton-Park/UW	9
Eta (Ferrier)	5	New Grell (G3)	5		
WSM 6-class graupel	6				
Goddard GCE	7				
New Thompson graupel	8				
Milbrandt-Yau 2-mom	9				
Morrison 2-mom	10				
CAM V5.1 5-class	11				
WRF 2-mom 5-class	14				
NSSL 2-mom	17				
NSSL Gilmore	21				
P3 1-category	50				

Table 2. Ensemble members definition

ENS	1	2	3	4	5	6	7	8	9	10	11	12	13	14	15
MP	4	3	3	3	3	1	4	1	5	6	7	8	9	10	11
SFC	1	1	1	5	1	1	1	1	1	1	1	1	1	1	1
PBL	1	1	1			5	9	1	1	1	1	1	1	1	1
CU	1	1	1	1	1	2	2	2	2	2	2	2	2	2	2
topo	2	0	2	0	0	0	2	2	0	0	0	0	0	0	0
ENS	16	17	18	19	20	21	22	23	24	25	26	27	28	29	30
MP	14	50	1	6	11	17	5	6	7	8	9	10	11	21	50
SFC	1	1	1	1	1	1	1	1	1	1	1	1	1	1	1
PBL	1	1	1	1	1	1	1	1	1	1	1	1	1	1	1
CU	2	2	3	3	3	3	5	5	5	5	5	5	5	5	5
topo	0	0	2	0	0	0	0	0	0	0	0	0	0	0	0

2.2. Evaluation method and results

For the sake of an efficient fine-tuning, various weather situations have been considered for simulation. Ten days with such weather that has adverse effect on aviation safety (e.g., freezing rain, snow, fog, low ceiling, and thunderstorm) were picked up from recent records. Dates and corresponding significant weather are summarized in *Table 3*. All cases refer to a period of 24 hours, exactly equal to a calendar day from 00:00Z to 24:00Z.

Table 3. Case study dates tested in parameterization fine-tuning

Description	Date
Warm front with freezing rain, following a long, extremely cold period	January 31, 2017
Severe freezing rain caused by a warm front	February 1, 2017
Off-season snow in spring	April 19, 2017
Freezing day with thunderstorms	May 3, 2017
Fog, low ceiling, freezing rain before the arrival of a cold front	January 17, 2018
Mild snowy day	February 20, 2018
Cold day with snows	February 28, 2018
Snow to freezing rain transition in the evening	March 2, 2018
Off-season dense fog	March 28, 2018
Early summer day with lifted nocturnal convection	May 2, 2018

All ensemble members were run for all cases resulting in 300 jobs altogether that were pushed into our CQueue worker for processing. Time series output at the location of each surface synoptic weather station and airport (34 stations altogether) within d02 were re-sampled every 5 minutes, converted from native model output variables (as model coordinate wind components or water vapor mixing ratio) into observation variables (wind direction and speed, dew-point) and pushed through CQueue system into a database for further processing (see Fig. 5). Prior to the whole procedure, this database has been filled up with archive surface observation data as well, so model forecasts and observation data were comparable on the SQL database level. In addition, 3-hourly input weather data from the driver GFS model, interpolated to the location of synoptic stations were also filled into the database for comparison and background (reference) model error assessment purposes. Both GFS and WRF model data were compared against observations available in time and space for the following variables: 2-meter temperature (T_{2m}), 2-meter dew point (Td_{2m}), and 10-meter wind speed (ws_{10m}). Although in most of the investigated cases, precipitation was a significant phenomenon, we have excluded this parameter from the verification formula, since there were lot of observations considered from stations without a reliable precipitation data, so the errors yielded by precipitation comparisons would significantly distort the evaluation. In addition, while T_{2m} , Td_{2m} , and ws_{10m} measurements were available on an hourly basis, precipitation data cycles were different, making uniform evaluation problematic.

The comparison method was kept simple but may be improved easily by changing the query evaluation formula and reprocessing the database in a real-time manner on the fly within a mean of several seconds of database processing time. The method used currently is based on the square WRF model error compared to the square GFS input error, yielding positive increment for improvement and negative for worsening WRF model performance compared to the input driver GFS skills. These increments were averaged over observations ($h \in \{3, 6, 9, 12, 15, 18, 21, 24\}$ as GFS provided data for these time steps) on a given day ($d \in [1..D]$; $D = 10$) for all s stations ($s \in [1..S]$; $S = 34$) to yield one single (overall) $Re(p)$ error score for a given $e \in [1..E]$; $ES = 30$ ensemble member (setup) for a given $p \in \{T_{2m}, Td_{2m}, ws_{10m}\}$ parameter as defined in the following equation:

$$Re(p) = \frac{1}{D \cdot S \cdot H} \sum_{d=1}^D \sum_{s=1}^S \sum_{h=0}^H \left[\left(F_{d,s,h}^{GFS}(p) - O_{d,s,h}(p) \right)^2 - \left(F_{d,s,h,e}^{WRF}(p) - O_{d,s,h}(p) \right)^2 \right], \quad (1)$$

where F stands for GFS or WRF forecast data (as indicated in the superscript) and O stands for observations, respectively.

An overall error score has been introduced by simply summing up the parameter error scores yielding one single score for a given ensemble member for the overall comparison.

$$S_e = \sum_p R_e(p), \tag{2}$$

where S_e is the overall error score.

Comparison of S_e overall error scores are presented in *Fig. 1* on a box-plot diagram, showing significant improvement in model skills for most of the ensemble members. The \times crosses represent means (most of them are above zero, indicating positive added value of WRF downscaling), horizontal lines are medians (all of them are above zero, showing that in most of the cases, the WRF results are closer to observations than the interpolated GFS data), vertical intervals show the absolute spread of skill scores, while boxes represent the inter-quartile range (IQR) of the deviations. In some cases, high positive outliers (those data which hit IQR threshold by more than $1.5 \times$ IQR are represented by individual dots) are indicating extraordinarily positive results, as for ensemble members #14, #17, #22, #26, and #30, while both absolute and IQR spreads are small by positive means and medians. It can be noted that current operational setup (ensemble member #1) yields mainly positive improvement compared to the simple interpolation of GFS fields, however, many other setups provide significantly better results in most cases. All WRF members yielded at least one result that performed poorer than GFS, and in most setups both absolute and IQR spreads are significant. Best results were yielded by ensemble members #15 and #20 (highest mean and median scores), while the best IQR and absolute ranges were yielded by ensemble members #17 and #30 (most reliable setups with low spreads).

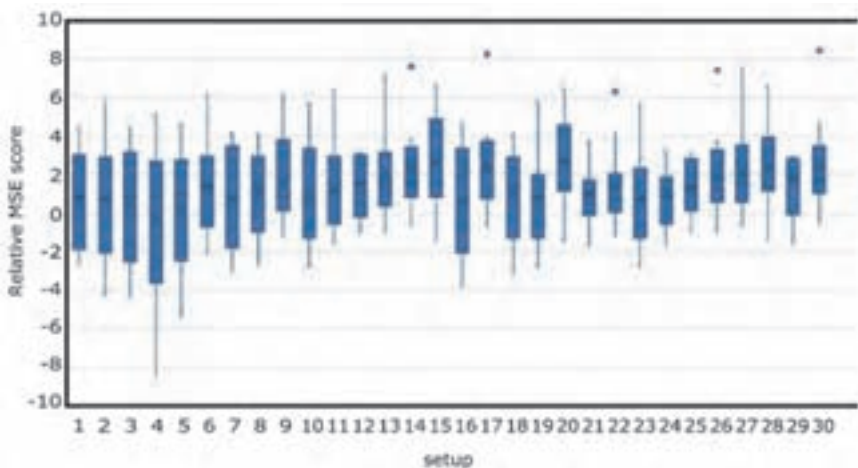


Fig. 1. Overall error scores for each ensemble member means (crosses), medians (horizontal lines), absolute spreads (vertical line intervals), IQR ranges (boxes), and $> 1.5 \times$ IQR outliers (dots).

In order to analyze the source of the large spread in the overall scores, the squared error differences have been summed up for e ensemble members instead of d cases as formulated in Eq.(3), which yielded the $R_d(p)$ error of the day parameter. The box-diagram of the error-of-the-day scores (in a similar manner to the overall error score box-plots, Fig. 2) shows high absolute and IQR spreads only for snow-to-freezing-rain-transition cases (January 1, 2017 and March 2, 2018), and relatively narrow positive results besides. The highest improvements compared to the GFS skills were yielded on April 19, 2017 (the “off-season-snow-in-spring” case). This indicates the possibility of the source of model errors to be sensitive to inverse lapse rate situations. In such cases, however, the assimilation of further (e.g., UAS-based) vertical profile measurements from the boundary layer with higher horizontal, vertical, and time resolution may significantly improve the forecast skills.

$$R_d(p) = \frac{1}{E \cdot S \cdot H} \sum_{e=1}^E \sum_{s=1}^S \sum_{h=0}^H \left[\left(F_{d,s,h}^{GFS}(p) - O_{d,s,h}(p) \right)^2 - \left(F_{d,s,h,e}^{WRF}(p) - O_{d,s,h}(p) \right)^2 \right]. \quad (3)$$

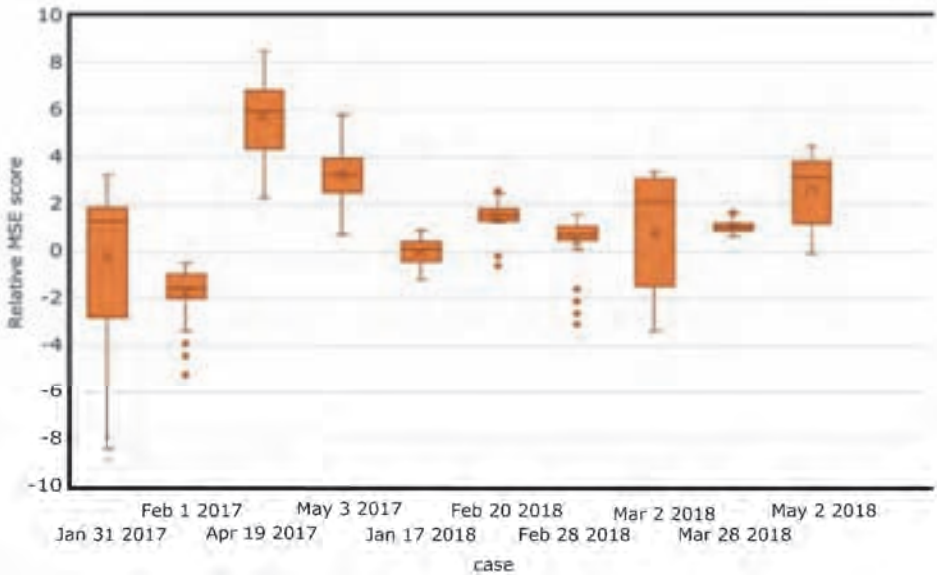


Fig. 2. Same as Fig. 1 for errors of the day showing less spread and higher added value for most cases besides two snow-to-freezing-rain-transition days on January 31, 2017 and March 2, 2018.

By the evaluation of the above results it can be concluded, that the value added by the costly high-resolution downscaling of global model results highly depends on the case selected, rather than the parameterization settings chosen. So in order to find the optimal parameterization, one order of magnitude higher number of cases should be considered instead of increasing the number of setups. In addition, evaluation formula which takes into account integral parameters (i.e., CAPE, CIN, precipitable water, etc.) or non-dimensional quantities for the evaluation of profile data instead of solely surface data comparison should be considered for the sake of a model system that is reliable for aviation (say 3 dimensional) purposes. Moreover, fine-tuning of model settings other than physical parameterizations (such as nesting, vertical resolution, data assimilation and dynamical options) may also be taken into account.

3. Applied container-based cloud computing platform

3.1. Docker containers for portability

Docker technology is the most rapidly spreading open-source software container platform (www.docker.com). It simplifies the software dependency handling, and ensures portability between different hardware, platforms, operating systems, and architectures, while supporting secure and agile deployment of new features. For the purposes of easy involvement of computing resources, the most important factor is portability, which simplifies the setting up of the environment on a wide variety of host machines in physical and cloud environments.

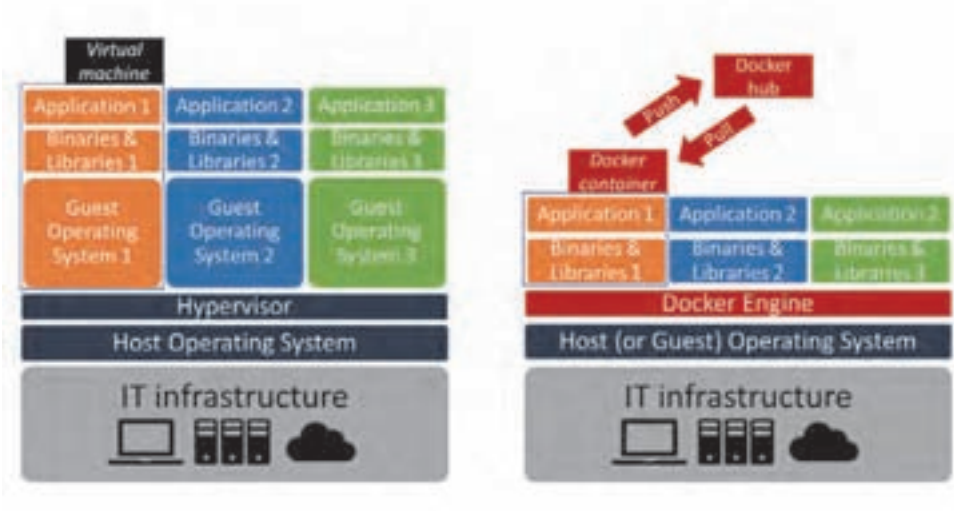


Fig. 3. Comparison of traditional operating system virtualization with Docker software container technology including Docker hub for publishing and storing images.

Docker images encapsulate environment settings and implement software dependencies (e.g., binaries and libraries) through inheriting other images. *Fig. 3* presents a comparison between the traditional operating system virtualization and the Docker software container technology. Docker also provides a simple command line interface to manage, download (pull), and create new images by Docker engine, but further sophisticated tools are also available for complex, workflow-oriented, and orchestrated usage scenarios, such as the Occopus cloud and container orchestrator tool (*Kovacs and Kacsuk, 2018*).

A related work on performance measurement compares high performance computing resources in cloud and physical environment, with and without utilizing the Docker software container technology (*Vránics et al., 2017*). The results show that the performance loss caused by the utilization of Docker is 5–10%, which is negligible compared to the 10–15-fold improvement in deployment time. The comparison shows that the expected performance of cloud resources is slightly lower than the performance of physical systems.

3.2. CQueue container queue service

Since Docker does not provide pull model for tasks execution (its Swarm cluster approach uses push execution model), the new CQueue framework provides a lightweight queue service for processing tasks via application containers. The framework consist of four main components (see *Fig. 4*): (i) one or more CQueue server(s), which act(s) as frontend(s) and receive(s) the container based task requests; (ii) a queue server schedules the tasks requests for workers; (iii) CQueue workers that pull tasks from the queue server; and (iv) a key-value store that backups the state and the output of the finished tasks. Currently queuing is handled by RabbitMQ, and Redis is used as the key-value store. The frontend server and the worker components are written in golang and they have a shared code-base. All of the components are running inside Docker containers and can be scaled based on their utilization. The design goals of the framework is to use standard interfaces and components to create a generic job processing middleware.

The framework is built for executing Docker container, based tasks with their specific inputs. Environment variables and other input parameters can be specified for each container also. CQueue uses an unique ID to identify the pushed tasks, and the user has to specify it. The ID, the application container, and the inputs of the task must be specified in standard JSON (JavaScript Object Notation) format. The CQueue server receives the tasks via a REST-Like API. After this step, the server transforms the JSON formatted tasks to standard AMQP (Advanced Message Queuing Protocol) messages and pushes them to the queue server. The workers pull the registered tasks from the queue server via the same AMQP protocol and execute them. One worker process one task at a time. After the task is completed, the workers send a notification to the queue server and this task will

be removed from the queue. The worker continuously updates the status (*registered*, *running*, *finished*, or *failed*) of the task with the task’s ID in the key-value store. When the task is finished or failed, the worker stores the *stdout* and *stderr* of task in the key-value store as well. The status of a task and the result can be queried from the key-value store through the CQueue server. The output of the task is not processed, it is stored in the key-value store in its original format.

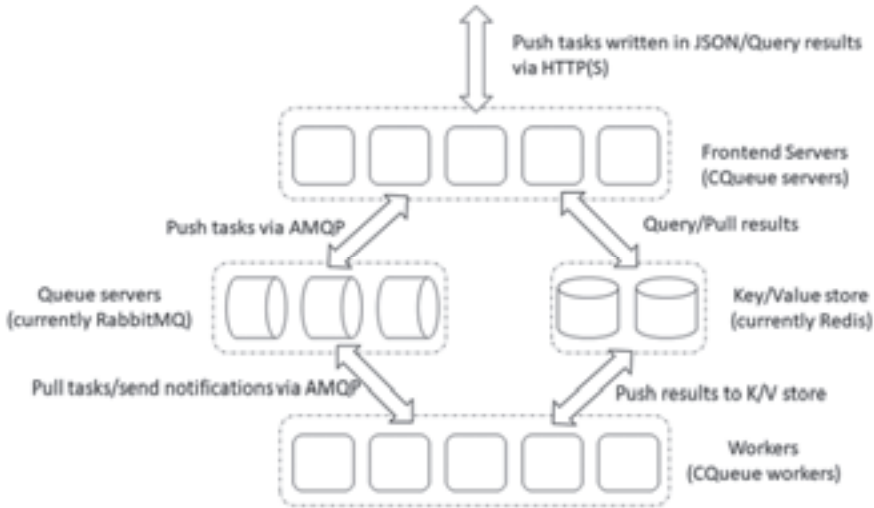


Fig. 4. CQueue architecture.

3.3. Virtualized architecture at large

As Fig. 5 depicts, resources have been involved from two Hungarian large-scale research infrastructures, MTA Cloud (cloud.mta.hu) and Agrodatt Cloud (agrodatt.hu) in order to execute the container based WRF simulations.

MTA Cloud is a federated community cloud, jointly operated by the MTA Wigner Data Center (WDC) and the Institute for Computer Science and Control (MTA SZTAKI). The recently opened OpenStack (Wen et al., 2012) and Docker container-based cloud infrastructures combine resources from WDC and MTA SZTAKI relying on the nationwide academic Internet backbone and other federated services, e.g., eduGain for authentication and authorization. The total capacity of the two deployed sites is 1160 virtualized CPU with 3.3 TB memory and 564 TB storage facility.

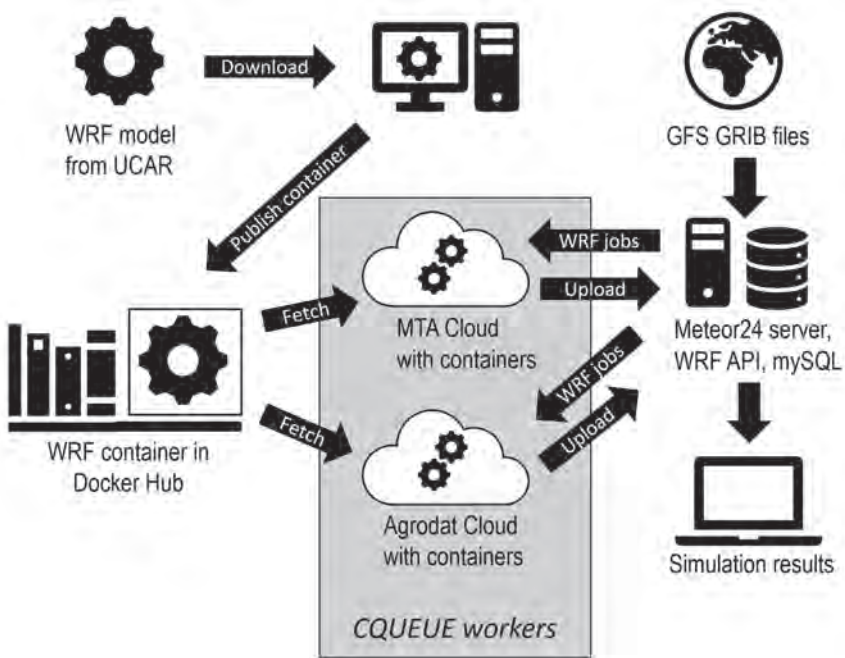


Fig. 5. The major components and their interactions of the elaborated IT architecture.

On the other hand, during the numerical weather modeling, the Agrodatt Cloud was used heavier, therefore, we introduce it with more details. The Agrodatt Cloud is a more specialized IaaS cloud, its main aim to support agriculture related research based on OpenNebula 5.2 cloud middleware (Moreno-Vozmediano *et al.*, 2012). The underlying virtualization technique is KVM (hardware virtualization), and storage is provided both by a Ceph (Weil *et al.*, 2006) distributed storage cluster and a QCOW2 store. Users can manage the cloud resources via browser based graphical interface (Sunstone) or via an EC2 interface. Additionally, an S3 based storage is part of the infrastructure (via RadosGW of Ceph). Currently 4 VM hosts (HPE ProLiant DL385p Gen8 and Dell PowerEdge R815 models) are allocated for the cluster with combined 144 CPU cores and 512GB RAM:

- Host 1: 2x AMD Opteron(tm) processor 6376 2.3GHz CPU (32 cores total), 128GB RAM,

- Host 2: 4x AMD Opteron(tm) processor 6262 HE 1.6GHz CPU (64 cores total), 256GB RAM,
- Host 3: 4x AMD Opteron(tm) processor 6164 HE 1.7GHz CPU (48 cores total), 128GB RAM.

Storage is available for the cluster as follows:

- 18.1TB QCOW2 storage,
- 31.5TB Ceph based distributed storage.

Networking is provided by Cisco Nexus 3548 (10Gb), and HP 5920 (10Gb Ethernet) switches. Ceph storage nodes are connected via 2x 10Gb Ethernet links to the network. Additionally, 1Gb Ethernet switches are used for management purposes.

On both clouds, the Docker container platform with CQueue (see Sections 3.1 and 3.2) enable the pull execution model for the fine-tuning of numerical weather modeling, i.e., each Cqueue worker on the launched virtual machines of the given cloud fetches the WRF jobs from the Meteor24 server one-by-one when worker becomes idle. It is also necessary to fetch the already prepared and published WRF container (see *Vranics et al., 2017*) from the public Docker Hub, but only once at the beginning of the simulation. The WRF jobs are prepared according to Section 2 using the data from the Global Forecasting System (GFS), and the progress and simulation results (stored in mySQL) can be accessed remotely. Total 300 jobs were added to CQueue system in our investigation. The average of 3 hour 38 minutes runtime of workers varies between 1 hour 14 minutes to 11 hours 59 minutes depending on which parameterization scheme was applied in that specific setting. As 8–12 virtual machines provided computing capacity for CQueue workers in our experiment at the same time, the total processing period was less than 8 days. Of course, because of the scalability of the whole system, it can be decreased significantly with involving more virtual machines in an easy manner.

4. Related works and conclusion

Comparing to the traditional parallel (multi-threaded or message passing-based) execution of modeling, our approach takes benefits of the distributed computing paradigm as well, even in heterogeneous computing environments. In this way, we leverage on the parallel execution inside the given multi-core computing node, but theoretically, arbitrary number of different executions are allowed at the same time in a distributed manner, involving further available computing nodes (e.g., traditional servers, cluster nodes, or virtual machines in the cloud). This type of

loosely coupled and heterogeneous systems require special methods and tools to handle the complex distributed management and software stack portability issues.

There are several software container and (mostly cloud-based) automatic management tools addressing the above described problems, such as the widely used Kubernetes (*Burns et al., 2016*) and Tosca (*Binz et al., 2014*). Recently, new emerging tools are also appearing in this field, such as MiCADO (*Kiss et al., 2017*) and Occopus (*Kovacs and Kacsuk, 2018*), for distributed execution of simulations. The enlisted tools are more feature-rich products, but CQueue became a proven and promising approach leveraging on the presented WRF results and further application areas (see its use case for Industry 4.0 by *Lovas et al., 2018*) since it is similarly robust distributed computing technology but having significantly lower entry-barrier for non-IT specialist and not steep learning curve comparing to its competitors.

Concerning WRF related containerization works, there are also related works, (*Hacker et al., 2017*) but (among others) they did not provide such convenient but at the same time very robust approach like our CQueue container queue oriented solution. This tool provided valuable results for our research project, and proved that it is an efficient way to manage this kind of fine tuning. As all results of finished jobs are available during the processing phase, we are able to add those new jobs into the schedule list which may serve promising additional information on the accuracy of various parameterization settings ensuring the effectiveness and time saving of the research project. Therefore, this tool is now ready to process plenty of jobs (magnitude of 1000) and to serve valuable information on appropriate parameterization settings for further research.

Acknowledgement: This work was supported by the European Regional Development Fund under Grant no. GINOP 2.3.2-15-2016-00007 (“Increasing and integrating the interdisciplinary scientific potential relating to aviation safety into the international research network at the National University of Public Service - VOLARE”). The project was realized through the assistance of the European Union, and co-financed by the European Regional Development Fund. On behalf of Project “Weather Research and Forecasting (WRF) - Benchmark & Orchestration” we thank for the usage of MTA Cloud that significantly helped us achieving the results published in this paper.

References

- Ács, F., Gyöngyösi, A.Z., Breuer, H., Horváth, Á., Mona, T., and Rajkai, K., 2014: Sensitivity of WRF-simulated planetary boundary layer height to land cover and soil changes. *Meteorol. Z.* 23, 279–293. Agrodatt.hu project website. Accessed: 2018-06-17. <https://doi.org/10.1127/0941-2948/2014/0544>
- Binz, T., Breitenbücher, U., Kopp, O., and Leymann, F., 2014: Tosca: Portable automated deployment and management of cloud applications. In *Advanced Web Services*. 527–549. Springer.
- Bottván, Zs., Wantuch, F., Gyöngyösi, A.Z., Tuba, Z., Hadobács, K., Kardos, P., and Kurunczi, R., 2013: Forecasting of hazardous weather phenomena in a complex meteorological support system for UAVs. *World Acad. Sci. Engin. Technol.* 7, 646–651.
- Bottván, Zs., Wantuch, F., and Gyöngyösi, A.Z., 2014: Forecasting of hazardous weather phenomena in a complex meteorological support system for UAVs. *J. Unman. Sys. Technol.* 2(2), 18–25.

- Bottyán, Zs., Gyöngyösi, A.Z., Wantuch, F., Tuba, Z., Kurunczi, R., Kardos, P., Istenes, Z., Weidinger, T., Hadobacs, K., Szabo, Z., Balczó, M., Varga, A., Birone Kircsi, A., and Horváth, Gy., 2015: Measuring and modeling of hazardous weather phenomena to aviation using the Hungarian Unmanned Meteorological Aircraft System (HUMAS). *Időjárás* 119, 307–335.
- Bottyán, Zs., 2017: On the theoretical questions of the uas-based airborne weather reconnaissance. In (Eds.: Bottyán, Zs., and Szilvássy, L.) *Repüléstudományi Szemelvények: A közfeladatot ellátó repülések meteorológiai biztosításának kérdései*. ISBN:978-615-5845-26-0, Nemzeti Közszolgálati Egyetem Katonai Repülő Intézet, Szolnok. 97–118.
- Bottyán, Zs., Tuba, Z., and Gyöngyösi, A.Z., 2017: Weather forecasting system for the unmanned aircraft systems (uas) missions with the special regard to visibility prediction, in Hungary. In (Eds. Nádaí L. and Padányi J.) *Critical Infrastructure Protection Research: Results of the First Critical Infrastructure Protection Research Project in Hungary*. Topics in Intelligent Engineering and Informatics; 12. ISBN:978-3-319-28090-5, 23–34. Springer International Publishing, Zürich.
- Breuer, H., Ács, F., Horváth, Á., Németh, P., and Rajkai, K.: Diurnal course analysis of the WRF-simulated and observation-based planetary boundary layer height. *Adv. Sci. Res.* 11, 83–88. (doi:10.5194/asr-11-83-2014)
- Burns, B., Grant, B., Oppenheimer, D., Brewer, E., and Wilkes, J., 2016: Borg, omega, and kubernetes. *Commun. ACM*, 59(5): 50–57. <https://doi.org/10.1145/2890784>
- Csirmaz, K., 2015: A new hail size forecasting technique by using numerical modeling of hailstorms: A case study in Hungary. *Időjárás* 119,443–474.
- Docker - Build, Ship, and Run Any App, Anywhere. <https://www.docker.com>, Accessed: 2017-10-30.
- Geresdi I, Xue L, and Rasmussen R., 2017: Evaluation of orographic cloud seeding using a bin microphysics scheme: Two-dimensional approach. *J App Met Clim.* 56, 1443–1462. <https://doi.org/10.1175/JAMC-D-16-0045.1>
- Gyöngyösi, A.Z., Kardos, P., Kurunczi, R., and Bottyán, Zs., 2013: Development of a complex dynamical modeling system for the meteorological support of unmanned aerial operation in Hungary. In *2013 International Conference on Unmanned Aircraft Systems (ICUAS): Conference Proceedings.*, 2013.05.28–2013.05.31. Atlanta (GA), ISBN: 978-1-4799-0815-8, 8–16, Atlanta, 2013. IEEE.
- Hacker, J.P., Exby, J., Gill, D., Jimenez, I., Maltzahn, C., See, T., Mullendore, G., and Fossell, K., 2017: A containerized mesoscale model and analysis toolkit to accelerate classroom learning, collaborative research, and uncertainty quantification. *Bull. Amer. Meteorol. Soc.*, 98, 1129–1138. <https://doi.org/10.1175/BAMS-D-15-00255.1>
- Horányi A., Ihász I. and Radnóti G., 1996: ARPEGE/ALADIN: a numerical weather prediction model for Central-Europe with the participation of the Hungarian Meteorological Service. *Időjárás* 100, 277–301.
- Horányi A., Kertész S., Kullmann L., and Radnóti G., 2006: The ARPEGE/ALADIN mesoscale numerical modeling system and its application at the Hungarian Meteorological Service. *Időjárás* 110, 203–227.
- Jonassen, M.O., Olafsson, H., Agustsson, H., Rognvaldsson, O., and Reuder, J., 2012: Improving high-resolution numerical weather simulations by assimilating data from an unmanned aerial system. *Mon. Weather Rev.* 140, 3734–3756. <https://doi.org/10.1175/MWR-D-11-00344.1>
- Kiss, T., Kacsuk, P., Kovacs, J., Rakoczi, B., Hajnal, A., Farkas, A., Gesmier, G., and Terstyanszky, G., 2017: Micado—microservice-based cloud application-level dynamic orchestrator. *Future Generation Computer Systems*. <https://doi.org/10.1016/j.future.2017.09.050>
- Kovács, J., and Kacsuk, P., 2018: Occopus: a multi-cloud orchestrator to deploy and manage complex scientific infrastructures. *J. Grid Comput.* 16, 19–37. <https://doi.org/10.1007/s10723-017-9421-3>
- Lovas, R., Farkas, A., Marosi, A.Cs., Ács, S., Kovacs, J., Szaloki, A., and Kadar, B., 2018: Orchestrated platform for cyber-physical systems. *Complexity* 2018, Article ID 8281079, 16 pages, <https://doi.org/10.1155/2018/8281079>
- Moreno-Vozmediano, R., Montero, R.S., and Llorente, I.M., 2012: IaaS cloud architecture: From virtualized datacenters to federated cloud infrastructures. *Computer*, 45, 65–72. <https://doi.org/10.1109/MC.2012.76>
- Mell, P. and Grance, T., 2011: The NIST definition of cloud computing. Technical Report SP 800-145, National Institute of Standards and Technology Gaithersburg, MD, United States.

- MTA Cloud. <https://cloud.mta.hu>, Accessed: 2018-06-18.
- Noble, E., Druyvan, L.M. and Fulakeza, M., 2014: The sensitivity of WRF daily summertime simulations over West Africa to alternative parameterizations. Part I: African wave circulation. *Mon. Weather Rev.* 142, 1588–1608. <https://doi.org/10.1175/MWR-D-13-00194.1>
- Noble, E., Druyvan, L.M., and Fulakeza, M., 2017: The sensitivity of WRF daily summertime simulations over West Africa to alternative parameterizations. Part II: precipitation. *Mon. Weather Rev.* 145, 215–233. <https://doi.org/10.1175/MWR-D-15-0294.1>
- Passner, J.E., Dumais jr., R.E., Flanigan, R., and Kirby, S., 2009: Using the Advanced Research version of the Weather Research and Forecast model in support of ScanEagle unmanned aircraft system test flights. ARL Technical Report ARL-TR-4746, Computational Information Sciences Directorate, U.S. Army Research Laboratory: White Sands Missile Range, NM.
- Passner, J.E., Kirby, S., and Jameson, T., 2012: Using real-time weather data from an unmanned aircraft system to support the Advanced Research version of the Weather Research and Forecast model. ARL Technical Report ARL-TR-5950, Computational Information Sciences Directorate, U.S. Army Research Laboratory: White Sands Missile Range, NM.
- Pérez, J.C., Díaz, J.P., González, A., Expósito, J., Rivera-López, F., and Taima, D., 2014: Evaluation of WRF parameterizations for dynamical downscaling in the Canary Islands. *J. Climate*, 27, 5611–5631. <https://doi.org/10.1175/JCLI-D-13-00458.1>
- Reen jr., R.E., and Dumais B.P., 2018: Assimilation of aircraft observations in highresolution mesoscale modeling. *Adv. Meteorol.* 2018. 1–16. <https://doi.org/10.1155/2018/8912943>
- Sarkadi N., Geresdi I., and Gregory T., 2016: Numerical simulation of precipitation formation in the case orographically induced convective cloud: Comparison of the results of bin and bulk microphysical schemes. *Atmos. Res.* 180, 241–261. <https://doi.org/10.1016/j.atmosres.2016.04.010>
- Seity Y., Brousseau P., Malardel S., Hello G., Bénard P., Bouttier F., Lac C., and Masson V., 2011: The AROME-France Convective-Scale Operational Model, *Mon. Weather Rev.* 139, 976–991. <https://doi.org/10.1175/2010MWR3425.1>
- Shin, H.H., Hong, S-Y., and Dudhia, J., 2012: Impacts of the lowest model level height on the performance of planetary boundary layer parameterizations. *Mon. Weather Rev.* 140, 664–682. <https://doi.org/10.1175/MWR-D-11-00027.1>
- Skamarock, W.C., Klemp, J.B., Dudhia, J., Gill, D.O., Barker, D.M., Duda, M.G., Huang, X-Y., Wang, W., and Powers, J.G., 2008: A description of the Advanced Research WRF version 3. NCAR Tech. Note NCAR/TN-475+STR, National Center of Atmospheric Research. doi:10.5065/d68s4mvh
- Tuba, Z., Vidnyánszky, Z., Bottyán, Zs., Wantuch, F., and Hadobács, K., 2013: Application of analytic hierarchy process in fuzzy logic-based meteorological support system of unmanned aerial vehicles. *Acad. Appl. Res. Military Sci.* 12, 221–228.
- Tuba Z. and Bottyán, Zs., 2018: Fuzzy logic-based analogue forecasting and hybrid modeling of horizontal visibility. *Meteorol. Atmos. Phys.* 130, 265–277. <https://doi.org/10.1007/s00703-017-0513-1>
- Vránics, D.F., Lovas, R., Kardos, P., Bottyán, Zs., and Palik, M., 2017: WRF benchmark measurements and cost comparison. virtualized environment versus physical hardware. *Repüléstudományi Közlemények*, 29, 257–272.
- Weil, S.A., Brandt, S.A., Miller, E.A., de Long, D., and Maltzahn, S., 2006: Ceph: A scalable, high-performance distributed file system. In Proceedings of the 7th symposium on Operating systems design and implementation. USENIX Association. 307–320.
- Wen, X., Gu, G., Li, Q., Gao, Y., and Zhang, X., 2012: Comparison of open-source cloud management platforms: Openstack and opennebula. 2457–2461.
- Zittis, G., Hadjinicolaou, P., and Lelieveld, J., 2014: Comparison of WRF Model Physics Parameterizations over the MENA-CORDEX Domain. *Amer. J. Clim. Change* 3, 490–511. <https://doi.org/10.4236/ajcc.2014.35042>

IDŐJÁRÁS

Quarterly Journal of the Hungarian Meteorological Service
Vol. 123, No. 2, April – June, 2019, pp. 183–202

Improving wintertime low level cloud forecasts in a high resolution numerical weather prediction model

Balázs Szintai^{1*}, Eric Bazile², and Yann Seity²

¹*Hungarian Meteorological Service*
Kitaibel Pál u. 1., H-1024 Budapest, Hungary

²*Météo-France*
42 av G Coriolis, 31057 Toulouse, France

*Corresponding author E-mail: szintai.b@met.hu

(Manuscript received in final form July 4, 2018)

Abstract—In this study, the performance of a high resolution numerical weather prediction (NWP) model is investigated in a particular weather situation, namely, in winter anticyclonic cases over land with low level clouds and fog. Most NWP models tend to underestimate low level cloudiness during these events which causes the overestimation of daytime temperature. Several sensitivity tests are performed to trace the cause of the erroneous model performance, and it is shown that model microphysics and, in particular, the autoconversion of cloud ice to snow is responsible for the underestimation of cloud cover. A modification is proposed which significantly reduces ice autoconversion and consequently keeps the low level clouds for situations with temperatures below freezing level. The modification is tested on several case studies and also on longer time intervals and proves to be applicable for operational model runs.

Key-words: numerical weather prediction, low level clouds, physical parameterization, cloud microphysics, ice autoconversion

1. Introduction

Simulating wintertime low level cloud cases is a challenging task for most operational numerical weather prediction (NWP) models. The difficulty of these situations from the modeling point of view is that several processes (radiation, turbulence, microphysics) are interacting to form the low level cloud layer. Recently, several modeling groups started to investigate these cases in more

details and proposed modifications to improve model performance. At the European Centre for Medium-Range Weather Forecasts (ECMWF), experiments concentrated on low level cloud cases over sea (*Ahlgrimm and Forbes, 2014*) and over high latitudes (*Forbes and Ahlgrimm, 2014*) and proposed several modifications in the boundary layer and shallow convection schemes and in the microphysics parameterization. Over the UK, during the 2014 Local and Non-local Fog Experiment (LANFEX, *Price et al., 2017*), observations and LES simulations have been used by the Met Office (*Boutle et al., 2018*) to improve the parameterization of cloud-droplets number in their UKV NWP model. In France, observations from the ParisFog (*Haeffelin et al., 2010*) campaign have been used to study the impact of surface heterogeneities (*Mazoyer et al., 2017*) at very high resolution with the Meso-NH model. A deposition term was added to the droplet sedimentation (representing the interception of droplets by the plant canopies), in order to have more realistic cloud water contents. At Météo-France, dedicated studies on fog have been performed with the AROME (*Seity et al., 2011*) model, such as *Philip et al. (2016)* who showed the impact of the model vertical resolution, and exhibited model deficiencies in cloud-base-lowering fog cases.

In this paper, the performance of the AROME model is investigated in winter anticyclonic cases over land. During strong winter anticyclones, cold air resides near the surface and no significant fronts occur which could sweep out the cold air from the Pannonian Basin. As solar irradiation is quite low in this season, the morning fog is not dissolved, it is only elevated to about 300-500 m above ground level, and a stratus layer is formed which stays constant during daytime. The elevation of the fog layer is basically caused by the high albedo of the cloud top, which causes the cloud top to cool even after sunrise. Consequently, condensation occurs at the cloud top and the fog starts to elevate. This kind of situation can typically last for 7–10 days over Hungary. Due to low wind speeds and constant cloudiness, the mixing height of pollutants is relatively low and the concentration of air pollutants can rise significantly. Generally, the AROME model – similarly to other NWP models applied at the Hungarian Meteorological Service (HMS) – is not very successful in simulating this weather phenomenon. The stratus layer tends to be dissolved by the model by early afternoon, and consequently, afternoon temperatures are overestimated and night temperatures are underestimated by the model.

2. Experimental setup and case study

For this study, the AROME non-hydrostatic high resolution model was used (*Termonia et al., 2018*). The development of AROME (Application of Research to Operations at Mesoscale) was initiated at Météo-France (*Seity et al., 2011*) at the beginning of the 2000's and is currently further developed in the ALADIN

and HIRLAM NWP modeling consortia. The AROME model has three main components: the non-hydrostatic ALADIN dynamical core (*Bubnová et al.*, 1995; *Benard et al.*, 2010), the atmospheric physical parameterizations, which are taken from the French Meso-NH research model (*Lafore et al.*, 1998), and the SURFEX surface model (*Masson et al.*, 2013). A mesoscale data assimilation system with a three-dimensional variational (3D-VAR; *Fischer et al.*, 2005) scheme for the upper-air and an optimum interpolation technique for the surface analyses provides reliable initial conditions for the AROME model.

At the Hungarian Meteorological Service, the AROME model is run operationally since 2010 (*Szintai et al.*, 2015; and model references therein). The model is integrated at 2.5 km horizontal resolution with 60 vertical levels and uses lateral boundary conditions from the IFS (Integrated Forecast System) model of ECMWF. The AROME assimilation system, using conventional observations (synop, radiosoundings, AMDAR), was operationally implemented in 2013 (*Mile et al.*, 2015).

The selected case study (November 30, 2011) was a late autumn day with stratus cover of nearly the whole Pannonian Basin. The simulation started at 00 UTC on November 30, 2011 and lasted 14 hours. In the reference simulation, initial and lateral boundary conditions for AROME were interpolated from the ARPEGE model, which is a global model run operationally at Météo-France (*Courtier et al.*, 1991).

Fig. 1 shows the ARPEGE and AROME forecasts and the satellite observations of low level cloud cover. At the start of the simulations both models diagnose the spatial extension of the fog well. As the simulation proceeds, both models erroneously dissolve the fog over the western part of Hungary. Over the eastern part of the country, ARPEGE keeps most of the low level clouds, while AROME dissolves a considerable part of the fog.

First, the performance of ARPEGE and AROME over the western part of Hungary was investigated. Over this area both models dissipate the fog and give wrong low level cloud forecasts. Vertical profiles of wind speed (*Fig. 2*) in AROME show that there is a substantial difference between the western and eastern parts of Hungary. Over the eastern part, wind at higher levels (i.e., at and above the height of the stratus layer) is constant or even decreasing during the simulation, while over the western part wind speed is increasing to about 14 m/s above the boundary layer. It is assumed that over the western part this strong wind increases the mixing in the model in the boundary layer and dissolves the fog/stratus. As this effect is considered to be a large scale phenomenon, in the following the investigation is focused on the eastern part of Hungary.

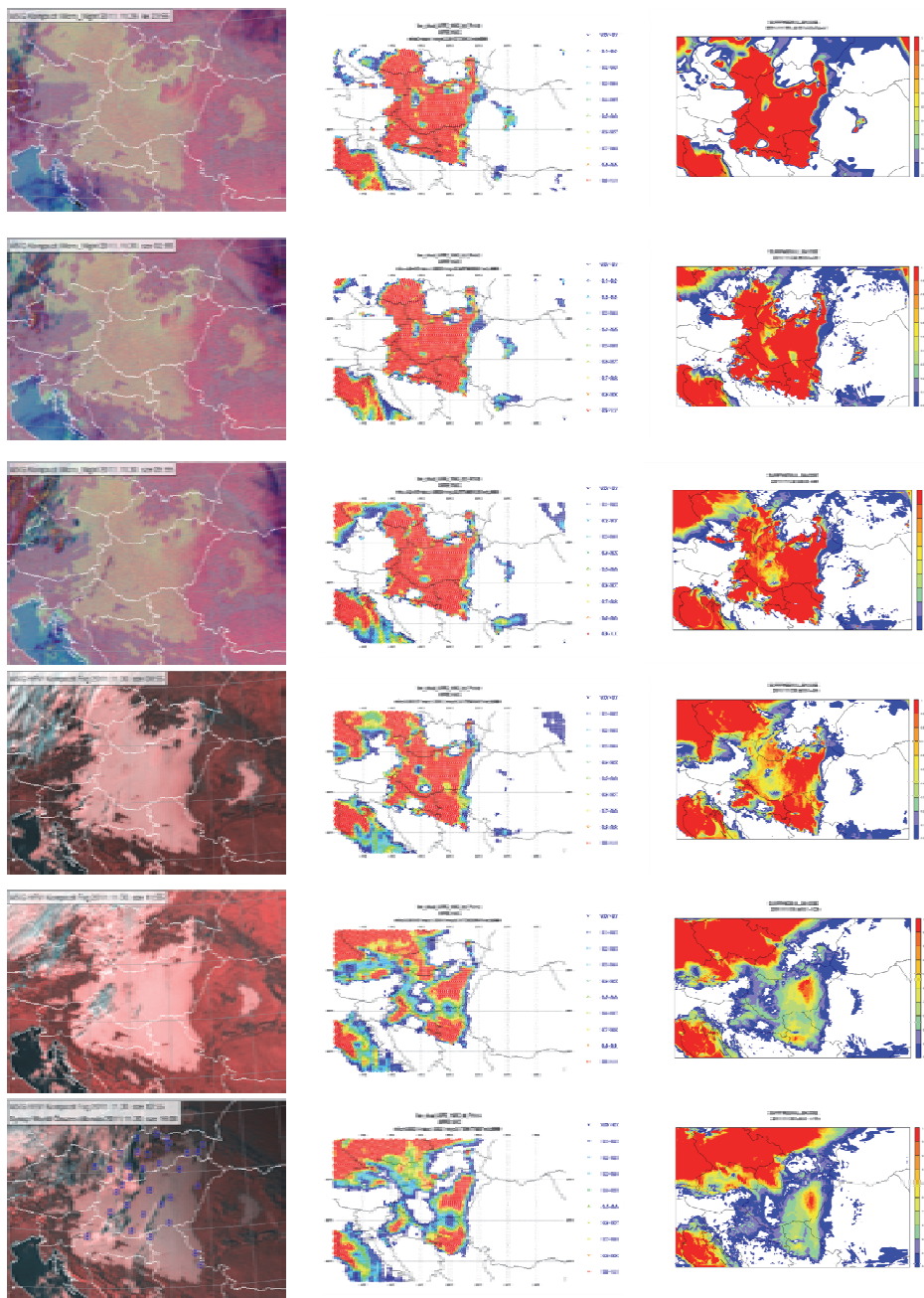


Fig. 1. Reference runs of the selected case study (November 30, 2011). Satellite observations (first column), ARPEGE (second column) and AROME (third column) forecasts of low level cloud cover. Each row refers to a single forecast time: 00 UTC (initial time), 03 UTC, 06 UTC, 09 UTC, 12 UTC, and 14 UTC. On the lower left picture, numbers indicate synop observations of low level cloudiness. For the model fields, white indicates no clouds, red indicates full cloud cover.

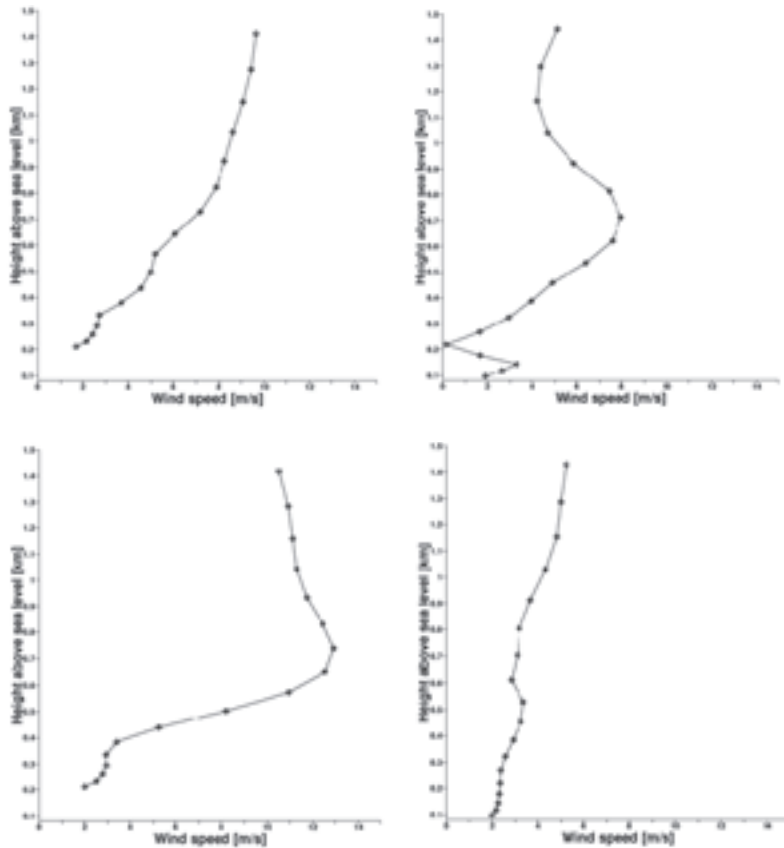


Fig. 2. Profiles of wind speed in AROME for a grid point in the western (left column) and eastern (right) parts of Hungary for November 30, 2011. Forecast range is +1h (01 UTC, upper row) and +14h (14 UTC, lower row).

3. Sensitivity tests

As a priori it was not known which of the processes involved (radiation, turbulence, microphysics) are responsible for the wrong forecast in the AROME model, several sensitivity tests were completed to diagnose the problem. These experiments are described in detail in the following.

The reference run was not using data assimilation, AROME was run in dynamical adaptation mode, i.e., the initial state was produced by interpolating the ARPEGE analysis to the AROME grid. In the first sensitivity test, the impact of data assimilation was tested. An assimilation cycle with 5-day spin-up was run for the selected case. In the atmosphere, the 3DVAR method was

applied using conventional (synop and radiosounding) observations, while on the surface, the optimal interpolation method (OI_MAIN) was applied. The application of data assimilation has an overall neutral but spatially variable impact on the low level cloud forecast in AROME (*Fig. 3a*).

The second sensitivity test aimed at quantifying the impact of lateral boundary conditions. In this experiment, boundary conditions from the ECMWF/IFS global model were used instead of the ARPEGE global model. Impact on the stratus cloud cover over Hungary was rather small (*Fig. 3b*).

The choice of the subgrid statistical cloud scheme has also been investigated. At the Hungarian Meteorological Service, a diagnostic formulation (*Sommeria and Deardorff, 1977*) is used operationally (used also in the reference run), while at Météo-France a prognostic one (*Chaboureau and Bechtold, 2002*). As experienced for several other case studies, the prognostic formulation gives much less low level clouds and tends to produce a low level cloud cover value of “zero or one”. For the given stratus case, the prognostic formulation gives much worse results than the reference (*Fig. 3c*).

The impact of turbulence parameterization has also been tested. It was supposed that Turbulent Kinetic Energy (TKE) is too high in the boundary layer and too strong mixing dissipates the fog in AROME. To test this assumption, the dissipation rate for TKE was increased. Surprisingly, this resulted in even less stratus (not shown). In a second experiment, the dissipation rate was decreased (from 0.85 to 0.2) which resulted in slightly more low level clouds in AROME (*Fig. 3d*). This model behavior is still under investigation.

It was assumed that one reason for the dissipation of stratus in AROME could be that after sunrise, more short wave radiation is transmitted through the fog layer in the model than in reality. Consequently, surface downward short wave radiation simulations were verified with the radiation measurement network of the Hungarian Meteorological Service, which consists of 39 stations. For the present case study, only four stations were selected in the eastern part of Hungary, where stratus was present the whole day both in reality and in ARPEGE, but not in AROME. Time series show that ARPEGE slightly overestimates the short wave radiation after sunrise, and the reference version of AROME simulates even higher values than ARPEGE. One of the main differences in the radiation settings of the two models is the value of the long wave inhomogeneity factor (*Nielsen et al., 2014*), which accounts for an increased radiation transfer in clouds. This parameter is set to 0.9 in ARPEGE and 0.7 in AROME. To test the impact of this parameter, both the short wave and long wave inhomogeneity factors were set to 1.0 in AROME. These settings result in a lower downward short wave radiation flux at the surface in AROME (*Fig. 4*). The increased optical thickness of clouds and the consequently slower heating of the boundary layer slightly increase the low level cloud cover over the eastern part of Hungary (*Fig. 3e*). In areas with frontal activity (north of Hungary), the modification has no impact on cloud cover.

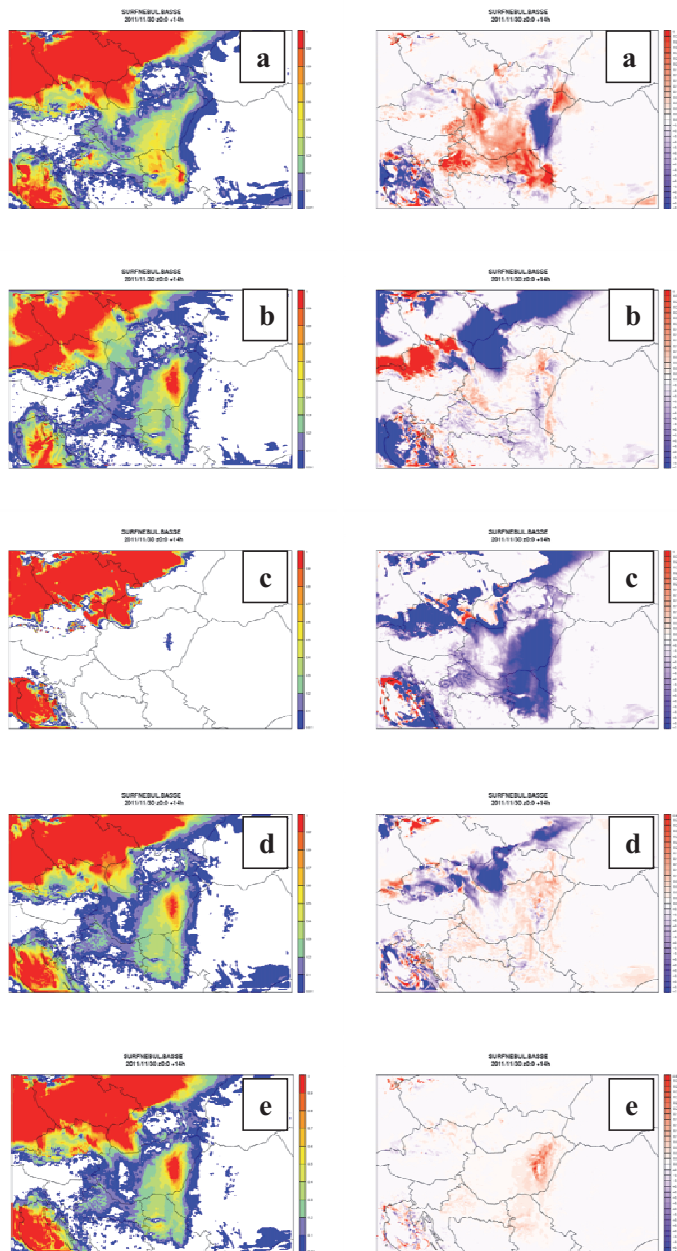


Fig. 3. Sensitivity experiments for AROME on November 30, 2011, at 14 UTC: (a) data assimilation, (b) lateral boundary conditions, (c) statistical cloud scheme, (d) turbulence parameterization, (e) cloud inhomogeneity factor in the radiation parameterization. Left column: low level cloud cover (white indicates no clouds, red indicates full cloud cover); right column: low level cloud cover difference (experiment-reference; red colors indicate more low level clouds in the experiment).

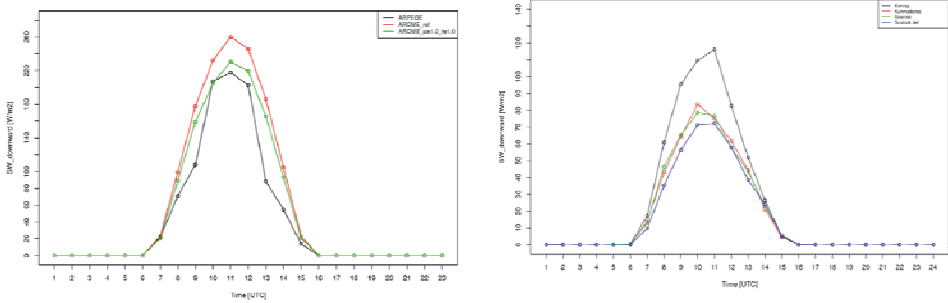


Fig. 4. Simulated (left) and observed (right) time series of downward short wave radiation on the surface on November 30, 2011. Model values are horizontally averaged on a $1^{\circ} \times 1^{\circ}$ box, which includes the ground measurements plotted on the right panel. Note the scale difference of the vertical axes between the two plots.

As shown in Fig. 4, even with the modification of the inhomogeneity factor, the simulated shortwave downward radiation of AROME is about three times as large as the measurements around noon (220 W/m^2 in AROME as compared to 70 W/m^2 in the measurements). To validate whether this overestimation is caused by the error in the radiation or in the microphysics scheme, the one-dimensional version of the AROME model (MUSC) was used. In this experiment, MUSC was initialized with the profiles and surface properties of the 3D AROME model and was also forced with tendencies obtained from the 3D AROME model. It was found that at 12 UTC, if the thickness of the cloud is enlarged by a factor of two (a value assumed to be close to reality) and the cloud liquid water content is increased from 0.1 g/kg to 0.3 g/kg (the latter is a typical value for continental stratus according to Hoffmann and Roth, 1989), then the simulated downward shortwave radiation is close to observations. Consequently, the radiation parameterization is most likely not responsible for the wrong low level cloud simulation of AROME.

Sensitivity tests on surface parameters were performed with MUSC in one dimension. AROME and ARPEGE 1D use the same initial vertical profiles. Only a few variables are changed in the initial surface file. Fig. 5 shows that this case is very sensitive to the vegetation fraction (VEG) and soil wetness index (SWI). With a bare (VEG=0) and moist (SWI=0.8) ground, AROME is not able to dissipate the cloud even if the cloud base and top are higher than in ARPEGE. In that case, moisture is easily taken from the first ground layer. With VEG=100% (a and c), it is more difficult to feed the atmosphere with moisture coming from the ground. Indeed, water has to be taken by the roots and is then provided to the atmosphere via plant evapotranspiration. Moreover, a too dry soil (SWI = 0) dissolves the fog during the afternoon, both in ARPEGE and AROME (c and d). Consequently, differences in soil moisture and/or vegetation fraction may partly explain differences observed between ARPEGE and AROME 3D runs.

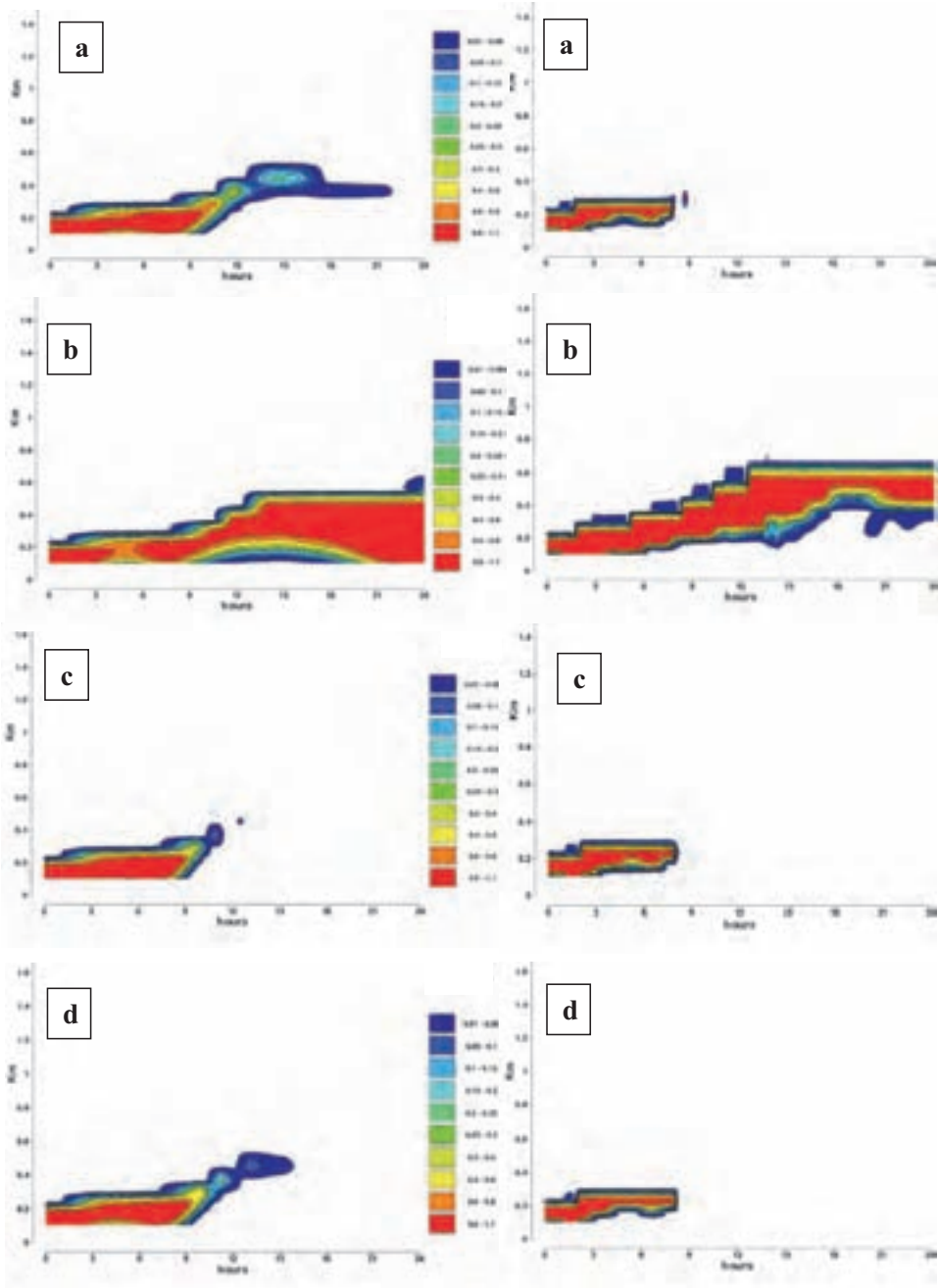


Fig. 5. One dimensional experiments: sensitivity tests on surface. Simulated cloudiness (white indicates no clouds, red indicates full cloud cover) time evolution in ARPEGE (left) and in AROME (right). (a) VEG=100% SWI=0.8, (b) VEG=0, SWI=0.8, (c) VEG=100% SWI=0, (d) VEG=0 SWI=0.

4. Tuning of microphysics

4.1. Case study

After the sensitivity experiments described above, the microphysics parameterization of AROME has also been investigated. After the subjective investigation of several other case studies (not shown), it was found that for wintertime stratus cases the AROME model often produces light precipitation. In the model, if temperature close to the surface is above 0 °C, the precipitation phase is liquid and the amount (typically around 0.3–0.5 mm/12h) is close to observations and other operational models (e.g., ECMWF/IFS, ARPEGE, WRF). Otherwise, for negative temperature the precipitation phase is solid and AROME gives higher values than the observations or other models (*Fig. 6a*).

This behavior is not due to dynamics or horizontal/vertical resolution differences, as it is not present in a forecast using ARPEGE physics but AROME dynamics on the AROME grid (*Fig. 6b*). It may come from differences in microphysics processes (Lopez scheme in ARPEGE (Lopez, 2002) with modifications of *Bouteloup et al.* (2005)), ICE3 in AROME (*Pinty and Jabouille, 1998*)).

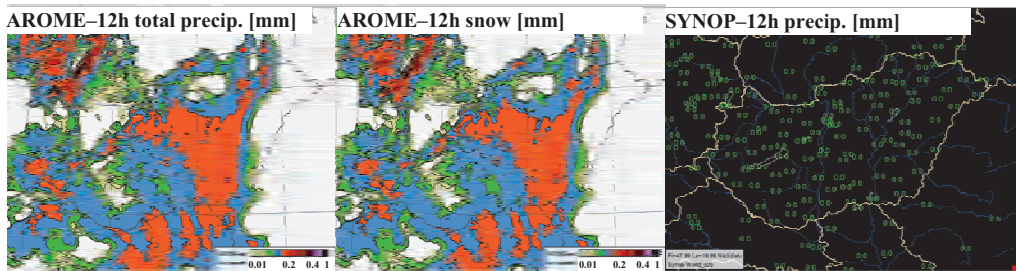


Fig. 6a. Accumulated 12h precipitation (in mm/12h) from AROME on November 30, 2011, at 12 UTC (+12h forecast) compared to synop observations. Left: total precipitation from AROME, middle: snow from AROME, right: synop observations.

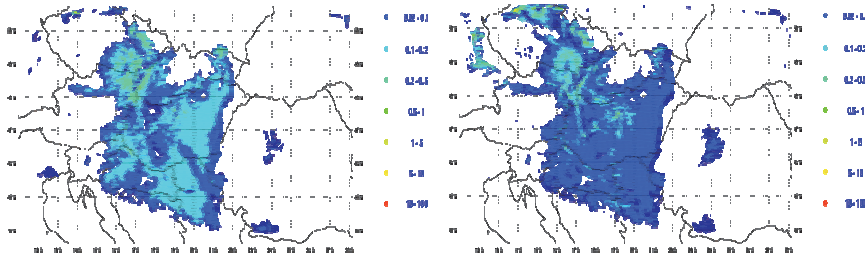


Fig. 6b. Accumulated 12h snowfalls on November 30, 2011, at 12 UTC (+12h forecast): left: ARPEGE physics at 2.5 km, right: AROME.

To understand the problem, budget profiles of microphysics were investigated from AROME (*Fig. 7*).

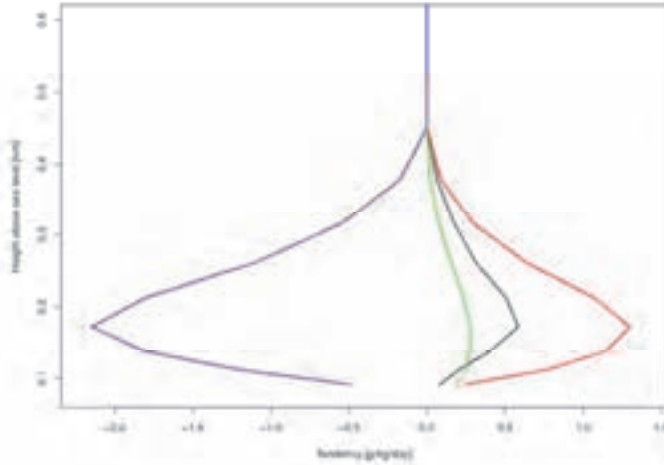


Fig. 7. Budget profiles for snow mixing ratio (in g/kg/day) from the AROME reference run between 00 and 06 UTC on November 30, 2011. The horizontal averaging was made on a 1 degree x 1 degree domain over the eastern part of Hungary. Main budget terms: sedimentation (blue), deposition on snow (red), autoconversion of ice to snow (black), riming by cloud droplets (green).

It was found that for the given case, three processes are responsible for the generation of falling snow: deposition, autoconversion of ice to snow and riming. The deposition process does not exist in ARPEGE Lopez scheme. That may explain differences shown in *Fig. 6b*. It was assumed that the largest uncertainty lies in the parameterization of autoconversion, so this process was selected for a tuning exercise. To reduce the solid precipitation in the model, the critical specific humidity value above which autoconversion could occur was increased from 0.02 g/m³ (as in (*Chaboureau et al.*, 2002) to 1 g/m³ (as in *Lin et al.*, 1983), keeping the temperature dependency of the critical value. Due to reduced solid precipitation, the low level cloud cover increases for the selected case (*Fig. 8*).

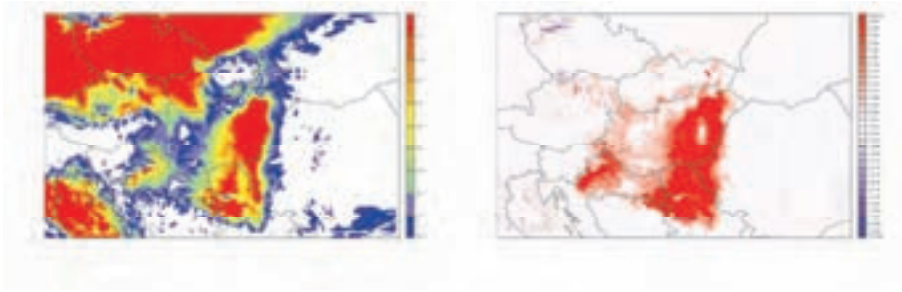


Fig. 8. Forecasted low level cloud cover by AROME with the modified autoconversion for November 30, 2011, at 14 UTC. Left: low level cloud cover, right: difference from the reference run.

4.2. Longer period with stratus

The proposed modification of the microphysics was tested on a two-week period in late autumn, 2011. This period was characterized by a frequent occurrence of daytime stratus due to a persistent anticyclone over Hungary. For every day of the period, a 24-hour forecast was run starting at 00 UTC. The configuration of this experimental chain was similar to the operational AROME-Hungary configuration in 2014, so an atmospheric 3DVAR data assimilation system was used with three hourly assimilation cycle. For the 3DVAR only conventional observations (synop stations, radiosoundings, and AMDAR data) were used. The initial condition of the soil was produced by interpolating the operational soil analysis of the ALADIN model (run at 8 km horizontal resolution). Three model configurations were compared: the reference run (“ref”) which has similar settings to the operational AROME-Hungary (diagnostic subgrid cloud scheme and original autoconversion); the first experiment (“exp1”) with modified autoconversion as described above (with diagnostic subgrid cloud scheme); and a second experiment (“exp2”) with prognostic subgrid cloud scheme and modified autoconversion. Significant differences were only detected in cloud cover and 2-meter temperature (*Fig. 9*). By comparing “ref” and “exp1” it can be noticed, that the modified autoconversion slightly increases cloud cover, thus decreases the model bias, and it also improves the temperature forecast. The comparison of “exp1” and “exp2” shows the impact of the saturation deficit variance parameterization. It is apparent that the prognostic subgrid cloud scheme gives much less clouds and also deteriorates the temperature forecast, especially during night for the selected time period.

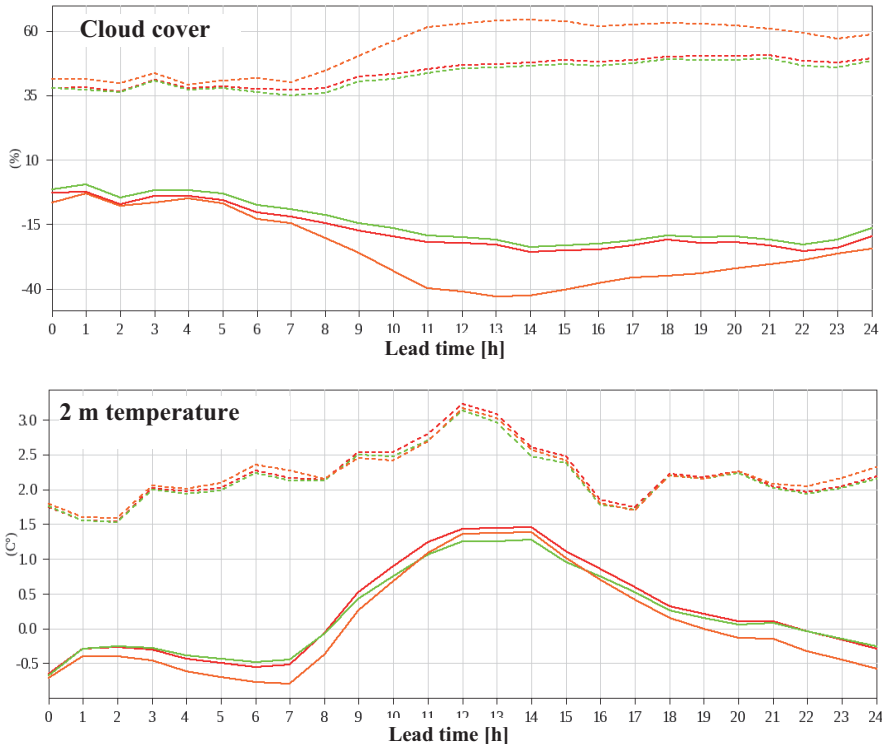


Fig. 9. Verification scores as a function of lead time for different AROME configurations for the period between November 18, 2011 and December 2, 2011. For the verification synop stations below 400 m were used over the AROME-Hungary domain. Upper panel: cloud cover, lower panel: 2-meter temperature. Solid lines: bias, dashed lines: RMSE. Red: reference run; green: first experiment (diagnostic subgrid cloud scheme, modified autoconversion); orange: second experiment (prognostic subgrid cloud scheme, modified autoconversion).

5. Control cases

The proposed modification of the microphysics parameterization has also been tested on so-called control cases. These cases should be characterized by different synoptic conditions than the one for which the modification have been developed. As the original case was a winter anticyclonic case, for the first control case a winter cyclonic situation with heavy snowfall was chosen, while for the second control case a summer convective event was selected.

On January 24, 2014, a Mediterranean cyclone was passing over Hungary causing heavy snowfall over the southwestern part of the country. According to

synop measurements, the depth of fallen snow exceeded 20 cm in large areas, and in mountainous regions values over 30 cm were also measured. Operational models (both hydrostatic and non-hydrostatic) forecasted the event successfully, however, the high values associated to orography were only present in the non-hydrostatic models (AROME and WRF). The run with the modified microphysics (“exp1”) simulated a snowfall pattern similar to the reference AROME run, with slightly lower values of snowfall (*Fig. 10*). No significant differences were detected for other variables, like temperature, cloud cover, or wind.

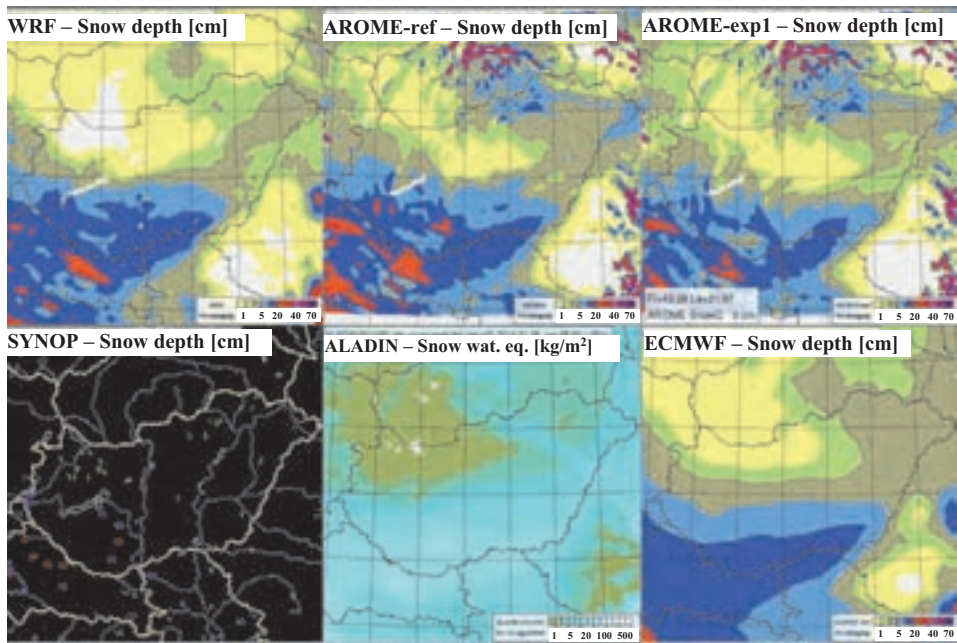


Fig. 10. Model forecasts and synop observations for the first control case. All models were initialized at 00 UTC on January 24, 2014, and +30h forecasts were made. Depicted is the 30h cumulated snowfall (except for the ALADIN model) both for models and synop measurements.

On June 24, 2013, a convective event occurred over Hungary. A cold front was approaching the region from northwest, and before the front in the warm sector thunderstorms developed which caused heavy precipitation (locally over 50 mm/24h). *Fig. 11* compares the precipitation forecasts of the reference AROME version and the one with modified microphysics.

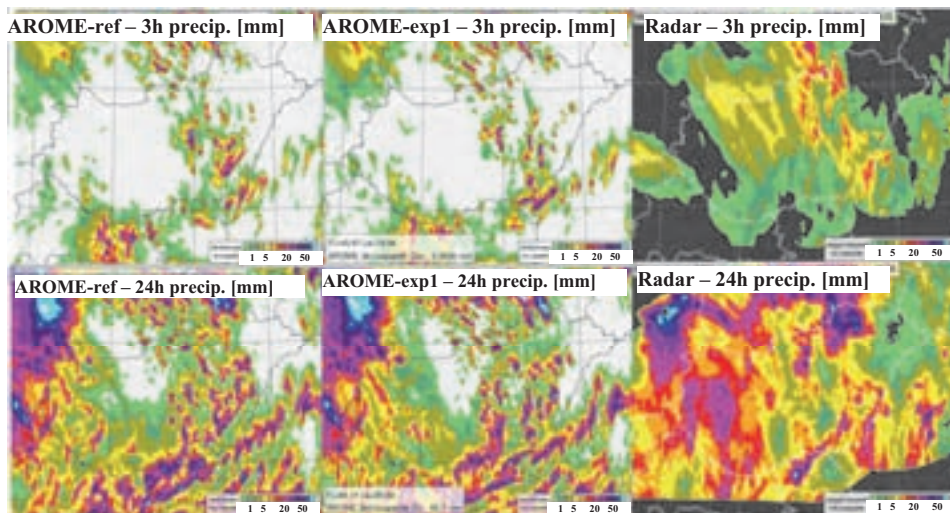


Fig. 11. Model forecasts and radar observations for the second control case. Both models were initialized at 00 UTC on June 24, 2013, and +24h forecasts were made. First row: 3h accumulated precipitation for the +18h lead time; second row: 24h accumulated precipitation for the +24h lead time.

Both versions were fairly successful in forecasting the thunderstorm activity over the eastern part of Hungary, however, over the western part, the precipitation amounts were underestimated by both versions. Regarding the timing of convection and the precipitation amounts, no significant difference was detected between the two versions of AROME.

6. Verification of longer periods

The proposed modification was also tested on longer continuous periods, which is a standard procedure to precede the operational implementation of a new model version. For this purpose, a winter (January 6-24, 2014) and a summer period (May 7-20, 2013) was selected. For these days, the AROME version with the proposed modification was run in an operational setting with a separate data assimilation cycle. These forecasts were then verified with observations, and verification scores were compared to the operational AROME model.

Model verification was performed either using standard surface (synop) observations with pointwise model-observation comparison (using the OVISYS system developed at the Hungarian Meteorological Service, *Randrimampianina*

et al., 2007), or using a novel spatial verification method (*Rezacova et al.*, 2015) based on the SAL (*Wernli et al.*, 2008) technique. The parameters investigated were temperature, humidity, precipitation, and clouds for the pointwise verification and precipitation for the spatial verification. It has to be noted that the spatial verification was only performed for the summer period. This is due to the fact, that the quantitative radar precipitation measurements used for the spatial scores are less reliable for winter situations with often very small precipitation intensities.

For the winter period, pointwise verification scores of the modified AROME version were very similar to the scores of the operational AROME for all meteorological parameters (not shown). This is mainly due to the fact, that the anticyclonic low level cloud cases were observed only on a small number of days in the period, and for other weather situations the impact of the modification is neutral.

For the summer period, pointwise verification showed no impact for cloudiness, temperature, and humidity. The pointwise precipitation verification showed small improvement for the morning hours of the forecast and neutral impact for the afternoon hours (*Fig. 12*). It has to be noted though, that the investigated period was rather short to be able to draw solid conclusions from pointwise verification in the case of a spatially strongly varying parameter like convective precipitation. Consequently, spatial verification scores were also investigated. *Fig. 13* shows the average intensity of precipitation objects as a function of forecast lead time for the reference and modified AROME versions and for radar observations. The precipitation objects were defined with the SAL method described in *Wernli et al.* (2008) using a dynamic threshold corresponding to 1/15 part of the maximum precipitation value over the domain. The three hourly accumulated radar precipitation measurements were corrected with surface synop measurements to account for the weakening of the Radar signal in the case of heavy precipitation. It can be concluded that the intensity of precipitation objects is overestimated by the AROME model in the late afternoon hours. The proposed microphysical modification improves model performance in this respect, however, a considerable overestimation still remains.

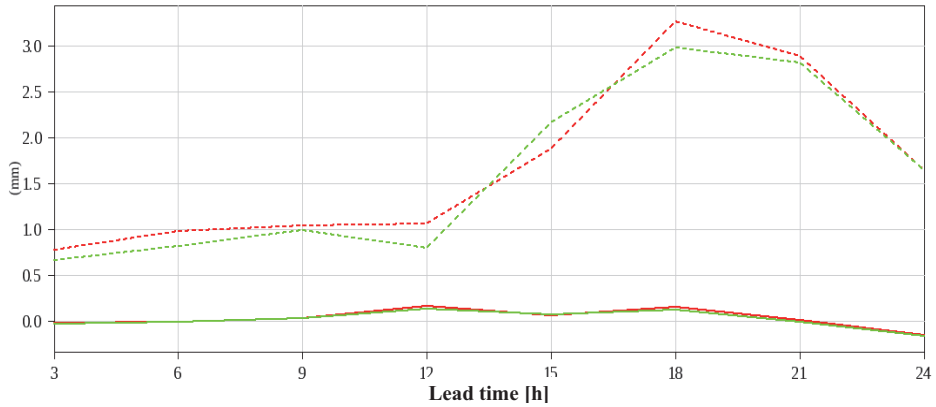


Fig. 12. Verification scores for 3h accumulated precipitation as a function of lead time for the period between May 5, 2013 and May 20, 2013. For the verification synop stations below 400 m were used over the AROME-Hungary domain. Solid lines: bias, dashed lines: RMSE. Red: reference run (original autoconversion); green: experiment (modified autoconversion).

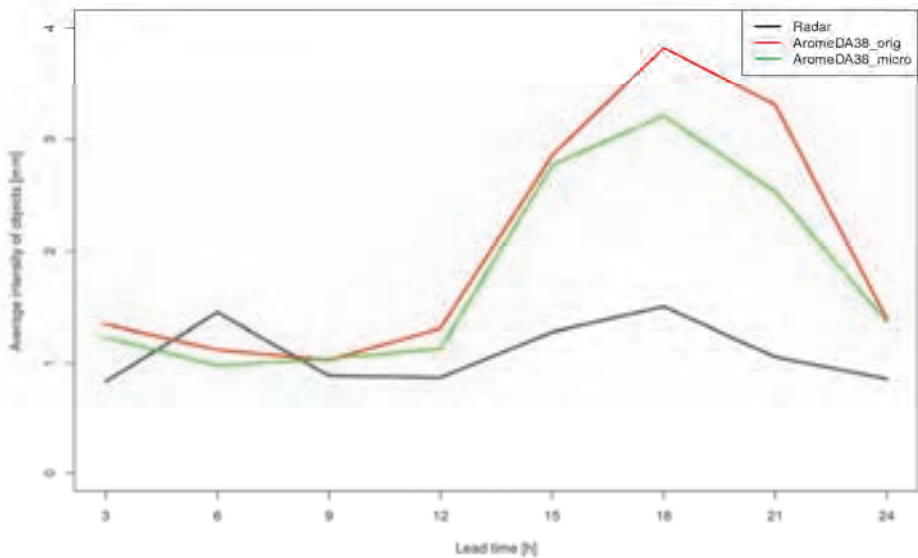


Fig. 13. Average intensity of precipitation objects as a function of lead time for different AROME configurations and radar observations for the period between May 5 and May 20, 2013. Black: radar; red: reference run (original autoconversion); green: experiment (modified autoconversion).

7. *Summary and conclusions*

In the present paper, wintertime low level cloud cases were investigated which are associated with anticyclonic conditions over Central Europe. Based on the experience of the forecasters at HMS, most operational numerical weather prediction models face difficulties when simulating these situations. The most common problem is the underestimation of low level cloud cover. Several sensitivity experiments were performed with the AROME model over Hungary, which investigated model performance in relation to initial and lateral boundary conditions, turbulence and radiation parameterization, surface properties, cloud and precipitation processes. Results indicated that the cause of the inadequate low level cloud forecast can be traced back to the microphysics parameterization. By increasing the critical threshold of cloud ice to snow autoconversion, the overestimation of light snow could be decreased, and consequently the low level cloud cover forecast improves.

After the detailed investigation of the selected wintertime anticyclonic case study, a longer period which mainly consisted of such situations was studied. Verification results proved that the proposed modification improves the simulation of clouds and consequently 2-meter temperature as well. As the next step, so-called “control cases” were investigated, with different weather situations (heavy snowfall and summer convection), showing neutral impact of the modification. Finally, two longer continuous periods in summer and winter were run with a separate data assimilation cycle. Pointwise and spatial verification results showed that the modification has a positive impact on the forecast of cloud cover and summertime convective precipitation. Impact on other meteorological parameters is neutral.

The investigations described above showed that the proposed microphysics modification could improve model performance, and it is worth to consider its implementation in the operational AROME version. Consequently, the modification was introduced as an option in the official code of AROME, and in April 2015, both the Hungarian Meteorological Service and Météo-France started to use it in its operational AROME configurations.

Acknowledgement: This study was conducted in the framework of the French — Hungarian bilateral project, entitled “Simulation of the Atmospheric Boundary Layer with the AROME Numerical Weather prediction model”, project numbers TÉT_11-2-2012-0003 (Hungary) and 27855UD (France).

References

Ahlgrimm, M., and R. Forbes, 2014: Improving the representation of low clouds and drizzle in the ECMWF model based on ARM observations from the Azores. *Mon. Weather Rev.* 142, 668–685. <https://doi.org/10.1175/MWR-D-13-00153.1>

- Benard, P., Vivoda, J., Masek, J., Smolikova P., Yessad, K., Smith, C., Brozkova, R., and Geleyn, J-F., 2010: Dynamical kernel of the Aladin-NH spectral limited-area model: Revised formulation and sensitivity experiments. *Quart. J. Roy. Meteor. Soc.* 136, 155–169. <https://doi.org/10.1002/qj.522>
- Bouteloup, Y., Bouyssel, F., and Marquet, P., 2005: Improvements of Lopez prognostic large scale cloud and precipitation scheme. ALADIN Newsletter, 28:66,73. 8
- Boutle, I., Price, J., Kudzotsa, I., Kokkola, H., and Romakkaniemi, S., 2018: Aerosol-fog interaction and the transition to well-mixed radiation fog, *Atmos. Chem. Phys.*, 7827-7840. <https://doi.org/10.5194/acp-18-7827-2018>
- Bubnová, R., Hello, G., Bénard, P., and Geleyn, J.-F., 1995: Integration of the fully elastic equations cast in the hydrostatic pressure terrain-following in the framework of the ARPEGE/ALADIN NWP system. *Mon. Weather Rev.* 123, 515–535. [https://doi.org/10.1175/1520-0493\(1995\)123<0515:IOTFEE>2.0.CO;2](https://doi.org/10.1175/1520-0493(1995)123<0515:IOTFEE>2.0.CO;2)
- Chaboureau, J.-P. and Bechtold, P., 2002: A simple cloud parameterization derived from cloud resolving model data: Diagnostic and prognostic applications. *J. Atmos. Sci.* 59, 2362–2372. [https://doi.org/10.1175/1520-0469\(2002\)059<2362:ASCPDF>2.0.CO;2](https://doi.org/10.1175/1520-0469(2002)059<2362:ASCPDF>2.0.CO;2)
- Chaboureau, J.-P., Cammas, J.-P., Mascart, P. J., Pinty, J.-P., and Lafore J.-P., 2002: Mesoscale model cloud scheme assessment using satellite observations. *J. Geophys. Res.* 107(D16), 4301. <https://doi.org/10.1029/2001JD000714>
- Courtier, P., Freydier C, Geleyn JF, Rabier F, and Rochas M., 1991: The ARPEGE project at Météo-France. In: Proc. ECMWF Seminar on Numerical Methods on Atmospheric Models. Vol. 2, Shinfield Park, Reading, UK, ECMWF, 193–231.
- Fischer, C., Montmerle, T., Berre, L., Auger, L., and Stefanescu, S. E., 2005: An overview of the variational assimilation in the Aladin/FranceNWP system. *Quart. J. Roy. Meteor. Soc.* 131, 3477–3492. <https://doi.org/10.1256/qj.05.115>
- Forbes, R.M. and M. Ahlgrimm, 2014: On the representation of high-latitude boundary layer mixed-phase cloud in the ECMWF global model. *Mon. Weather Rev.* 142, 3425–3445. <https://doi.org/10.1175/MWR-D-13-00325.1>
- Haeffelin, M., Bergot, T., Elias, T., Tardif, R., Carrer, D., Chazette P., Colomb, M., Drobinski, P., Dupont, E., Dupont, J., Gomes, L., Musson-Genon, L., Pietras, C., Plana-Fattori, A., Protat, A., Rangognio, J., Raut, J., Rémy, S., Richard, D., Sciare, J., and Zhang, X., 2010: PARISFOG: shedding new light on fog physical processes. *Bull. Amer. Meteorol. Soc.* 91, 767–783. <https://doi.org/10.1175/2009BAMS2671.1>
- Hoffmann, H.-E. and Roth, R., 1989: Cloudphysical Parameters in Dependence on Height Above Cloud Base in Different Clouds. *Meteorol. Atmos. Phys.* 41, 247–254. <https://doi.org/10.1007/BF01026113>
- Lafore, J.-P., Lafore, J. P., Stein, J., Asencio, N., Bougeault, P., Ducrocq, V., Duron, J., Fischer, C., Hérelil, P., Mascart, P., Masson, V., Pinty, J. P., Redelsperger, J. L., Richard, E., and Vilà-Guerau de Arellano J., 1998: The Meso-NH atmospheric simulation system. Part I: Adiabatic formulation and control simulations. *Ann. Geophys.* 16, 90–109. <https://doi.org/10.1007/s00585-997-0090-6>
- Lin, Y.-L., Farley, R.D., and Orville, H.D., 1983: Bulk parameterization of snow field in a cloud model. *J. Climate Appl. Meteor.* 22, 1065–1092.
- Lopez, Ph., 2002: Implementation and validation of a new prognostic large-scale cloud and precipitation scheme for climate and data-assimilation purposes. *Quart. J. Roy. Meteor. Soc.*, 128, 229-257. <https://doi.org/10.1256/00359000260498879>
- Masson, V., P. Le Moigne, E. Martin, S. Faroux, A. Alias, R. Alkama, S. Belamari, A. Barbu, A. Boone, F. Bouyssel, P. Brousseau, E. Brun, J.-C. Calvet, D. Carrer, B. Decharme, C. Delire, S. Donier, K. Essaouini, A.-L. Gibelin, H. Giordani, F. Habets, M. Jidane, G. Kerdraon, E. Kourzeneva, M. Lafaysse, S. Lafont, C. Lebeaupin Brossier, A. Lemonsu, J.-F. Mahfouf, P. Marguinaud, M. Mokhtari, S. Morin, G. Pigeon, R. Salgado, Y. Seity, F. Taillefer, G. Tanguy, P. Tulet, B. Vincendon, V. Vionnet, and A. Voldoire, 2013: The SURFEXv7.2 land and ocean surface platform for coupled or offline simulation of earth surface variables and fluxes. *Geosci. Model Dev.* 6, 929-960. <https://doi.org/10.5194/gmd-6-929-2013>

- Mazoyer, M., Lac, C., Thouron, O., Bergot, T., Masson, V., and Musson-Genon, L., 2017: Large eddy simulation of radiation fog: impact of dynamics on the fog life cycle, *Atmos. Chem. Phys.*, 17, 13017–13035. <https://doi.org/10.5194/acp-17-13017-2017>
- Mile M., Bölöni, G., Randriamampianina, R., Steib, R., and Kucukkaraca, E., 2015: Overview of mesoscale data assimilation developments at the Hungarian Meteorological Service. *Időjárás* 119, 215–241.
- Nielsen K.P., Gleeson E., and Rontu, L., 2014: Radiation sensitivity tests of the HARMONIE 37h1 NWP model. *Geosci. Model Dev.* 7, 1433–1449. <https://doi.org/10.5194/gmd-7-1433-2014>
- Philip A., Bergot, T., Bouteloup, Y. and Bouyssel, F., 2016: The Impact of Vertical Resolution on Fog Forecasting in the Kilometric Scale Model Arome: A case Study and Statistics. *Weather Forecast.* 31,1655–1671. <https://doi.org/10.1175/WAF-D-16-0074.1>
- Pinty, J.-P. and P. Jabouille, 1998: A mixed-phased cloud parameterization for use in a mesoscale non-hydrostatic model: simulations of a squall line and of orographic precipitation. Conf. on Cloud Physics, Everett, WA, Amer. Meteor. Soc., Preprints, 217–220.
- Price, J., Lane, S., Boutle, I., Smith, D., Bergot, T., Lac, Duconge, L., C., McGregor, J., Kerr-Munslow, A., Pickering, M., and Clark, R., 2018: LANFEX: a field and modelling study to improve our understanding and forecasting of fog, *Bull. Amer. Meteor. Soc.*, . <https://doi.org/10.1175/BAMS-D-16-0299.1>
- Randriamampianina, R., Balogh, M., Bölöni, G., Csima, G., Hágel, E., Horányi, A., Ihász, I., Kertész, S., Kullmann, L., Lőrincz, A., Radnóti, G., Szabó, L., Szépszó, G., Szintai, B., Tóth, H., and Vörös, M., 2007: Recent development and changes in the operational ALADIN/HU 3D-Var system Poster presented at SRNWP Workshop on Data Assimilation, Emphasis: Use of moisture-related observations, Norrköping, Sweden, 21-23 March, 2007.
- Řezáčová, D, Szintai, B , Jakubiak, B., Yano, J-I, and Turner, S, 2015: Verification of high-resolution precipitation forecast with radar-based data. In: Robert, S Plant; Jun-Ichi, Yano (ed.) Moist Atmospheric Convection: An Introduction and Overview : Parameterization of Atmospheric Convection. Volume 1: Theoretical Background and Formulation. Imperial College Press, 173–214.
- Seity, Y., Brousseau, P., Malardel, S., Hello, G., Bénard, P., Bouttier, F., Lac, C., and Masson, V., 2011: The AROME-France Convective-Scale Operational Model. *Mon. Weather Rev.* 139, 976–991. <https://doi.org/10.1175/2010MWR3425.1>
- Sommeria, G. and J.W. Deardorff, 1977, Subgrid scale condensation in models for non precipitating clouds. *J. Atmos., Sci.* 34, 344–355. [https://doi.org/10.1175/1520-0469\(1977\)034<0344:SSCIMO>2.0.CO;2](https://doi.org/10.1175/1520-0469(1977)034<0344:SSCIMO>2.0.CO;2)
- Szintai B., Szűcs, M., Randriamampianina, R., and Kullmann, L., 2015: Application of the AROME non-hydrostatic model at the Hungarian Meteorological Service: physical parametrizations and ensemble forecasting. *Időjárás* 119, 241–265.
- Termonia P., C. Fischer, E. Bazile, F. Bouyssel, R. Brožková, P. Bénard, B. Bochenek, D. Degrauwe, M. Derková, R. El Khatib, R. Hamdi, J. Mašek, P. Pottier, N. Pristov, Y. Seity, P. Smolíková, O. Španiel, M. Tudor, Y. Wang, C. Wittmann, and A. Joly, 2018: The ALADIN System and its canonical model configurations AROME CY41T1 and ALARO CY40T1. *Geosci. Model Dev.* 11, 257–281. <https://doi.org/10.5194/gmd-11-257-2018>
- Wernli, H., Paulat, M., Hagen, M. and Frei, Ch., 2008: SAL - A novel quality measure for the verification of Quantitative Precipitation Forecast. *Mon. Weather Rev.* 136, 4470–4487. <https://doi.org/10.1175/2008MWR2415.1>

IDŐJÁRÁS

Quarterly Journal of the Hungarian Meteorological Service
Vol. 123, No. 2, April – June, 2019, pp. 203–215

Online coupled modeling of weather and air quality of Budapest using the WRF-Chem model

Attila Kovács¹, Ádám Leelőssy¹, Róbert Mészáros^{1,*}, and István Lagzi^{2,3}

¹ *Eötvös Loránd University, Department of Meteorology
Pázmány Péter sétány 1/A, 1117 Budapest, Hungary*

² *Budapest University of Technology and Economics
Department of Physics
Budafoki út 8, 1111 Budapest, Hungary*

³ *MTA-BME Condensed Matter Research Group
Budafoki út 8, 1111 Budapest, Hungary*

**Corresponding author E-mail: mrobi@nimbus.elte.hu*

(Manuscript received in final form October 18, 2018)

Abstract—WRF-Chem is a numerical Eulerian non-hydrostatic mesoscale weather prediction model online coupled with the atmospheric chemistry model, developed mainly by the National Center for Atmospheric Research (NCAR) and the National Oceanic and Atmospheric Administration (NOAA). This model system is a frequently used tool for creating high resolution air quality simulations at different spatial and temporal scales for various air pollutants. In this study, the technical backgrounds of the WRF-Chem model applied for high resolution urban air quality forecasts in Budapest are presented. The meteorological module of the system uses the WRF-ARW (Weather Research and Forecasting – Advanced Research WRF) dynamical solver, and obtains its initial and boundary conditions from the GFS (Global Forecast System) using a horizontal resolution of 0.25×0.25 degree. By applying two nested model domains (with 15×5 km horizontal resolution), fine resolution meteorological fields can be achieved. In the chemical module, the National Emission Inventories created by the Hungarian Meteorological Service were applied, different chemical reaction sets were used and tested, and constant deposition rates were assumed. In this work, a case study for different pollutants (O_3 , NO, NO_2 , and CO) is presented for an early summer period of 2015.

Key-words: WRF-Chem, air pollution, photochemical mechanism, tropospheric ozone

1. Introduction

Outdoor air pollution is a serious environmental issue in Hungary, especially in winters. Ambient air quality thresholds for NO₂ and PM₁₀ are regularly exceeded (Mészáros *et al.*, 2013). The Aphekom project found that in the period of 2008–2011, the life expectancy was decreased by 19 months in Budapest due to the outdoor air pollution (Pascal *et al.*, 2013). The World Health Organization (WHO) found that in 2012, approximately 8,000 premature deaths could be attributed to polluted ambient air in Hungary (WHO, 2016). The main sources of PM₁₀ and ozone air pollution are domestic heating, road traffic, and large-scale transport of air pollutants (Ferenczi, 2013; Kis-Kovács *et al.*, 2017). The European Union expects effective strategies to diminish the effect of air pollution, however, policymaking requires the good understanding of the fine scale urban environmental processes and the reliable prediction of air quality for the following days. Operational air quality prediction is performed by the Hungarian Meteorological Service using the CHIMERE air dispersion model offline coupled with the WRF numerical weather prediction model (Ferenczi *et al.*, 2014).

Online coupled weather and air quality modeling have become a powerful and widely applied tool to predict and evaluate air pollution on the regional scale (Baklanov *et al.*, 2014). In Europe, numerical air quality forecasts are available from several continental scale atmospheric chemistry transport models, mainly those of the Copernicus Atmospheric Monitoring Service (CAMS) cooperation (<https://atmosphere.copernicus.eu/>). Its models use a grid of 0.1 degree resolution on the continental scale to operationally predict atmospheric concentrations of the main air pollutants, as well as pollens and volcanic ash (Marécal *et al.*, 2015). However, for cities and other sensitive areas, a finer model resolution might be necessary, especially if the emission inventory is available on a fine scale. This can be achieved by a nested atmospheric chemistry transport model that can reach very fine (1–3 km) resolution for a limited area (Kuik *et al.*, 2016; Liu *et al.*, 2018).

WRF-Chem is an atmospheric chemistry and transport module online integrated with the extremely popular Weather Research and Forecast (WRF) numerical weather prediction model. It solves the governing equations of atmospheric dynamics, tracer transport, and chemical reactions within one model system, sharing the same grid and timesteps (Grell *et al.*, 2005). Online coupling enables the model to simulate the feedbacks of air pollution on the weather, especially the effects of atmospheric aerosols (Kong *et al.*, 2015). On the other hand, online coupling of the meteorology and transport simulation can gain better accuracy in complex weather situations by accessing the full planetary boundary layer (PBL) parameterization of the weather forecast model and avoiding the information bottleneck of derived output parameters (Baklanov *et al.*, 2014; Leelőssy *et al.*, 2017).

WRF-Chem has been used in several countries for regional and urban scale air pollution forecast. In recent years, nested WRF-Chem simulations focusing on urban air pollution have been presented for cities such as Berlin (*Kuik et al.*, 2016), Madrid (*José et al.*, 2015), Los Angeles (*Kim S.-W. et al.*, 2016), for several metropolitan regions in China (*Liao et al.*, 2015; *Zhang et al.*, 2015; *Liu et al.*, 2018), and even for the complex terrain of Kathmandu (*Mues et al.*, 2017). However, comparison studies proved that WRF-Chem model results show a large sensitivity on the selection of the chemistry scheme, both regarding the tropospheric ozone (*Mar et al.*, 2016) and secondary aerosol (*Balzarini et al.*, 2015) formation. For example, in a photochemical box model, 25% difference was found between NO_x concentrations obtained with different chemical mechanisms (*Knote et al.*, 2015).

In this paper, we investigate the applicability of WRF-Chem (numerical weather prediction and atmospheric chemistry and transport) model to simulate and estimate concentration levels and diurnal variation of ozone and nitrogen oxides in Budapest and other sites in Hungary.

2. Methods

The WRF-Chem coupled meteorology-chemistry model was applied for air pollutant transport simulation using two nested domains (*Fig. 1*). The external domain covered Central Europe ranging $1,500 \times 1,050$ km with horizontal resolution of 15 km. The internal, 5-km-resolution domain had a size of 560×350 km, covering Hungary entirely. The number of horizontal grid points was therefore 7,000 and 7,840 in the external and internal domain, respectively. The same 40 vertical levels between 1,000 and 50 hPa were applied in both domains. Lateral boundary conditions were provided by the GFS (Global Forecast System) global model with a horizontal and temporal resolution of 0.25° and 3 hours, respectively. Lower boundary conditions are obtained from static geographical input data by the WRF Preprocessing System (WPS). The applied parameterization schemes are presented in *Table 1*.

Pollutant emissions were obtained from the 2015 National Emission Ceiling Directive – Informative Inventory Report of the Hungarian Meteorological Service (*Kis-Kovács et al.*, 2017). NECD-IIR provided estimates of the total annual release of 15 air pollutants on a horizontal grid covering Hungary with a resolution of $0.1^\circ \times 0.1^\circ$. In this study, the emission inventories of NO_x, NMVOCs (non-methane volatile organic compounds) and CO were used. NMVOC emission was added to the model input as isoprene emission.

Table 1. The configuration of the WRF-Chem model runs

Physical/chemical process	Applied scheme
Planetary boundary layer	Mellor–Yamada–Janjic scheme
Microphysics	WRF Single-Moment 6-class scheme
Photolysis	Fast-J photolysis
Gas-phase chemistry	Regional Acid Deposition Model 2
Longwave radiation	Rapid Radiative Transfer Model
Shortwave radiation	Old Goddard scheme
Cumulus convection	Grell-Freitas ensemble scheme
Urban canopy	Building Environment Parameterization
Land surface process	Noah Land Surface Model
Surface layer scheme	Monin-Obukhov Janjic Eta similarity scheme

The annual emission value was uniformly distributed in the year, therefore, the temporal variability of the emissions could not be considered in this model. However, due to the fine spatial resolution of both the emission inventory and the computational domain, the differences in urban and rural air pollution could be well investigated.

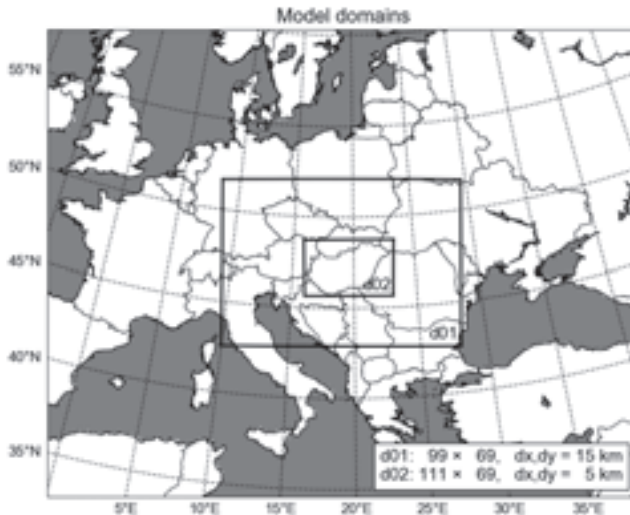


Fig. 1. The two nested computational domains of the WRF-Chem simulations.

A period of four days was simulated with the WRF-Chem model. The first day (May 15, 2015) was a spin-up period for the meteorological component, and only the meteorological calculations were performed by the model. The second day (May 16, 2015) was used as a spin-up phase for the chemistry model and was then discarded. The third and fourth days (May 17 and 18, 2015) were considered as the model results.

A summer period with calm anticyclonic weather was selected for the investigation of the photochemical ozone production from 2015, the reference year of the IIR emission inventory. The spin-up day for meteorology has been used to create the atmospheric initial conditions for the WRF domains corresponding to the GFS boundary conditions, as no data assimilation was performed. Initial and lateral boundary conditions for chemistry have been set to zero, and the chemistry spin-up period was used to create the initial concentration field corresponding to the emission inventory. By choosing a period with calm weather and weak winds, the effect of local emissions could be investigated.

Model results were compared to measurement data from the following automatic monitoring stations of the Hungarian Air Quality Network: Budapest (Gillice tér station in the south-eastern suburbs of the city), Pécs, Győr, Debrecen, and K-Pusztá (field monitoring station) (*Fig. 2*).

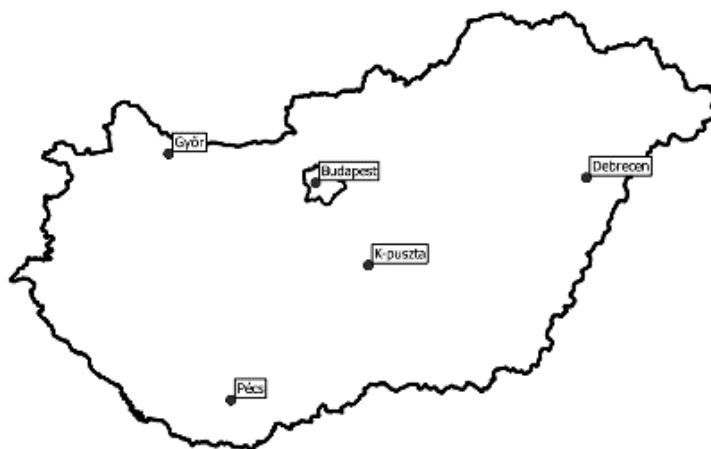


Fig. 2. Air quality monitoring sites of the Hungarian Air Quality Network where the model comparison was performed.

Two chemical mechanisms have been compared: the RADM2 (*Regional Acid Deposition Model 2nd generation*) and the CBMZ (*Carbon-Bond Mechanism version Z*), both with and without a KPP (*Kinetic PreProcessor*) solver (Stockwell *et al.*, 1990; Zaveri and Peters, 1999). RADM2 mechanism contains 21 and 42 inorganic and organic chemical species, respectively, with 158 chemical reactions out of them 21 are photochemical reactions (Gross and Stockwell, 2003). CBMZ is a modified and updated version of the CBM-IV mechanism (Gery *et al.*, 1989), which contains 52 chemical species with 132 chemical reactions (Zaveri and Peters, 1999).

3. Results

Despite the stationary emission rates of CO, NO, and NO₂, the simulated O₃ concentration data were consistent with the typical diurnal cycle of ozone and the measurement data provided by the monitoring stations (Fig. 3). The highest concentrations of ozone were observed in the afternoon, especially between 15–18 UTC, reaching 100 µg/m³. (The solar time in Budapest was UTC + 80 minutes on these days.) The diurnal cycle was well captured by all chemical mechanisms. A general underestimation can be observed in the results obtained with the CBMZ mechanism, while RADM2 was found to provide generally higher ozone concentrations. This is surprising in the context of a year-long European-scale study, where RADM2 showed a significant negative bias (Mar *et al.*, 2016). Ozone rapidly decayed in the model during the night in both CBMZ and the RADM2-KPP runs. However, the RADM2 mechanism without KPP resulted in a relatively high (20–50 µg/m³) residual night-time ozone concentration near the surface. Apart from this effect, there was generally a very small difference between results obtained with and without the kinetic pre-processor.

The modeled diurnal cycle of the NO concentration was close to the observed one, but lacked the night peak from 18 UTC to 00 UTC. The RADM2 and RADM2-KPP mechanisms overestimated the peak NO₂ levels by a factor of 2, unlike the CBMZ and CBMZ-KPP mechanisms, which gave a much better correspondence with the observed concentrations. The simulations provided almost the same CO concentration levels with all chemical settings. The temporal evolution of CO concentrations was well reproduced, however, the models yielded significantly lower values than the measurement data. It must be noted that due to the high uncertainty of the emission inventory and the limited representativity of urban monitoring sites, the model errors can hardly be attributed quantitatively to the applied chemical mechanisms.

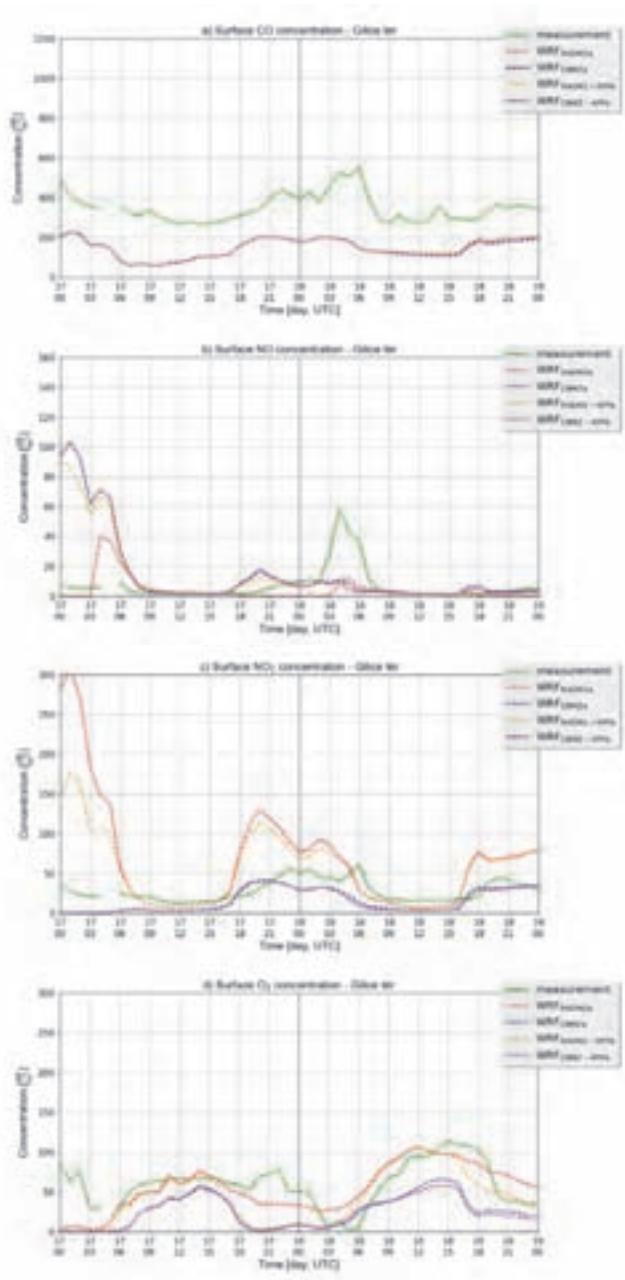


Fig. 3. Measured and modeled concentration of air pollutants on May 17–18, 2015 in Budapest, Gilice tér. Dashed lines: time series of simulated near-surface concentrations of a) CO, b) NO, c) NO₂, and d) O₃, respectively. Green line: time series of hourly measured concentrations. (Source of measured data: Hungarian Air Quality Network – <http://www.levegominoseg.hu/>).

As the NECD-IIR database provided the total NO_x emission data for nitrogen oxides, the sensitivity of the chemical mechanism was investigated for the initial NO/NO_x ratio. For the first set of simulations (a) the NO/NO_x proportion in the initial NO_x emission data was set to the simplistic 0.50 ratio, to 0.75 for the second sequence (b), and to 0.25 for the final series (c).

Fig. 4 shows the simulated O_3 concentrations using the RADM2-KPP and CBMZ-KPP chemical mechanisms, each with applying the three $\text{NO}-\text{NO}_2$ scenarios. Only two of four mechanisms are shown, because there was no considerable difference between the CBMZ and the CBMZ-KPP mechanism in the O_3 concentrations, and the alteration of the $\text{NO}-\text{NO}_2$ distribution in the NO_x emission did not affect the model output concentrations in the case of the RADM2 chemical mechanism. The sensitivity of O_3 concentration on the initial NO/NO_x ratio was very low during the day, however, the decreased direct NO emission in the (c) scenario caused higher night-time ozone levels due to the weakening of the $\text{NO}-\text{O}_3$ reaction.

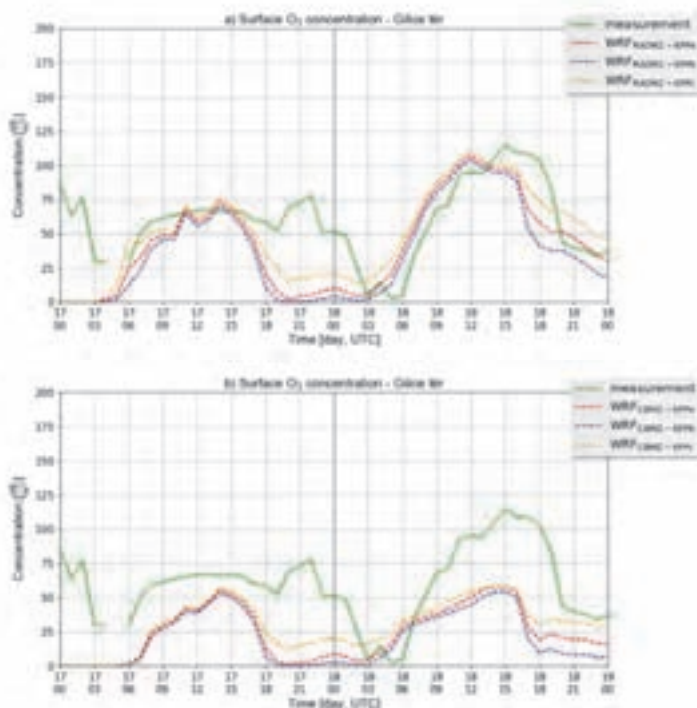


Fig. 4. Measured and modeled concentration of air pollutants on May 17–18, 2015 in Budapest, Gilice tér using the RADM2 (a) and CBMZ (b) chemical model. Dashed lines: time series of simulated near-surface concentrations of O_3 using different NO/NO_2 emission ratios, $\text{NO}/\text{NO}_x = 0.5$ (red dashed line), $\text{NO}/\text{NO}_x = 0.75$ (blue dashed line), and $\text{NO}/\text{NO}_x = 0.25$ (yellow dashed line). Solid green line: time series of measured concentrations. (Source of measurement data: Hungarian Air Quality Network - <http://www.levegominoseg.hu/>).

Fig. 5 shows the simulated concentration field of O₃ at 12 UTC, May 18, 2015 using the RADM2-KPP chemical mechanism. The 10 m wind field is also presented by wind barbs. A large plume indicates Budapest, the capital and biggest city of Hungary in the north central part of the country. This plume of ozone was formed by the significant urban emissions of NO_x and was transported north-westward by light near-surface winds. (*Fig. 5*).

A comparison of measured and modeled ozone concentrations at selected monitoring sites are presented in *Fig. 6*. Pécs, Győr, and Debrecen are urban sites, while K-Pusztza is a background site located in an agricultural area. The diurnal cycle of ozone was generally well captured by the model, and the RADM2 mechanism yielded higher – more realistic – ozone concentrations, while results obtained with the CBMZ scheme showed a serious underestimation. The best agreement of model results with observations was found at the background station K-Pusztza that had the largest spatial representativity (*Fig. 6*). At the urban sites of Győr, Pécs, and Debrecen, a secondary night-time ozone peak was observed, which could not be captured by the model.

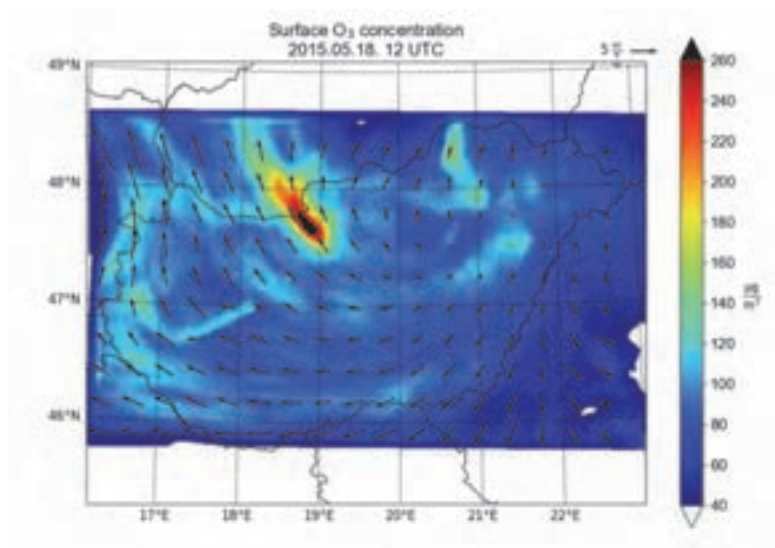


Fig. 5. Simulated near-surface ozone concentration and 10 m wind field at 12 UTC, May 18, 2015, using WRF-Chem with the RADM2-KPP chemical mechanism.

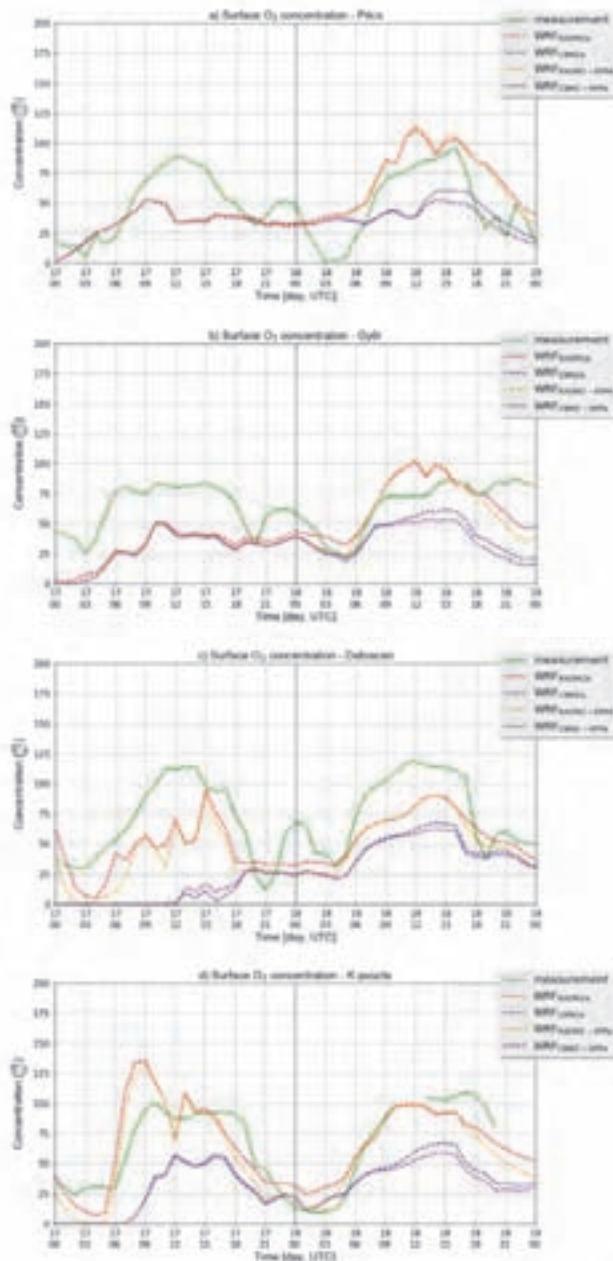


Fig. 6. Measured and modeled concentration of air pollutants on May 17–18, 2015 in a) Pécs, b) Győr, c) Debrecen, and d) Kaposvár. Dashed lines: time series of simulated near-surface concentrations of O₃ on May 17–18, 2015 at 4 locations within Hungary using different chemical mechanisms. Green line: time series of measured O₃ concentration at the respective monitoring sites. (Source of measurement data: Hungarian Air Quality Network - <http://www.levegominoseg.hu/>).

4. Conclusion

An online coupled atmospheric chemistry transport modeling application has been presented to simulate the air pollution of Hungary. Simulations were performed with the WRF-Chem model using two nested domains covering Central Europe and Hungary. With this method, a relatively low horizontal resolution (5 km) could be achieved at an acceptable computational cost. Provided with meteorological boundary conditions from the Global Forecast System (GFS) and emission data from the NERC–IIR national emission inventory, the model could simulate the atmospheric dispersion of pollutants and the photochemical ozone formation.

Model capabilities were demonstrated through a case study for May 17–18, 2015, comparing two chemical mechanisms (RADM2 and CBMZ), both with and without the kinetic pre-processor (KPP). Emission inventories of NO_x, non-methane VOCs, and CO were considered. Model results were compared to measurements taken at monitoring sites of the Hungarian Air Quality Network (OLM). The diurnal cycle of ozone was generally well captured by the model despite the stationary emission field. However, a large difference was found between the two applied chemical mechanisms. RADM2 provided generally higher and more realistic ozone concentrations, however, it seriously overestimated NO₂ levels. Results showed low sensitivity on the application of the kinetic pre-processor and the initial NO/NO₂ ratio.

Acknowledgement: This work was supported by the National Research, Development and Innovation Office of Hungary (No. K116506, K128805-K128818).

References

- Baklanov, A., Schlünzen, K., Suppan, P., Baldasano, J., Brunner, D., Aksoyoglu, S., Carmichael, G., Douros, J., Flemming, J., Forkel, R., Galmarini, S., Gauss, M., Grell, G., Hirtl, M., Joffre, S., Jorba, O., Kaas, E., Kaasik, M., Kallos, G., Kong, X., Korsholm, U., Kurganskiy, A., Kushta, J., Lohmann, U., Mahura, A., Manders-Groot, A., Maurizi, A., Moussiopoulos, N., Rao, S.T., Savage, N., Seigneur, C., Sokhi, R.S., Solazzo, E., Solomos, S., Sørensen, B., Tsegas, G., Vignati, E., Vogel, B., and Zhang, Y., 2014: Online coupled regional meteorology chemistry models in Europe: current status and prospects. *Atmos. Chem. Physics* 14, 317–398.
<https://doi.org/10.5194/acp-14-317-2014>
- Balzarini, A., Pirovano, G., Honzak, L., Žabkar, R., Curci, G., Forkel, R., Hirtl, M., San José, R., Tuccella, P., and Grell, G.A., 2015: WRF-Chem model sensitivity to chemical mechanisms choice in reconstructing aerosol optical properties. *Atmos. Environ.* 115, 604–619.
<https://doi.org/10.1016/j.atmosenv.2014.12.033>
- Ferenczi, Z., 2013: Predictability analysis of the PM_{2.5} and PM₁₀ concentration in Budapest. *Időjárás* 117, 359–375.
- Ferenczi, Z., Labancz, K., and Steib, R., 2014: Development of a Numerical Prediction Model System for the Assessment of the Air Quality in Budapest, In (eds. Steyn, D. and Mathur, R.) Air Pollution Modeling and Its Application. XXIII, Springer Proceedings in Complexity, Springer International Publishing, 401–405.

- Gery, M.W., Whitten, G.Z., Killus, J.P., and Dodge, M.C., 1989: A photochemical kinetics mechanism for urban and regional scale computer modeling. *J. Geophys. Res. Atmospheres* 94, 12925–12956. <https://doi.org/10.1029/JD094iD10p12925>
- Grell, G.A., Peckham, S.E., Schmitz, R., McKeen, S.A., Frost, G., Skamarock, W.C., and Eder, B., 2005: Fully coupled “online” chemistry within the WRF model. *Atmos. Environ.* 39, 6957–6975. <https://doi.org/10.1016/j.atmosenv.2005.04.027>
- Gross, A., and Stockwell, W.R., 2003: Comparison of the EMEP, RADM2 and RACM Mechanisms. *J. Atmos. Chem.* 44, 151–170. <https://doi.org/10.1023/A:1022483412112>
- José, R.S., Pérez, J.L., Pecci, J., Garzón, A., and Palacios, M., 2015: Comparison between different dynamical downscaling methods using WRF-Chem for urban applications: Madrid case study. *Int. J. Environ. Pollut.* 58, 293–306. <https://doi.org/10.1504/IJEP.2015.077459>
- Kim S.-W., McDonald B. C., Baidar S., Brown S. S., Dube B., Ferrare R. A., Frost G. J., Harley R. A., Holloway J. S., Lee H.-J., McKeen S. A., Neuman J. A., Nowak J. B., Oetjen H., Ortega I., Pollack I. B., Roberts J. M., Ryerson T. B., Scarino A. J., Senff C. J., Thalman R., Trainer M., Volkamer R., Wagner N., Washenfelder R. A., Waxman E., and Young C. J., 2016: Modeling the weekly cycle of NO_x and CO emissions and their impacts on O₃ in the Los Angeles-South Coast Air Basin during the CalNex 2010 field campaign. *J. Geophys. Res. Atmospheres* 121, 1340–1360. <https://doi.org/10.1002/2015JD024292>
- Kis-Kovács, G., Tarczay, K., Kőbányai, K., Ludányi, E., Nagy, E., and Lovas, K., 2017: Informative Inventory Report 1990–2015. Hungarian Meteorological Service, Unit of National Emissions Inventories, Budapest.
- Knote, C., Tuccella, P., Curci, G., Emmons, L., Orlando, J.J., Madronich, S., Baró, R., Jiménez-Guerrero, P., Luecken, D., Hogrefe, C., Forkel, R., Werhahn, J., Hirtl, M., Pérez, J.L., San José, R., Giordano, L., Brunner, D., Yahya, K., and Zhang, Y., 2015: Influence of the choice of gas-phase mechanism on predictions of key gaseous pollutants during the AQMEII phase-2 intercomparison. *Atmos. Environ.* 115, 553–568. <https://doi.org/10.1016/j.atmosenv.2014.11.066>
- Kong, X., Forkel, R., Sokhi, R.S., Suppan, P., Baklanov, A., Gauss, M., Brunner, D., Barò, R., Balzarini, A., Chemel, C., Curci, G., Jiménez-Guerrero, P., Hirtl, M., Honzak, L., Im, U., Pérez, J.L., Pirovano, G., San Jose, R., Schlünzen, K.H., Tsegas, G., Tuccella, P., Werhahn, J., Žabkar, R., and Galmarini, S., 2015: Analysis of meteorology–chemistry interactions during air pollution episodes using online coupled models within AQMEII phase-2. *Atmos. Environ.* 115, 527–540. <https://doi.org/10.1016/j.atmosenv.2014.09.020>
- Kuik, F., Lauer, A., Churkina, G., Denier van der Gon, H.A.C., Fenner, D., Mar, K.A., and Butler, T.M., 2016: Air quality modelling in the Berlin–Brandenburg region using WRF-Chem v3.7.1: sensitivity to resolution of model grid and input data. *Geosci. Model Develop.* 9, 4339–4363. <https://doi.org/10.5194/gmd-9-4339-2016>
- Leelőssy, Á., Mészáros, R., Kovács, A., Lagzi, I., and Kovács, T., 2017: Numerical simulations of atmospheric dispersion of iodine-131 by different models. *PLoS ONE*, 12, e0172312. <https://doi.org/10.1371/journal.pone.0172312>
- Liao, J., Wang, T., Jiang, Z., Zhuang, B., Xie, M., Yin, C., Wang, X., Zhu, J., Fu, Y., and Zhang, Y., 2015: WRF-Chem modeling of the impacts of urban expansion on regional climate and air pollutants in Yangtze River Delta, China. *Atmos. Environ.* 106, 204–214. <https://doi.org/10.1016/j.atmosenv.2015.01.059>
- Liu, S., Hua, S., Wang, K., Qiu, P., Liu, H., Wu, B., Shao, P., Liu, X., Wu, Y., Xue, Y., Hao, Y., and Tian, H., 2018: Spatial-temporal variation characteristics of air pollution in Henan of China: Localized emission inventory, WRF/Chem simulations and potential source contribution analysis. *Sci. Total Environ.* 624, 396–406. <https://doi.org/10.1016/j.scitotenv.2017.12.102>
- Mar, K.A., Ojha, N., Pozzer, A., and Butler, T.M., 2016: Ozone air quality simulations with WRF-Chem (v3.5.1) over Europe: model evaluation and chemical mechanism comparison. *Geosci. Model Develop.* 9, 3699–3728. <https://doi.org/10.5194/gmd-9-3699-2016>
- Marécal, V., Peuch, V.-H., Andersson, C., Andersson, S., Arteta, J., Beekmann, M., Benedictow, A., Bergström, R., Bessagnet, B., Cansado, A., Chéroux, F., Colette, A., Coman, A., Curier, R.L., Denier van der Gon, H.A.C., Drouin, A., Elbern, H., Emili, E., Engelen, R.J., Eskes, H.J., Foret, G., Friese, E., Gauss, M., Giannaros, C., Guth, J., Joly, M., Jaumouillé, E., Josse, B., Kadyrov,

- N., Kaiser, J.W., Krajsek, K., Kuenen, J., Kumar, U., Liora, N., Lopez, E., Malherbe, L., Martinez, I., Melas, D., Meleux, F., Menut, L., Moinat, P., Morales, T., Parmentier, J., Piacentini, A., Plu, M., Poupkou, A., Queguiner, S., Robertson, L., Rouil, L., Schaap, M., Segers, A., Sofiev, M., Tarasson, L., Thomas, M., Timmermans, R., Valdebenito, A., van Velthoven, P., van Versendaal, R., Vira, J., and Ung, A., 2015: A regional air quality forecasting system over Europe: the MACC-II daily ensemble production. *Geosci. Model Develop.* 8, 2777–2813. <https://doi.org/10.5194/gmd-8-2777-2015>
- Mészáros, R., Lagzi, I., Gelybó, G., and Leelőssy, Á., 2013: Atmospheric Chemistry. Eötvös Loránd University, Budapest.
- Mues, A., Lauer, A., Lupascu, A., Rupakheti, M., Kuik, F., and Lawrence, M.G., 2017: Air quality in the Kathmandu Valley: WRF and WRF-Chem simulations of meteorology and black carbon concentrations. *Geosci. Model Develop Discuss.* 2017, 1–38. <https://doi.org/10.5194/gmd-2017-224>
- Pascal, M., Corso, M., Chanel, O., Declercq, C., Badaloni, C., Cesaroni, G., Henschel, S., Meister, K., Haluza, D., Martin-Olmedo, P., and Medina, S., 2013: Assessing the public health impacts of urban air pollution in 25 European cities: Results of the Aphekom project. *Sci. Total Environment*, 449, 390–400. <https://doi.org/10.1016/j.scitotenv.2013.01.077>
- Stockwell, W.R., Middleton, P., Chang, J.S., and Xiaoyan, T., 1990: The second generation regional acid deposition model chemical mechanism for regional air quality modeling. *J. Geophys. Res. Atmospheres*, 95, 16343–16367. doi:10.1029/JD095iD10p16343
- WHO (Ed.), 2016: Ambient air pollution: A global assessment of exposure and burden of disease. World Health Organization, Geneva, Switzerland, 131 p.
- Zaveri, R.A. and Peters, L.K., 1999: A new lumped structure photochemical mechanism for large-scale applications. *J. Geophys. Res. Atmospheres*, 104, 30387–30415. <https://doi.org/10.1029/1999JD900876>
- Zhang, L., Wang, T., Lv, M., and Zhang, Q., 2015: On the severe haze in Beijing during January 2013: Unraveling the effects of meteorological anomalies with WRF-Chem. *Atmos. Environ.* 104, 11–21. <https://doi.org/10.1016/j.atmosenv.2015.01.001>

IDŐJÁRÁS

*Quarterly Journal of the Hungarian Meteorological Service
Vol. 123, No. 2, April – June, 2019, pp. 217–240*

Detailed validation of EURO-CORDEX and Med-CORDEX regional climate model ensembles over the Carpathian Region

Csaba Zsolt Torma

*Department of Meteorology
Eötvös Loránd University and MTA Post-Doctoral Research Program
Pázmány Péter st. 1/A, H-1117 Budapest, Hungary*

**Corresponding author E-mail: tcsabi@caesar.elte.hu*

(Manuscript received in final form September 24, 2018)

Abstract— Present study evaluates the ability of the ERA-Interim-driven regional climate model (RCM) simulations conducted in the framework of the Coordinated Regional Climate Downscaling Experiment (CORDEX) in describing precipitation and temperature climatic conditions over the Carpathian Region. In total, nine RCM simulations were assessed from EURO-CORDEX and Med-CORDEX (at 0.44° and 0.11° nominal resolutions) against the CARPATCLIM high resolution gridded observational database. Present work focuses on the mean, minimum, and maximum near-surface air temperature and precipitation. The study shows the performance of the members of RCM ensembles in representing the basic spatiotemporal patterns of the climate over the Carpathian Region for the period of 1989–2008. Different metrics covering from daily to monthly and from seasonal to annual time scales are analyzed over the region of interest: spatial patterns of seasonal mean temperature and precipitation, annual cycle of precipitation, monthly mean temperature bias, as well as climate indices, including CDD (consecutive dry days), R95, FD (frost days, when $T_{\min} < 0$ °C), and SU (summer days, when $T_{\max} > 25$ °C). The results confirm the distinct capabilities of RCMs in capturing the local features of the climatic conditions of the Carpathian Region. This work is in favor to select RCMs with reasonable performance over the Carpathian Region, based on which a high-resolution bias-adjusted climatic database can be established for future risk assessment and impact studies.

Key-words: EURO-CORDEX, Med-CORDEX, CARPATCLIM, regional climate model evaluation, Carpathian Region, temperature, precipitation

1. Introduction

Global or regional climate models can be useful tools for providing climate projections including information on human influence on climate and on climate change (IPCC, 2013). However, it is important to note that climate projections can be characterized by various kinds of uncertainties (*Giorgi, 2005*). Uncertainties arising from different model simulations, among others, can be attributed to internal variability (in the absence of any external radiative forcing), to the implemented parameterization and model dynamics (model or response uncertainty), or to the prescribed emission scenarios (scenario uncertainty). Regional climate model projections have inherent additional uncertainties due to the choice of integration domain, resolution, lateral boundary conditions (LBCs).

The evaluation of RCMs as members of ensembles has been recommended as a good practice (*Beniston et al., 2007*) to quantify the uncertainties and extract credible signals. Over the European continent, several RCM-based climate change projects have been accomplished in the last decades: (1) PRUDENCE (Predicting of Regional Scenarios and Uncertainties for Defining European Climate Change Risks and Effects, 2001–2004; *Christensen and Christensen, 2007*), (2) ENSEMBLES (Ensembles-Based Predictions of Climate Changes and Their Impacts, 2004–2009; *Hewitt and Griggs, 2004*), (3) CECILIA (Central and Eastern Europe Climate Change Impact and Vulnerability Assessment, 2006–2009; *Halenka, 2007*). The COordinated Regional Downscaling Experiment (CORDEX, *Giorgi et al., 2009*) is a more recent international initiative with the task of producing reliable regional climate simulations under the supervision of the World Climate Research Programme (WCRP, whose Task Force on Regional Climate Downscaling with a broader scientific community called for the aforementioned initiative). In the framework of CORDEX, several RCM experiments have been accomplished over different sub-regions of the globe. EURO-CORDEX (*Jacob et al., 2013*) and Med-CORDEX (*Ruti et al., 2016*) initiatives provide RCM simulations targeting European regions at grid resolutions of 0.44° (~ 50 km, medium resolution) and of 0.11° (~ 12 km, high resolution). Two main guidelines are followed in designing the CORDEX RCM simulations according to the purposes: model assessment and regional climate projection (*Giorgi et al., 2009; Jones et al., 2011*). Under the model assessment experiments, the RCMs are driven by ERA-Interim reanalysis (*Dee et al., 2011*) providing the LBC, whilst in projections, RCMs are driven by selected GCMs serving climate change information through the twenty-first century.

This work is in favor of giving supporting information on selecting RCMs with good performance in different aspects over the Carpathians and its surrounding territories including the Carpathian Basin (the whole region hereafter referred as the Carpathian Region), and providing information on which a high-resolution bias-adjusted climatic database can be established for risk assessment and impact studies for this region. Overarching aim of the author is to create a

bias-adjusted database including precipitation and temperature data for the Carpathian Region, based on EURO- and Med-CORDEX regional climate model simulations using the CARPATCLIM dataset (Szalai *et al.*, 2013) as reference. Initial steps towards this purpose are reported here.

The Carpathian Region expands between 44°–50° North and 17°–27° East. The Carpathians play an important role in the climate of the Carpathian Region (i.e., by blocking cold air masses from the north), where warm dry Balkans meets with temperate Central Europe and cold continental Eastern Europe (UNEP, 2007). The climate across the Carpathian Region is influenced by oceanic, continental, and mediterranean effects, as well as by orographic factors. The region of interest has quite complex orography, including low lands and high mountain peaks with an altitude range between 27 m and 2655 m (*Fig. 1*). The CARPATCLIM dataset provides daily data over the following countries: Austria, Czech Republic, Croatia, Hungary, Poland, Romania, Serbia, Slovakia, and Ukraine with more than 20 million inhabitants living in that region. The Carpathian Region embraces a significant part of the drainage basins of the main rivers of this region: Danube and Tisza. Recent studies have been published with a special focus on the climate of the Carpathian Region considering the CARPATCLIM dataset (Birsan *et al.*, 2014; Spinoni *et al.*, 2015; Kis *et al.*, 2017) noting that in the work of Kis *et al.*, 2017, the change of precipitation related climatic conditions has been also assessed, but based on simulations of the aforementioned ENSEMBLES project.

Detailed evaluation of EURO-CORDEX and Med-CORDEX RCM simulations driven by the ERA-Interim reanalysis is presented at both resolutions (medium and high) over the Carpathian Region. In total, nine RCM simulations were validated over the region of interest against the CARPATCLIM high resolution gridded observational database. Noting that the relatively high resolution (0.25°) E-OBS observational database (Haylock *et al.*, 2008) is also available encompassing the Carpathians and can serve as reference data (Torma *et al.*, 2011; Szépszó *et al.*, 2014). Considering that CARPATCLIM provides higher station density (compared to E-OBS), data homogenization, and data quality control, this dataset is ideal for validation studies and appropriate reference data for bias correction over the Carpathian Region.

The paper shows the performance of the members of RCM ensembles (EURO- and Med-CORDEX) in representing the basic spatiotemporal patterns of the climatic conditions over the Carpathian Region for the period of 1989–2008. The present study aims to evaluate the near-surface minimum, maximum, and mean air temperature (hereafter referred as *tasmin*, *tasmax*, and *tas*, or temperature, respectively) and precipitation on a European regional scale at different time scales. Furthermore, following previous investigations focusing on RCM performance over regions with complex topography (Frei *et al.*, 2003; Kotlarski *et al.*, 2010; Torma *et al.*, 2015; Giorgi *et al.*, 2016), meteorological variables are assessed over a selected sub-region with a relative high average altitude within the Carpathian Region.

However, it is not the main purpose of the present work to demonstrate the added value of high resolution climate modeling, basic differences between simulations at different resolutions are reported also for the selected mountainous sub-region.

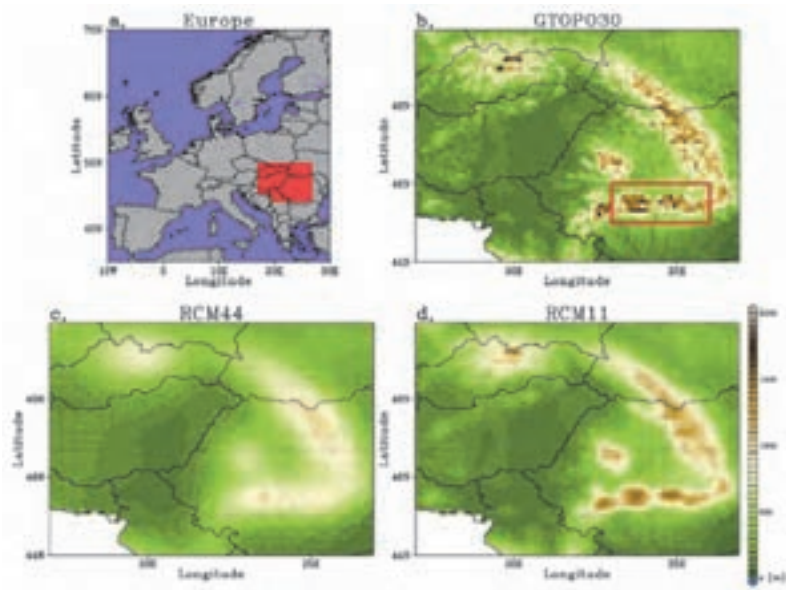


Fig. 1. Analysis regions and topography (on a common 0.11° grid) over the Carpathian Region. a) Location of the analysis region within the whole European domain (area filled with red color); b) topography based on the GTOPO30 database and the mountainous sub-region used in the analysis (red rectangle); c) average topography of the medium resolution RCMs (0.44°); and d) the average topography of high resolution RCMs (0.44°). Units in b), c), and d) are m. Note that the territory of Bosnia and Herzegovina is not covered by the CARPATCLIM dataset.

In Section 2, the reference observational dataset, the assessed RCM simulations, and the applied re-gridding technique along with the evaluation metrics are introduced. Section 3 provides details of RCMs' performance on reproducing climatic conditions over the Carpathian Region followed by Section 4, in which short summary of the results accompanied with concise considerations are given.

2. Data and method

2.1. Observation dataset: CARPATCLIM

The CARPATCLIM dataset provides in total 16 daily meteorological variables (including daily mean, maximum, minimum temperatures and daily precipitation sum) and related derived indicators for the period of 1961–2010 encompassing the Carpathian Region at $0.1^\circ \times 0.1^\circ$ grid resolution (Szalai *et al.*, 2013). The database is station-based, state-of-the-art quality controlled, covers the Carpathian Mountains and the whole Carpathian Basin (approximately 500 000 km²), and freely available for scientific purposes through the following link: <http://www.carpatclim-eu.org>. The technique of Multiple Analysis of Series for Homogenized Database (MASH; Szentimrey and Bihari, 2006) was used for homogenization and data quality control. For interpolation and gridding, the Meteorological Interpolation based on Surface Homogenized Database (MISH; Szentimrey, 2007) method was applied within the CARPATCLIM database. From a network of weather stations covering the Carpathian Region, a number of 415 and 904 stations were used in collecting near surface daily temperature and daily precipitation data, respectively (Spinoni *et al.*, 2015).

One must note that a systematic error related to precipitation measurements is due to the distortion of the wind field above the precipitation gauges. This wind-induced undercatch by precipitation gauges can yield an underestimate as of 20% of actual precipitation, especially over mountainous regions under cold season snow-blowing conditions (Adam and Lettenmaier, 2003). Since the CARPATCLIM dataset originally does not account for the wind-induced precipitation undercatch problem, an additional location-dependent monthly gauge undercatch correction was implemented based on the global precipitation dataset of the University of Delaware (UDel Version 3.01; Legates and Willmott, 1990) following the work of Torma *et al.* (2015). The correction was not applied in the daily precipitation as UDel dataset provides only mean monthly climatological precipitation data.

2.2. RCM simulations

All the nine ERA-Interim driven RCM simulations evaluated in this work are reported in detail in *Table 1*. At the beginning of the present study, from the framework of Med-CORDEX, only three models (ALADIN, RegCM, and PROMES) fulfilled the following requirements: daily precipitation and temperature (mean, minimum, maximum) data are available at both resolutions (0.11° with a corresponding partner at 0.44° using identical model version). Whilst EURO-CORDEX could provide six RCMs (CCLM, HIRHAM, RCA, RACMO, REMO, and WRF) fulfilling the aforementioned criteria. Both integration domains (Med-CORDEX and EURO-CORDEX) entirely include the Carpathian Region, and all simulations cover the period of 1989–2008 with LBCs provided by the ERA-Interim reanalysis.

Table 1: Overview of regional climate models used in the present study. Models provided by the Med-CORDEX framework labeled with an asterisk

Model	Modeling group	Reference
ALADIN 5.2*	Centre National de Recherches Meteorologiques, France	<i>Colin et al., (2010)</i>
CCLM 4.8.17	Climate Limited-area Modelling Community, Germany	<i>Rockel et al., (2008)</i>
HIRHAM 5	Danish Meteorological Institute	<i>Christensen et al., (1998)</i>
PROMES*	Universidad de Castilla-La Mancha, Spain	<i>Castro et al., (1993)</i>
RCA 4	Swedish Meteorological and Hydrological Institute, Rososby Centre, Sweden	<i>Kupiainen et al., (2011)</i>
RACMO 2.2	Royal Netherlands Meteorological Institute, The Netherlands	<i>Meijgaard et al., (2012)</i>
RegCM 4.3*	International Centre for Theoretical Physics, Italy	<i>Giorgi et al., (2012)</i>
REMO	Climate Service Center, Germany	<i>Jacob et al., (2012)</i>
WRF 3.3.1	IPSL (Institut Pierre Simon Laplace) and INERIS (Institut National de l'Environnement industriel et des RISques), France	<i>Skamarock et al., (2008)</i>

The ERA-Interim data is a global atmospheric reanalysis produced by the European Centre for Medium-Range Weather Forecasts (ECMWF). ERA-Interim data is available from 1979 (continuously updated once per month) at approximately 80 km grid resolution and on 60 vertical levels from the surface to 0.1 hPa. Analysis fields were constructed in every 6 hours using a variety of observations, the 4D-Var data assimilation technique, and the version of the ECMWF global model which was operational in 2009. The forcing fields provided by the ERA-Interim for the assessed RCMs include not only atmospheric LBCs, but also sea ice cover and sea surface temperature values.

The EURO-CORDEX simulations are integrated over whole Europe, while Med-CORDEX runs focused more on the Mediterranean region (most of the Scandinavian countries are out of the scope). Additional details of the actual regions of different CORDEX domains can be found on the official CORDEX homepage: <http://cordex.org/>. The RCM simulations of the different model horizontal grid resolutions of 0.11° and 0.44° are hereafter referred as RCM11 and RCM44, respectively. Keep in mind, that the main purpose of including simulations from both original resolutions is to give a general comparative overview of those performance over the region of interest.

2.3. Regridding

Since the RCMs and observational datasets do not share the same horizontal grid, according to a previous assessment with a special focus on added value over region with complex topography (Torma *et al.*, 2015), all simulation data (RCM44 and RCM11) and observational data were interpolated onto a common grid spacing of 0.11° . The interpolation was performed by using the Climate Data Operators software (CDO, <https://code.mpimet.mpg.de/projects/cdo>). The distance-weighted average remapping method was used during the interpolation processes. Though several different interpolation methods are available in the framework of CDO, such as distance weighted, bicubic, bilinear, and field conserving, the distance-weighted method was found to be the most spatial pattern consistent between different resolutions (Torma *et al.*, 2015). Hereafter, all data were evaluated on the common 0.11° grid. Keep in mind, that the main goal of present work is to give comprehensive information on the performances of RCMs in simulating climatic conditions in different aspects, and it is not primary intention to investigate and reveal the possible added value of high resolution computing.

2.4. Evaluation metrics

Different metrics can be used in order to represent the performance of climate models in simulating climatic conditions (Zhao *et al.*, 2013). Besides computing the mean bias and root mean square error (RMSE), the degree of statistical similarity between two climatic fields can be concisely quantified in the form of normalized Taylor diagrams. The diagram, which was originally introduced by Taylor (2001), can be considered as the combination of different measures such as the centered (or bias removed) RMSE, spatial standard deviation (STDV), and spatial correlation. Geometric relationship between these metrics allows that the performance of each model in comparison to CARPATCLIM (serving as reference) can be displayed on the same diagram. The azimuthal position of a symbol in the Taylor diagram gives information on the spatial correlation coefficient between the RCM results and the reference. The radial distances from the origin to each symbol are proportional to the pattern standard deviation normalized by the reference variance, thus reference located at value 1. The distances of each symbol (along concentric circles) from this reference point indicate the centered RMSE based on the RCM and reference data. Note that the centered RMSE values were also standardized with the variance of the reference data. Consequently, symbols representing the best performing RCMs are positioned closest to this reference point. The Taylor diagrams reported in the present study are based on 20-year seasonal means in grid points, except for the assessed climate indices, where 20-year annual means in each grid point were used.

The spatial distribution of mean precipitation, the annual cycle of mean monthly precipitation along with the mean monthly temperature bias averaged over the entire analysis region, as well as the probability distribution function (PDF) of daily precipitation events are also presented in this work. In order to assess the model performances in simulating different characteristics of daily precipitation and temperature, four hydrological and thermal indices are evaluated. The following four precipitation and temperature related climate indices (*Karl et al.*, 1999; *Peterson et al.*, 2001) recommended by the Expert Team in Climate Detection and Indices (ETCCDI) have been examined:

- SU: number of summer days (days with maximum temperature > 25 °C)
- FD: number of frost days (days with minimum temperature < 0 °C)
- CDD: consecutive dry days (number of periods with precipitation < 1 mm/day over at least 5 days)
- R95: fraction of precipitation accounted for by events above the 95th percentile (R95 is computed using all days rather than only days with precipitation > 1 mm)

Note that R95 is relative to a given PDF and is not a measure of absolute extremes, but it is also commonly used in analyzing of extremes (*Sillmann et al.*, 2013; *Giorgi et al.*, 2016).

3. Evaluation of RCM data

3.1. Mean precipitation and temperature characteristics

Before turning our attention to daily precipitation and temperature statistics, it is also important to provide an evaluation of the model performances on simulating the mean precipitation and temperature characteristics throughout the year over the region of interest (*Fig. 1a*). *Fig. 2* represents the annual cycle of monthly precipitation averaged over the Carpathian Region. Information depicted in *Fig. 2* is derived from the ERA-Interim database and from the RCM44 and RCM11 simulations, the CARPATCLIM is also depicted with and without the gauge-correction on the common 0.11° grid. The Carpathian Region experiences a precipitation maximum in summer (June, July) and a minimum in winter (December, January). In general, the RCM ensembles reproduce the annual cycle with a more pronounced precipitation maximum in June. It is also interesting that RCM11 simulations basically give more abundant precipitation during the whole year compared to RCM44 simulations, with the largest extent between May and August, when most of the convective processes occur within the region of interest. Following this, the enhanced precipitation can be attributed to an increase of convective rainfall due to topographical modulation (*Giorgi et al.*, 2016). Such phenomenon is expected to be better represented by simulations where orography is described at higher resolutions (*Torma et al.*, 2015). Both RCM ensembles

generally underestimate the precipitation throughout a relatively warm period between July and September. During spring, precipitation is overestimated (March, April, May), especially by RCM11, even compared to the corrected observations. It can be seen that during October–November–December, the simulated precipitation is more in line with the corresponding field in ERA-Interim than with the observations (CARPATCLIM). One might also notice in Fig. 2, that the spread of RCM simulations does not decrease with higher grid resolution. This fact can be attributed to different factors such as the increased surface internal variability on small scales due to the topographic forcing and locally strong surface heterogeneities at higher resolutions (Separovic *et al.*, 2008), or the amplification of biases already present in the boundary conditions (Laprise *et al.*, 2008). But it is also important to keep in mind, that higher resolution RCM simulations are expected to provide more accurate frequency distributions of daily weather events and extremes rather than decreasing mean bias fields (Giorgi 2006; Laprise *et al.*, 2008; Torma *et al.*, 2015).

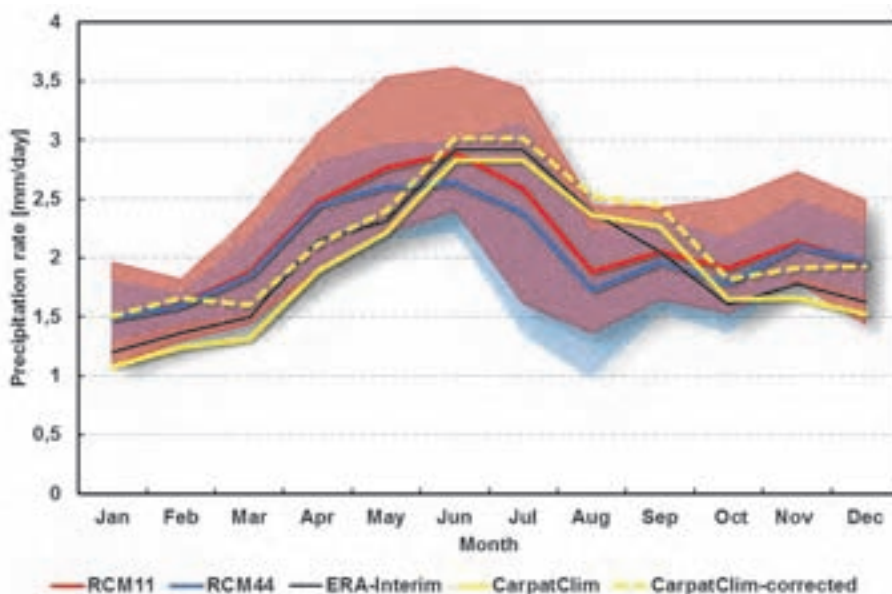


Fig. 2. Monthly mean precipitation averaged over the Carpathian Region for the reference period of 1989–2008 for the ERA-Interim (black), CARPATCLIM (yellow, dashed line stands for the gauge-corrected version), and RCM simulations (ensemble mean of RCM11 with red, ensemble mean of RCM44 with blue). Units are mm/day.

Fig. 3 shows the spatial distribution of mean winter (December-January-February, or DJF), spring (March-April-May, or MAM), summer (June-July-August, or JJA), and autumn (September-October-November, or SON) precipitation for the ensemble average of RCM44 and RCM11 along with the corresponding field in ERA-Interim and CARPATCLIM with and without the gauge correction, all interpolated onto the common 0.11° grid. In general, regardless of the original resolution, RCMs' performance in representing seasonal mean precipitation over the Carpathian Region reflects in cold and warm seasonal dependencies. More specifically, DJF precipitation is slightly overestimated by about 5% by HIRHAM, RCA, and WRF, and exaggeratedly by RegCM (20%). While, in general, all RCMs underestimate JJA precipitation ($\sim 0\%$ – 20%), except for PROMES ($\sim +15\%$). It is worth mentioning that the model REMO underestimates seasonal precipitation for all seasons with an average of 15%. It can be seen that higher resolution comes with an increase in precipitation detail, which phenomenon can be attributed to the topographical features of the Carpathians (*Fig. 1*), and it had been reported over different regions all over Europe in the work of *Fantini et al.* (2016). Analyzing the spatial distributions of seasonal precipitation fields it is evident, that in all seasons the precipitation maxima are mostly topographically induced. The precipitation maxima are found across the western flanks of the northern Carpathians in the observations throughout all the four seasons (DJF, MAM, JJA, SON) with higher values in RCM11 simulations over the southern peaks of the Carpathians. It is also evident, that the effect of the undercatch correction is more prominent in the cold season (DJF) over regions with high elevations.

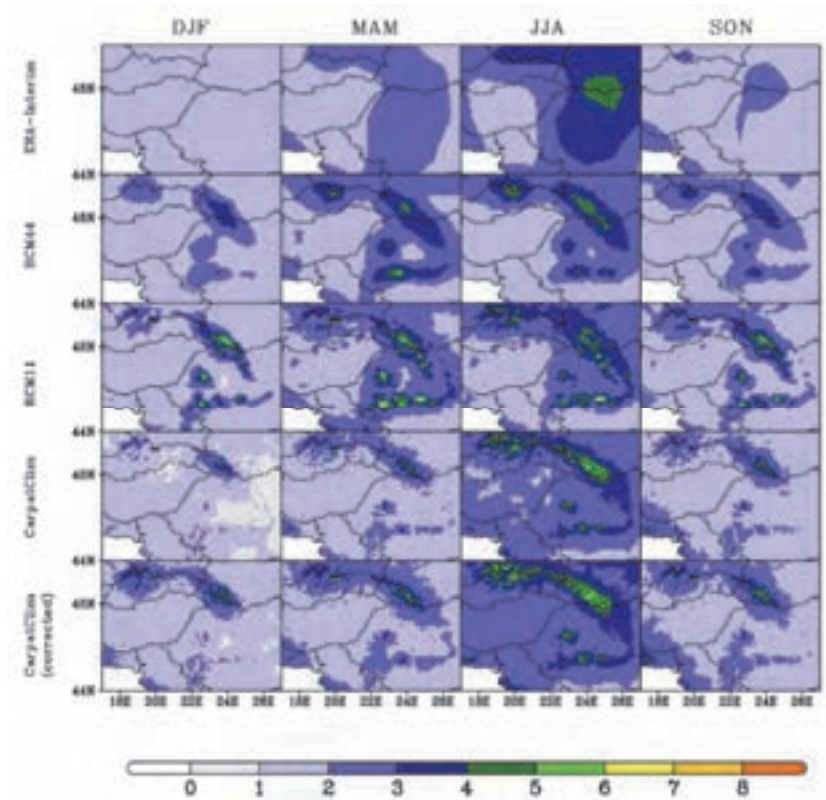


Fig. 3. Mean (1989–2008) winter (December-January-February, DJF), spring (March-April-May, MAM), summer (June-July-August, JJA) and autumn (September-October-November, SON) precipitation for the ERA-Interim (top row) reanalyses, the ensembles of RCM44 and RCM11 (second and third row, respectively) simulations, and the CARPATCLIM observations without and with undercatch gauge correction (last two rows). Units are mm/day.

The centered RMSE along with the STDV and the spatial correlations of RCM44 and RCM11 simulations against CARPATCLIM dataset assessed over the Carpathian Region for the period of 1989–2008 in Fig. 4. The Taylor diagrams enable a direct comparison of different (in sense of resolution and physics) RCM simulations on a common grid (0.11°). In the Taylor diagrams, the high resolution RCM11 simulations are depicted with open circles, while the medium resolution RCM44 simulations are indicated with closed circles. In addition, in Fig. 4, the gauge-corrected CARPATCLIM was used as reference data, since this corrected data is more likely to be representative in sense of mean precipitation climatology over mountainous regions (Torma et al., 2015; Fantini et al., 2018). Also note that the

application of such correction on the observations does not alter significantly the assessed performance metrics (i.e., correlation; *Torma et al., 2015*). During the four seasons, the group of RCM44 simulations is not sharply separated from the RCM11 simulations in general. The biggest uncertainty in representing seasonal mean precipitation over the Carpathian Region occurs in MAM, while relatively the smallest centered RMSE and the highest spatial correlation values can be found in JJA. In DJF (when precipitation shows minimum), the spread of the RCM simulations is relatively small, but at the same time, their performance on simulating the spatial distribution of precipitation is also poor in general. Based on the Taylor diagrams for all four seasons, among the best performing RCMs are as follows: ALADIN, RACMO, and CCLM. In particular RACMO (RCM11) shows the highest spatial pattern correlations, while exhibits one of the best scores in terms of normalized STDV and centered RMSE. Whilst HIRHAM model can be considered as an outlier, as it exhibits qualitatively modest performances regardless of the season. Specifically, it can be seen in case of HIRHAM (RCM44) that large spatial variability (standard deviation ratio generally exceeds 1.5, in season MAM even 2.5) comes along with the largest centered RMSE in all seasons.

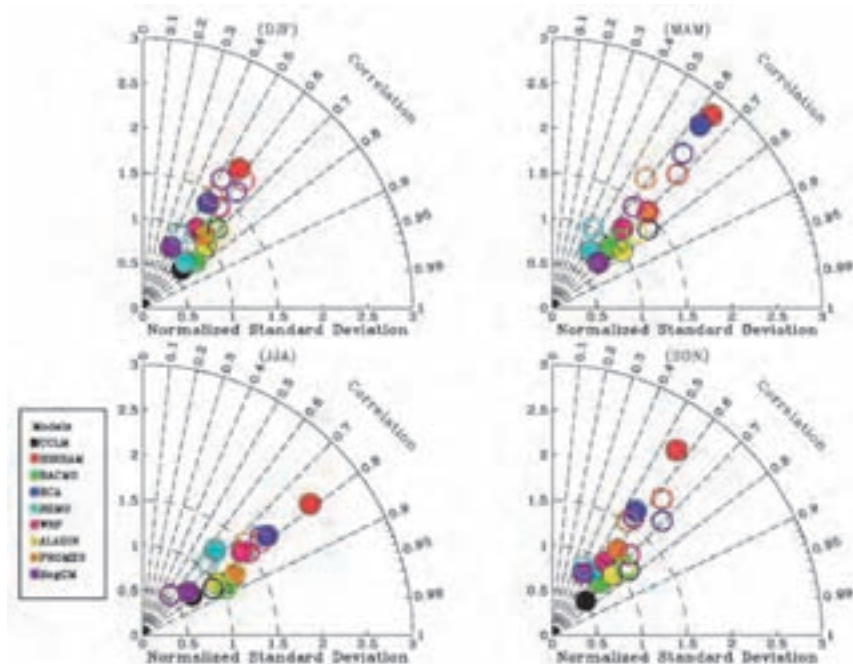


Fig. 4. Taylor diagram of mean (1989–2008) seasonal precipitation for the two model ensembles (filled circles for the RCM44, open circles for the RCM11) versus the gauge-corrected CARPATCLIM observations. The four panels refer to the four seasons (DJF, MAM, JJA, and SON).

In order to reveal more in depth the capacity of RCMs in reproducing climatic conditions over the Carpathian Region, further assessments of additional variables are needed. For this purpose the mean seasonal temperature fields and the annual cycle of mean temperature bias fields averaged over the region of interest for the reference period 1989–2008 are reported in *Figs. 5* and *6*, respectively. *Fig. 5*, following the concept of *Fig. 3*, demonstrates the spatial features of temperature simulations, along with the ERA-Interim and the observations. It must be noticed, that moving towards the originally higher resolution information, the finer the details are in the spatial distribution of the seasonal temperature fields. The Carpathian Mountains play an evident role in the formation of seasonal temperature fields in the Carpathian Region. In all seasons, the peaks of the Carpathians excel with their relatively lower temperature compared to their surroundings. Even the highest peak within the Carpathian Region (Gerlachov Peak, located in Slovakia) can be recognized based on the mean seasonal temperature fields (i.e., MAM and SON) derived from the RCM11 simulations. Additionally, the spatial features of mean seasonal temperature fields of RCM11 simulations even reveal the ranges of Apuseni Mountains (mountain range in Transylvania), which is in fact is valid for all seasons, but not for the RCM44 simulations.

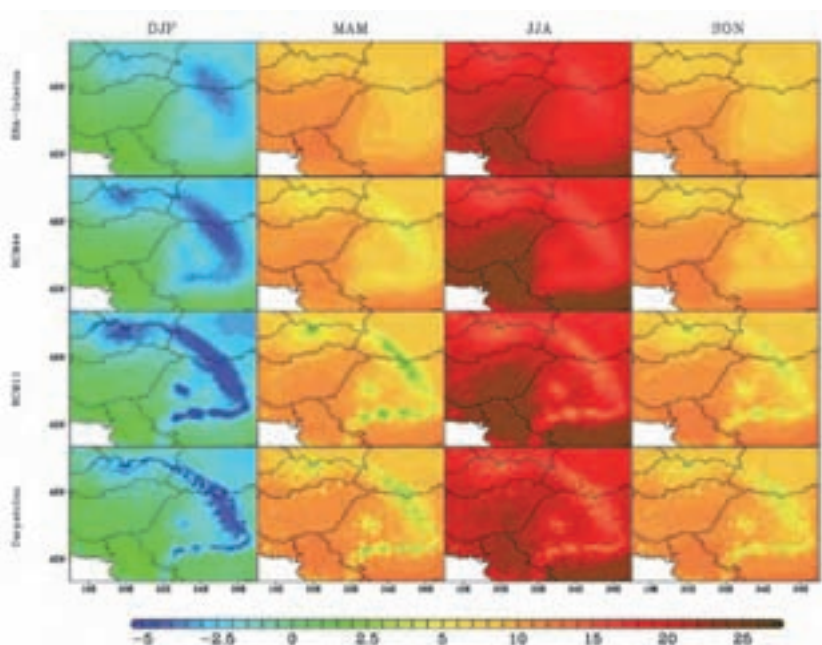


Fig. 5. Mean (1989–2008) winter (December-January-February, DJF), spring (March-April-May, MAM), summer (June-July-August, JJA), and autumn (September-October-November, SON) temperature for the ERA-Interim (top row) reanalyses, the ensembles of RCM44, and RCM11 (second and third row, respectively) simulations, and the CARPATCLIM observations (last row). Units are °C.

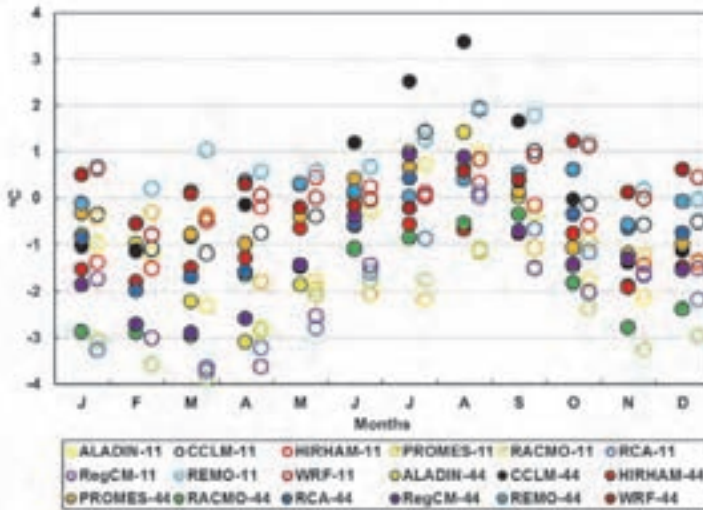


Fig. 6. Monthly mean temperature bias averaged over the Carpathian Region for the reference period of 1989–2008. RCM44 marked with closed circles, while RCM11 are depicted by open circles. Units are °C.

Again, higher resolution RCM simulations are not expected to decrease the mean bias fields (as referred in the previous section), and actually the standard deviation of bias averaged over the Carpathian Region in each month is larger in case of RCM11 compared to the RCM44 ensemble (Fig. 6). The wide range of the spread in monthly biases can be directly attributed to the different topography and parameterizations implemented in the evaluated RCM simulations. Fig. 6 also shows a strong time dependency, as temperature biases are not constant in time. They have a clear annual cycle: there is no RCM with a constant positive or negative temperature bias through the year, temperature is generally overestimated in August, whilst underestimated to a varying extent in the rest of the year. One might also notice, that RCM11 simulations do not always show better performance in simulating cold or warm climatic conditions compared to their partner RCM44 simulations. The spread of bias fields mostly ranges between -3 °C and $+3$ °C, only ALADIN, RegCM, RACMO, RCA (underestimation), and CCLM (overestimation) models are slightly exceeding these limits. RegCM and RACMO typically show a strong cold bias when compared to the CARPATCLIM observational dataset. In general, WRF performs among the best RCMs (median is -0.1 for RCM11 and 0.2 for RCM44): i.e., producing close to zero mean bias during the period of April-May-June-July.

Further assessments are accomplished over a selected sub-region in the Carpathian Region to investigate the benefits of high resolution computing over complex topography. The mountainous sub-region with high mean elevations is highlighted with red box in *Fig. 1b*. All the aforementioned four meteorological variables (pre, tas, tasmin, and tasmax) are evaluated against the CARPATCLIM dataset over this sub-region in the form of Taylor diagram and reported in *Fig. 7* (closed circles represent the RCM44, and open circles are for the RCM11 simulations) for JJA during 1989–2008. As referred previously, higher resolution simulations have the potential to describe more accurately the frequency distributions of daily weather events and extremes, especially over regions with complex topography, when grid resolutions do really matter (*Giorgi, 2006; Laprise et al., 2008; Torma et al., 2015*). Over the mountainous sub-region, higher resolution RCM simulations lead to a slightly improved representation of precipitation, which manifested in higher spatial correlations. RCM11 simulations compared to their RCM44 pairs show increased STDV values, furthermore, all RCM11 simulations overestimate the STDV by exceeding 1 as representative for the reference. During the analyzed period (JJA), when the precipitation maximum occurs, the model REMO realized the poorest performance. At both resolutions, REMO shows displacement of maximum values over the southern ridges of the Carpathians. Moreover, in contrast with observations, a peak with minimum precipitation also appears within the selected sub-region (not shown). Low spatial correlation values (RCM44 REMO exhibits negative correlation) are clear consequences of the aforementioned facts. While in case of precipitation, symbols of RCM44 and RCM11 simulations still overlapping each other, but for temperature (tas, tasmin, and tasmax) evident clusters of RCM44 and RCM11 simulations can be seen, and RCM11 simulations obviously outperform their RCM44 pairs. This can be seen in the improved values of centered RMSE, STDV, and spatial correlations as well. Nevertheless, in the RCM11 simulations, tasmax values are better represented over the selected sub-region than tasmin, as for tasmin they show too high spatial variability. In other seasons similar performances were found (not shown for brevity). It is worth mentioning that CCLM and RACMO models are among the best performing models, which is in line with the previous findings published in the work of *Kotlarski et al. (2017)*.

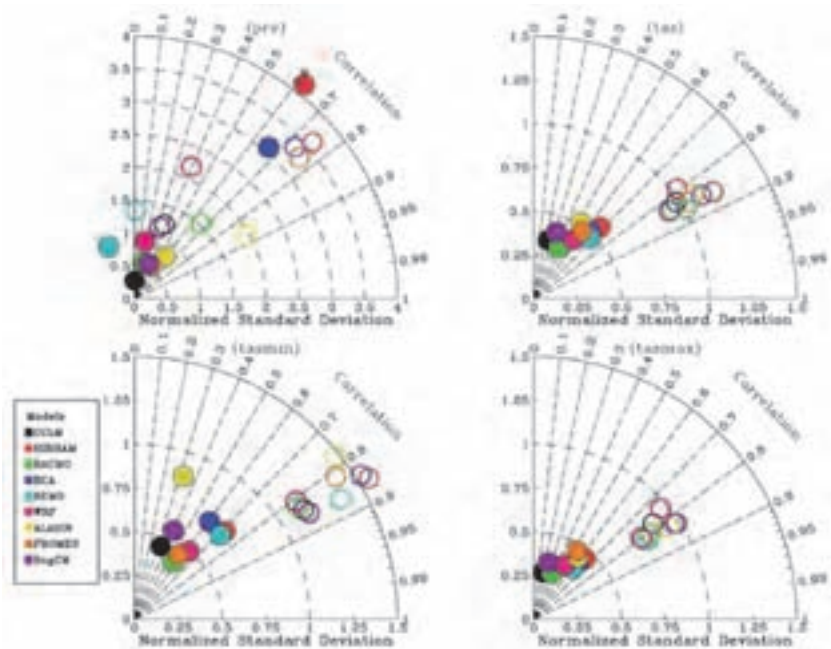


Fig. 7. Taylor diagram of precipitation (pre), temperature (tas), minimum temperature (tasmin), and maximum temperature (tasmax) (closed circles for the RCM44, open circles for RCM11 simulations) versus the CARPATCLIM observations (the gauge-corrected observations in case of precipitation) over the mountainous region for JJA in the period of 1989–2008.

3.2. Climate indices

In order to investigate the daily precipitation intensities, Fig. 8 presents the PDFs of all daily precipitation during the period of 1989–2008 from RCM11 and RCM44 ensembles. All data were interpolated onto the 0.11° resolution grid of the Carpathian Region along with the corresponding observational dataset. On average, the RCM simulations appear to be consistent with the low-intensity tail of observed distribution (up to about 50 mm/day), but mostly overestimate the frequency of the high-intensity events (exceeding 100 mm/day), especially RCM11. PDFs derived from RCM44 simulations are more in line with observations than their higher resolution partners, which is in fact the opposite what was found for another European regions with complex topography (Torma *et al.*, 2015). There are different possible explanations for this finding. On the one hand, these results can be attributed to the fact that RCMs can simulate unrealistic high precipitation intensities at high grid resolutions over different regions (i.e., due to the sensitivity of the implemented convective parameterization). On the other hand, these results

might reveal some deficiencies of the CARPATCLIM reference dataset, as the effective resolution might be lower than the nominal 0.1° over regions of low station network density (Fantini et al., 2016; Kotlarski et al., 2017). As a direct consequence of this, CARPATCLIM dataset might underrepresent the frequency of the events with high precipitation over those regions. Both explanations turn attention to exciting challenges arise in regional climate modeling.

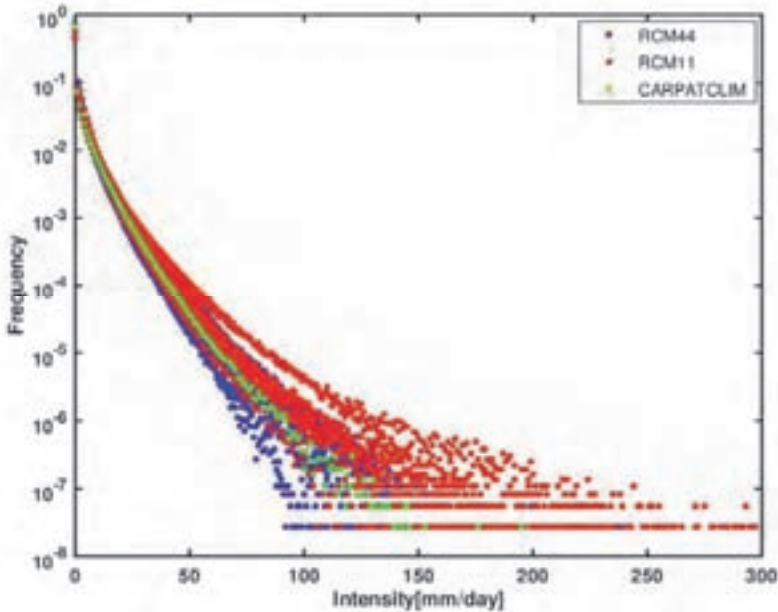


Fig. 8. Daily precipitation intensity empirical probability distribution functions (PDFs) (frequency versus intensity of daily precipitation events for the period of 1989–2008) for RCM44 (blue) and RCM11 (red) model experiments, and the CARPATCLIM observations (green).

Fig. 9 shows the spatial distribution of R95 for the RCM44 and RCM11 ensemble means with the corresponding observations. The R95 metric was defined in Section 2.4 and is calculated including all days with no additional restrictions in the reference period (1989–2008). The observed values of R95 at the common 0.11° resolution grid vary mostly in the range of 24–38%, with some higher peaks in the southern-southeastern part of the Carpathians and over a smaller region in the western part of the Carpathian Region. Sharp contrast can also be noticed between the western/eastern and northern/southern sides of the Carpathians, while R95 has generally lower values on the west, but higher values

on the east, and shows more prominent maximum over the southern part of the southern range of the Carpathians. This contrast can be found in both RCM ensembles, but only RCM11 ensemble presents the two aforementioned regions with high R95 values. By and large, RCM44 ensemble can capture well the locations of R95 maxima and minima, but typically underestimates them and misses the high resolution details with the corresponding locations of maxima, indicating the benefits of using higher resolution information in the assessment of R95.

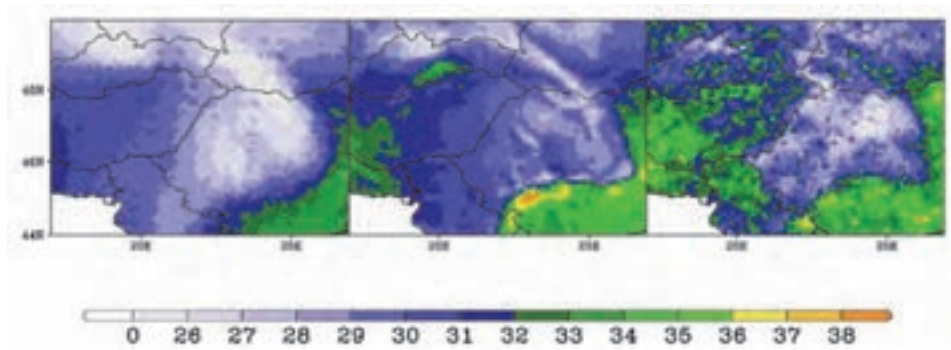


Fig. 9. Ensemble mean of R95 index for the RCM ensembles (RCM44 on the left panel, RCM11 on the middle panel) and the CARPATCLIM observations (right panel) for the period of 1989–2008. Units are in percent of total precipitation accounted for by events above the 95th percentile.

Fig. 10 summarizes the performances of individual RCM11 and RCM44 simulations against the CARPATCLIM observational dataset in representing the CDD, R95, FD, and SU climate indices over the mountainous sub-region within the Carpathian Region. Taylor diagrams for CDD and R95 demonstrate that simulation of days with low or no precipitation can be quite challenging over regions with complex topography for the RCMs. In case of the CDD, regardless the RCM, higher resolution typically manifested in higher STDV and spatial correlation values, except for HIRHAM. RCM44 version of REMO shows negative correlation, whereas CCLM and ALADIN results could be considered as the best ones. For R95, RCMs showed better agreement with the reference dataset compared to the CDD. Among RCM11 simulations, CCLM and RACMO models provides remarkably better results, while HIRHAM, PROMES, and RegCM models performed more modestly. From overlap of symbols for RCM44 and RCM11 simulations one can conclude that not all RCM11 members show improvement with respect to the RCM44 members.

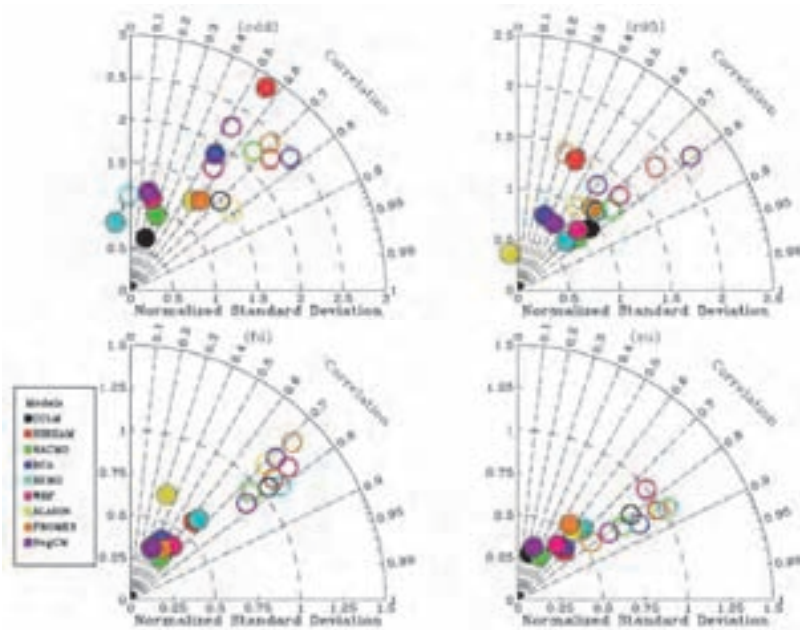


Fig. 10. Same as Fig. 7, but for annual values of climate indices CDD (top left), R95 (top right), FD (bottom left), and SU (bottom right). Note that no additional gauge-correction was implemented on daily observational data.

In general, RCMs perform better in reproducing thermal climatic conditions than simulating precipitation events. This can be attributed to the fact that precipitation shows higher variability in space and time than temperature, thus it is more challenging to be simulated by RCMs. For FD and SU, a clear separation of RCM44 and RCM11 ensemble members can be seen. RCM11 versions of CCLM, RACMO, and REMO simulate FD with good agreement over the sub-region. As member of the same ensemble, PROMES showed weaker results for both temperature indices. In case of the SU index, the high resolution simulations of HIRHAM, ALADIN, and REMO provided the most reasonable results (noting that in other aspects as showed earlier, HIRHAM was considered as an outlier). These findings can support the fact that higher resolution RCM simulations can give more valuable information on extremes and climate indices than coarser ones. All the results reported in the present study demonstrate the lack of a single model above all other models.

4. Summary and final considerations

In the present study, nine RCMs as members of the European branches of CORDEX (EURO- and Med-CORDEX) have been evaluated over a 20-year long reference period (1989–2008) against the high-resolution, gridded CARPATCLIM observational dataset. Overarching aim of the present study is to provide useful information on general capabilities of given RCMs in reproducing climatic conditions over the Carpathian Region. All RCM simulations provided daily precipitation and temperature (tas, tasmin, and tasmax) data at both nominal resolutions of 0.11° and 0.44° , and have been evaluated on a common 0.11° grid against the CARPATCLIM dataset.

By and large, the annual precipitation cycle averaged over the Carpathian Region is well represented by both RCM44 and RCM11 ensembles. According to the spatial distribution of seasonal precipitation, RCM11 generally produced a more pronounced precipitation maxima over the southern peaks of the Carpathians compared to RCM44. ALADIN, CCLM, and RACMO exhibited good results, while HIRHAM showed relatively poor performances in simulating mean precipitation fields regardless of the season. The average temperature bias values range between -3°C and $+3^\circ\text{C}$. WRF (RCM11) could be considered as one of the best performing RCMs, while for among others, RegCM, and RCA showed strong cold bias through the year in the analyzed period. Over a selected sub-region described as region with high mean elevation, RACMO and CCLM provided the best agreement with the CARPATCLIM dataset for JJA in all aspects (pre, tas, tasmin, and tasmax). Further climate indices (FD, SU, CDD, and R95) were computed and assessed over the entire region of interest and over the sub-region as well. In general, in case of the temperature related climate indices (FD and SU), RCM11 ensemble showed better agreement with observations than RCM44 ensemble. For FD and SU climate indices, PROMES model showed relatively poor performance. While the models ALADIN, HIRHAM, and REMO were found to be the best in representing FD and SU over the selected sub-region, respectively. In general, CCLM represented remarkably good performances for CDD and R95, while HIRHAM is found to show modest results.

According to the findings reported in the present work, the following considerations can be made: (1) there is not a single RCM outperforming the other ones in all aspects, but it is also important to note that all RCMs have their strength and weaknesses; (2) better description of extremes and climate indices can be achieved by applying higher resolution simulations; (3) due to the amplification of biases already present in the BCs or the increased internal variability on small scales induced by strong local surface heterogeneities within the regional domain, higher resolution RCM simulations not necessarily reduce the uncertainties; (4) RCM performances are also influenced by observational uncertainties. On the one hand, observational uncertainties might be high over regions with relatively sparse station network, especially over regions with high elevations (*Prein and Gobiet*,

2017). On the other hand, the ever increasing resolution of current state-of-the-art RCMs constantly requires and highlights the need of quality controlled, high resolution observational datasets for their assessment and development. Such comprehensive evaluations discussed in the present study cannot be done on a continental scale (i.e., over entire Europe), only over sub-regions covered by high-quality, high resolution observational datasets such as the CARPATCLIM. This statement draws attention to the fact, that there is still an urgent need in integrating such observational datasets over the entire European continent.

Acknowledgements: The research leading to these results has received funding from the Hungarian Academy of Sciences under the Premium Post-Doctoral Research Program. All data from EURO-CORDEX and Med-CORDEX modeling groups used in this work and CARPATCLIM, Database © European Commission – JRC 2013, along with GTOPO30 data provided by the U.S. Geological Survey are acknowledged. The data used in this work can be found at the following web sites: <http://cordexesg.dmi.dk/esgf-web-fe/> (EURO-CORDEX), <http://www.medcordex.eu/medcordex.php> (Med-CORDEX), <http://www.carpatclim-eu.org/pages/download/> (CARPATCLIM), and https://www.esrl.noaa.gov/psd/data/gridded/data.UDel_AirT_Precip.html (UDeI). The author is also grateful to the anonymous reviewer for thorough revision of the manuscript, which helped to significantly improve the quality of the paper.

References

- Adam, J.C. and Lettenmaier, D.P., 2003: Adjustment of global gridded precipitation for systematic bias. *J. Geophys. Res.* 108(D9), 4257. <https://doi.org/10.1029/2002JD002499>
- Beniston, M., Stephenson, D.B., Christensen, O.B., Ferro, C.A.T., Frei, C., Goyette, S., Halsnaes, K., Holt, T., Jylhä, K., Koffi, B., Palutikof, J., Schöll, R., Semmler, T., and Woth, K., 2007: Future extreme events in European climate: An exploration of regional climate model projections. *Climat. Change* 81 S1, 71–95. <https://doi.org/10.1007/s10584-006-9226-z>
- Birsan, M.-V., Dumitrescu, A., Micu, D.M., and Cheval, S., 2014: Changes in annual temperature extremes in the Carpathians since AD 1961. *Nat Hazards* 74, 1899–1910. <https://doi.org/10.1007/s11069-014-1290-5>
- Castro, M., Fernández, C., and Gaertner M.A., 1993: Description of a mesoscale atmospheric numerical model. In: (eds. Díaz JI, Lions JL) *Mathematics, climate and environment. Recherches en Mathematics Appliques Series Mason*, 230–253.
- Christensen, O.B., Christensen, J.H., Machenhauer, B., and Botzet, M., 1998: Very high-resolution regional climate simulations over Scandinavia - Present climate. *J Climate* 11, 3204–3229. [https://doi.org/10.1175/1520-0442\(1998\)011<3204:VHRRCS>2.0.CO;2](https://doi.org/10.1175/1520-0442(1998)011<3204:VHRRCS>2.0.CO;2)
- Christensen, J.H. and Christensen, O.B., 2007: A summary of the PRUDENCE model projections of changes in European climate by the end of this century. *Climatic Change* 81 S1,7–30. <https://doi.org/10.1007/s10584-006-9210-7>
- Colin, J., Deque, M., Radu, R., and Somot, S., 2010: Sensitivity study of heavy precipitation in limited area model climate simulations: influence of the size of the domain and the use of the spectral nudging technique. *Tellus A* 62, 591–604. <https://doi.org/10.1111/j.1600-0870.2010.00467.x>
- Dee, D.P., Uppala, S.M., Simmons, A.J., Berrisford, P., Poli, P., Kobayashi, S., Andrae, U., Balmaseda, M. A., Balsamo, G., Bauer, P., Bechtold, P., Beljaars, A. C. M., van de Berg, L., Bidlot, J., Bormann, N., Delsol, C., Dragani, R., Fuentes, M., Geer, A. J., Haimberger,

- L., Healy, S. B., Hersbach, H., Hólm, E. V., Isaksen, L., Kållberg, P., Köhler, M., Matricardi, M., McNally, A. P., Monge-Sanz, B. M., Morcrette, J.-J., Park, B.-K., Peubey, C., de Rosnay, P., Tavolato, C., Thépaut, J.-N. and Vitart, F., 2011: The ERA-Interim reanalysis: configuration and performance of the data assimilation system. *Quart. J.Roy. Meteor. Soc.* 137, 553–597. <https://doi.org/10.1002/qj.828>
- Fantini, A., Raffaele, F., Torma, Cs., Bacer, S., Coppola, E., and Giorgi, F., 2018: Assessment of multiple daily precipitation statistics in ERA-Interim driven Med-CORDEX and EURO-CORDEX experiments against high resolution observations. *Climat. Dynam.* 51, 877–900. <https://doi.org/10.1007/s00382-016-3453-4>
- Frei, C., Christensen, J. H., Déqué, M., Jacob, D., Jones, R. G., and Vidale, P. L., 2003: Daily precipitation statistics in regional climate models: Evaluation and intercomparison for the European Alps. *J. Geophys. Res.* 108, 4124. <https://doi.org/10.1029/2002JD002287>
- Giorgi, F., 2005: Climate change prediction. *Climatic Change* 73, 239–265. <https://doi.org/10.1007/s10584-005-6857-4>
- Giorgi, F., 2006: Regional climate modeling: Status and perspectives. *J. Phys.* IV, 139, 101–118. <https://doi.org/10.1051/jp4:2006139008>
- Giorgi, F., Jones, C., and Ghassem, A., 2009: Addressing climate information needs at the regional level, The CORDEX framework. *WMO Bull* (July 2009 issue)
- Giorgi, F., Coppola, E., Solmon, F., Mariotti, L., Sylla, MB., Bi, X., Elguindi, N., Diro, GT., Nair, V., Giuliani, G., Turuncoglu, UU., Cozzini, S., Güttler, I., O'Brien, TA., Tawfik, AB., Shalaby, A., Zakey, AS., Steiner, AL., Stordal, F., Sloan, LC., Branković, C., 2012: RegCM4: model description and preliminary tests over multiple CORDEX domains. *Climat. Res.* 52, 7–29. <https://doi.org/10.3354/cr01018>
- Giorgi, F., Torma, Cs., Coppola, E., Ban, N., Schär, C., Somot, S., 2016: Enhanced summer convective rain at Alpine high elevations in response to climate warming. *Nat. Geosci.* 9, 584–589. <https://doi.org/10.1038/ngeo2761>
- Halenka, T., 2007: On the Assessment of Climate Change Impacts in Central and Eastern Europe - EC FP6 Project CECILIA. *Geophys. Res. Abst.* 9, 10545.
- Haylock, M.R., Hofstra, N., Tank, AMG., Klok, E.J., Jones, P.D., and New, M., 2008: A European daily high-resolution gridded dataset of surface temperature and precipitation for 1950–2006. *J. Geophys. Res. (Atmospheres)* 113 (D20119): 12. <https://doi.org/10.1029/2008JD10201>
- Hewitt, C.D. and Griggs, D., 2004: Ensembles-Based Predictions of Climate Changes and Their Impacts. *Eos Trans. AGU*, 85(52). <https://doi.org/10.1029/2004EO520005>
- IPCC, 2013: Climate Change 2013: The Physical Science Basis. Contribution of Working Group I to the Fifth Assessment Report of the Intergovernmental Panel on Climate Change (eds. Stocker, T.F., D. Qin, G.-K. Plattner, M. Tignor, S.K. Allen, J. Boschung, A. Nauels, Y. Xia, V. Bex and P.M. Midgley). Cambridge University Press, Cambridge, United Kingdom and New York, NY, USA. <https://doi.org/10.1017/CBO9781107415324>
- Jacob, D., Elizalde, A., Haensler, A., Hagemann, S., Kumar, P., Podzun, R., Rechid, D., Remedio, A.R., Saeed, F., Sieck, K., Teichmann, C., and Wilhelm, C., 2012: Assessing the transferability of the regional climate model REMO to different coordinated regional climate downscaling experiment (CORDEX) regions. *Atmosphere* 3, 181–199. <https://doi.org/10.3390/atmos3010181>
- Jacob, D., Petersen, J., Eggert, B., Alias, A., Christensen, O.B., Bouwer, L.M., Braun, A., Colette, A., Déqué, M., Georgievski, G., Georgopoulou, E., Gobiet, A., Menut, L., Nikulin, G., Haensler, A., Hempelmann, N., Jones, C., Keuler, K., Kovats, S., Kröner, N., Kotlarski, S., Kriegsman, A., Martin, E., van Meijgaard, E., Moseley, C., Pfeifer, S., Preuschmann, S., Radermacher, C., Radtke, K., Rechid, D., Rounsevel, M., Samuelsson, P., Somot, S., Soussana, J.-F., Teichmann, C., Valentini, R., Vautard, R., Weber, B., and

- Yiou, P., 2013: EURO-CORDEX: new high resolution climate change projections for European impact research. *Reg. Environ. Change* 14, 563–578.
<https://doi.org/10.1007/s10113-013-0499-2>
- Jones, C., Giorgi, F., and Asrar, G., 2011: The coordinated regional downscaling experiment: CORDEX. An international downscaling link to CMIP5. *CLIVAR Exch* 16, 34–40.
- Karl, T.R., Nicholls, N., and Ghazi, A., 1999: CLIVAR/GCOS/WMO workshop on indices and indicators for climate extremes: workshop summary. *Clim. Change* 42, 3–7.
<https://doi.org/10.1023/A:1005491526870>
- Kis, A., Pongrácz, R., and Bartholy, J., 2017: Multi-model analysis of regional dry and wet conditions for the Carpathian Region. *Int. J. Climatol.* 37, 4543–4560.
<https://doi.org/10.1002/joc.5104>
- Kotlarski, S., Paul, F., and Jacob, D., 2010: Forcing a Distributed Glacier Mass Balance Model with the Regional Climate Model REMO. Part I: Climate Model Evaluation. *J. Climate* 23, 1589–1606. <https://doi.org/10.1175/2009JCLI2711.1>
- Kotlarski, S., Szabó, P., Herrera, S., Rätty, O., Keuler, K., Soares, P. M., Cardoso, R. M., Bosshard, T., Pagé, C., Boberg, F., Gutiérrez, J. M., Isotta, F. A., Jaczewski, A., Kreienkamp, F., Liniger, M. A., Lussana, C., and Pianko-Kluczyńska, K., 2017: Observational uncertainty and regional climate model evaluation: a pan-European perspective. *Int. J. Climatol.* <https://doi.org/10.1002/joc.5249>
- Kupiainen, M., Samuelsson, P., Jones, C., Jansson, C., Willén, U., Hansson, U., Ullerstig, A., Wang, S., and Döscher, R., 2011: Rossby centre regional atmospheric model, RCA4. Rossby Centre Newsletter.
- Laprise, R., de Elia, R., Caya, D., Biner, S., Lucas-Picher, P., Diaconescu, E., Leduc, M., Alexandru, A., and Separovic, L., 2008: Challenging some tenets of Regional Climate Modelling, *Meteorol. Atmos. Phys.* 100, 3–22. <https://doi.org/10.1007/s00703-008-0292-9>
- Legates, D.R. and Willmott, C. J., 1990: Mean seasonal and spatial variability in gauge-corrected, global precipitation. *Int. J. Climatol.* 10, 111–127.
- Meijgaard, E. van, Ulft, L.H. van, Lenderink, G., Roode, S.R. de, Wipfler, E.L., Boers, R., and Timmermans, R.M.A. van, 2012: Refinement and application of a regional atmospheric model for climate scenario calculations of Western Europe. *Climate Changes Spatial Planning Publication: KvR 054/12*.
- Peterson, T.C., Folland, C., Gruza, G., Hogg, W., Mokssit, A., and Plummer, N., 2001: Report on the activities of the working group on climate change detection and related rapporteurs 1998–2001. World Meteorological Organisation Rep. WCDMP-47, WMO-TD 1071, Geneva, Switzerland.
- Prein, A.F. and Gobiet, A., 2017: Impacts of uncertainties in European gridded precipitation observations on regional climate analysis. *Int. J. Climatol.* 37, 305–327.
<https://doi.org/10.1002/joc.4706>
- Rockel, B., Castro, C.L., Pielke, R.A. Sr, von Storch, H., and Lencini, G., 2008: Special issue regional climate modelling with COSMO-CLM (CCLM). *Meteorol Z* 17, 347–348.
<https://doi.org/10.1127/0941-2948/2008/0309>
- Ruti, P.M., Somot, S., Giorgi, F., Dubois, C., Flaounas, E., Obermann, A., Dell’Aquila, A., Pisacane, G., Harzallah, A., Lombardi, E., Ahrens, B., Akhtar, N., Alias, A., Arsouze, T., Aznar, R., Bastin, S., Bartholy, J., Béranger, K., Beuvier, J., Bouffies-Cloché, S., Brauch, J., Cabos, W., Calmanti, S., Calvet, J.-C., Carillo, A., Conte, D., Coppola, E., Djurdjevic, V., Drobinski, P., Elizalde-Arellano, A., Gaertner, M., Galàn, P., Gallardo, C., Gualdi, S., Goncalves, M., Jorba, O., Jordà, G., L’Heveder, B., Lebeau-pin-Brossier, C., Li, L., Liguori, G., Lionello, P., Maciàs, D., Nabat, P., Onol, B., Raikovic, B., Ramage, K., Sevault, F., Sannino, G., Struglia, M.V., Sanna, A., Torma, Cs., and Vervatis, V., 2016: MED-CORDEX initiative for Mediterranean Climate studies, *Bull. Amer. Meteor. Soc.* 97, 1187–1208. <https://doi.org/10.1175/BAMS-D-14-00176.1>

- Separovic, L., de Elia, R., and Laprise, R., 2008: Reproducible and irreproducible components in ensemble simulations of a regional climate model. *Clim. Dynam.* 136, 4942–4961. <https://doi.org/10.1175/2008MWR2393.1>
- Sillmann, J., Kharin, V.V., Zwiers, F.W., Zhang, X., and Bronaugh, D., 2013: Climate extreme indices in the CMIP5 multi-model ensemble: Part 2. Future climate projections. *J. Geophys. Res. Atmos.*, 118, 2473–2493. <https://doi.org/10.1002/jgrd.50188>
- Skamarock, W.C., Klemp, J.B., Dudhia, J., Gill, D.O., Duda, M.G., Huang, X.-Y., Wang, W., and Powers, J.G., 2008: A description of the advanced research WRF version 3. *NCAR Technical note 475*.
- Spinoni, J., Szalai, S., Szentimrey, T., Lakatos, M., Bihari, Z., Nagy, A., Németh, Á., Kovács, T., Mihic, D., Dacic, M., Petrovic, P., Kržič, A., Hiebl, J., Auer, I., Milkovic, J., Štěpánek, P., Zahradnick, P., Kilar, P., Limanowka, D., Pyrc, R., Cheval, S., Birsan, M.-V., Dumitrescu, A., Deak, G., Matei, M., Antolovic, I., Nejedlik, P., Štastný, P., Kajaba, P., Bochnicek, O., Galo, D., Mikulová, K., Nabyvanets, Y., Skrynyk, O., Krakovska, S., Gnatiuk, N., Tolasz, R., Antofie, T., and Vogt, J., 2015: Climate of the Carpathian region in the period 1961–2010: climatologies and trends of 10 variables. *Int. J. Climatol.* 35, 1322–1341. <https://doi.org/10.1002/joc.4059>
- Szalai, S., Auer, I., Hiebl, J., Milkovich, J., Radim, T., Stepanek, P., Zahradnick, P., Bihari, Z., Lakatos, M., Szentimrey, T., Limanowka, D., Kilar, P., Cheval, S., Deak, Gy., Mihic, D., Antolovic, I., Mihajlovic, V., Nejedlik, P., Stastny, P., Mikulova, K., Nabyvanets, I., Skryryk, O., Krakovskaya, S., Vogt, J., Antofie, T., and Spinoni, J., 2013: Climate of the Greater Carpathian Region. Final Technical Report. <http://www.carpatclim-eu.org>
- Szentimrey, T. and Bihari, Z., 2006: MISH (Meteorological Interpolation based on Surface Homogenized Data Basis). COST Action 719 Final Report, The use of GIS in climatology and meteorology, Edited by Ole Einar Tveito, Martin Wegehenkel, Frans van der Wel and Hartwig Dobesch, 2006, 54–56.
- Szentimrey, T., 2007: Manual of homogenization software MASHv3.02. Hungarian Meteorological Service.
- Szépszó, G., Lingemann, I., Klein, B., and Kovács, M., 2014: Impact of climate change on hydrological conditions of Rhine and Upper Danube rivers based on the results of regional climate and hydrological models. *Nat Hazards* 72, 241–262. <https://doi.org/10.1007/s11069-013-0987-1>
- Taylor, K.E., 2001: Summarizing multiple aspects of model performance in a single diagram. *J. Geophys. Res.* 106, 7183–7192. <https://doi.org/10.1029/2000JD900719>
- Torma Cs., Coppola, E., Giorgi, F., Bartholy, J., and Pongrácz, R., 2011: Validation of a high resolution version of the regional climate model RegCM3 over the Carpathian Basin. *J. Hydrometeor.* 12, 84–100. <https://doi.org/10.1175/2010JHM1234.1>
- Torma, Cs., Giorgi, F., and Coppola, E., 2015: Added value of regional climate modeling over areas characterized by complex terrain - Precipitation over the Alps. *J. Geophys. Res. Atmos.*, 120, 3957–3972. <https://doi.org/10.1002/2014JD022781>
- UNEP, 2007: Carpathian environmental outlook—KEO2007. United Nations Environment Programme.
- Zhao, Z.-C., Luo, Y., and Huang, J.-B., 2013: A review on evaluation methods of climate modeling. *Adv. Clim. Change Res.*, 4, 137–144. <https://doi.org/10.3724/SP.J.1248.2013.137>

IDŐJÁRÁS

Quarterly Journal of the Hungarian Meteorological Service
Vol. 123, No. 2, April – June, 2019, pp. 241–264

Fog climatology in Hungary

**Anikó Cséplő^{1*}, Noémi Sarkadi¹, Ákos Horváth², Gabriella Schmeller¹,
and Tünde Lemler²**

¹*University of Pécs, Faculty of Sciences
Institute of Geography and Earth Sciences
Ifjúság útja 6, 7624 Pécs, Hungary*

²*Hungarian Meteorological Service
Storm Warning Observatory
Vitorlás utca 17, 8600 Siófok, Hungary*

**Corresponding author E-mail: acseplo@gamma.ttk.pte.hu*

(Manuscript received in final form June 25, 2018)

Abstract—The fog not only makes the traffic more difficult, but it is frequently accompanied by increased air pollution. A research program has been started recently to improve our knowledge about fog both in macro and micro scales. In the first part of the research project, analysis of the data collected in the last 60 years has been performed. This database contains information about the visibility and the duration of the reduced visibility at 8 different cities in different regions of Hungary. The climatology of fog in Hungary has been studied in only few research programs, and no comprehensive analysis of the data has been performed. The first results of the data analysis show that the frequency and duration of the mist significantly reduced between the 1980s and 2000s, and the most dramatic reduction occurred in the northeast region of the country. Furthermore, the frequency of fog also dropped in this time period. The most dramatic reduction of the fog and mist events was found in northeastern Hungary, which was one of the most polluted regions in the country until the 90s of the last century. The coincidence of the significant reduction of duration of fog and that of the sulfate emission in NE Hungary supports the hypothesis that there is a strong correlation between the air pollution and the formation of the mist and fog.

Key-words: fog, mist, fog climatology, statistical analysis

1. Introduction

Low visibility due to fog increases the hazard of the traffic on road, landing of airplanes or shipping in the coastal area. The fog is frequently accompanied by enhanced air pollution, which can significantly increase the health risk.

The reduced horizontal visibility can be caused by rainfall, fog, smog, haze, mist, and even sand storm. The fog is defined as an atmospheric phenomenon which reduces the visibility below 1 km due to suspended water droplets nearby surface of the Earth (*National Oceanic and Atmospheric Administration*, 1995) (*WMO*, 2011). The reduced visibility in case of mist is between 1 km and 5 km. (*WMO*, 2011). The fog is a greatly localized phenomenon, because the conditions necessary for its formation – increased moisture content and/or cooling of air mass – are typically influenced by geographical characteristic of location where fog forms (*Peace*, 1969).

In Hungary, only few papers have been published about the characteristics of the fog. These studies have examined mainly the physics of fog, the characteristics of fog at different meteorological conditions, and have analyzed data about reduced visibility at some airports. The results of these researches were published in the middle decades of the 20th century. These studies focused on local regions in Hungary; comprehensive, climatological analysis of the available data has not been accomplished.

In the fog-prone regions of the world, some scientists investigated the microphysics of fog to improve the forecast and understanding of fog formation. The spatial and temporal frequency of fog have been studied, furthermore, methods about the identification and classification of fog have been presented.

One of the earlier researches examined the annual frequency of days with heavy fog in the United States. *Peace* (1969) assessed that heavy fog (visibility is one-fourth mile or less – about 0.4 km) occurred over 20 days per year at 50 % of the main weather stations, and the frequency of heavy fog was found to be higher than in previous 30 years. The regions with largest frequency of heavy fog are located in the West Coast, Appalachian Mountains, and Atlantic and Gulf Coasts. The annual mean data were displayed by histograms and isopleth analysis (steep gradient was 10 days increment up to 100 days). *Hardwick* (1973) used an objective analysis by applying special computer program called SYMAP to create maps about the monthly and annual distribution of heavy fog days over the continental part of the United States. The author found similar result in case of the annual distribution of heavy fog than *Peace* did, but the isopleth analysis was proved to be a more precise tool than the computer analysis. The analysis accomplished by the latter method overestimated the relative frequency of the fog within New England and Washington State. The monthly data were plotted by maps for each month showed similar spatial distribution of fog than it was published by *Peace* (1969).

Meyer and Lala (1990) used term of fog events instead of foggy days to avoid multiple counting of the same fog event and to consider the changing characteristics of the fog (e.g., the formation and evolution of fog lasts not only one day). According to their result, the peak of the number of radiation fog events is in September and October at Albany, New York. During the studied period (1970–1979), radiation fog events were 71% of all fog events in this area.

The most reliable method to examine fog climatology is the combination of surface meteorological observation data and digital satellite images (*Bendix, 1994*). Using satellite data with high spatial resolution (1 km²) helps to avoid overestimation of fog frequency which can derive from the extrapolation of surface data. Data from NOAA-AVHRR were used in this study to determine areas covered by fog according to the image of temperature differences between channel 3 and 4 for day and night. The result of this study affirmed that the extension of fog is highly influenced by the weather condition and the airflow.

Shanyengana et al. (2002) published interesting results about fog climatology in Namibia. The frequency of fog was investigated in the Namib Desert to promote the utilization of fog water deposition. In this location, the coincidence of the peak of fog deposition and the high groundwater salinity is favorable to dilute saline groundwater for drinking purposes from August to February.

The temporal variation of fog was studied in mountainous areas as well. *Blas et al. (2002)* published analysis of data observed in Mt. Sznrenica, Poland. The results based on hourly observed data of 51 stations showed that the average number of annual foggy days was about 274. The longest foggy period lasted for 371 h, and very dense fog (visibility is equal or less than 100 m) occurred predominantly. Furthermore, the spatial variation of fog was examined in the Sudety (Poland). The result proved that the local geographical features (such as landform type, exposure of the windward side, etc.) could play more important role in the spatial variability of fog than the altitude.

About 50 years data from 12 airports were collected and analyzed with two-tailed t-test to determine the long term climatological changes of dense fog in the USA by *Witiw and Baars (2003)*. The results showed that the occurrence of dense fog decreased at 7 regions (Seattle–Tacoma, San Francisco, Los Angeles, Long Beach, La Guardia [New York], Baltimore–Washington International, and Washington Reagan), furthermore, an increase was reported in Boston, a slight increase was found at Denver, and not significant difference was found in the case of Minneapolis–St. Paul, Atlanta, and Dallas–Fort Worth during the studied period. In this study it was also reported, that the frequency of fog decreases in the cities in some country, e.g., in Canada, Brazil, Argentina, United Kingdom.

Further statistical methods have been applied to study the fog climatology. The effect of urban heat island, particulate pollution, and sea surface temperature were examined; how they could influence the occurrence of dense fog in Los Angeles (*LaDochy, 2005*). The results showed that the increase of the temperature

in the urban area and the improvement of air quality played important role in the reduction of the number of foggy days. However, it was also found that the Pacific Decadal Oscillation and El-Niño-Southern Oscillation impacted the interannual fog variability by the changing of coastal sea surface temperature.

The knowledge and dataset which have been retrieved from the study of fog climatology can be used to improve the forecast; e.g., new technology exists to plot frequencies of different meteorological conditions on SD-graphs (seasonal-diurnal) (Gultepe *et al.*, 2007). Martin (1972) utilized this method to examine the ceiling frequencies at different flight categories. The improvement of computer capacity, statistical analyses methods, and graphic user interface allowed the SD-graphs to be improved (Gultepe *et al.*, 2007). This technique was used by Fisk (2004) to display the fog formation frequency in London, Point Mugu, and St. John's, Newfoundland. It was also applied by Tardif and Rasmussen (2007) to provide detailed data about onset and dissipation of different fog types. In the latter study it was conceded, that the hourly observation data might be useful to identify fog events, and atmospheric conditions have been analyzed by a decision algorithm to deduce the formation of different fog types. The authors suggested determining the fog events on the base of regular observation data.

Scherrer and Appenzeller (2014) presented a long-term FLS-climatology (FLS: fog-low stratus) of the Swiss Plateau. The study based on daily relative sunshine duration measurements to create different categories for duration of FLS cases. These indicators (full FLS and at least half FLS days) were analyzed for three time periods (entire series, the foggiest and the least foggy decades). The results suggested that there were decadal and interannual variability of fog. However, significant long-term trend was not reported. Strong correlation was found between the numbers of cool air pools days and FLS data.

Evaluation of fog climatology of Japan based on statistical analysis of data about foggy days and fog events was presented by Akimoto and Kusaka (2015). They studied the relation between the visibility of fog and the surrounding geographical environment (topography and land use). The classification of fog events was based on the extent of horizontal visibility (fog, quasi-dense fog, and dense fog events). Long-term data series (from 1966 to 2005) were used to demonstrate long-term changes in the number of foggy days in Japan. The results indicated that most of the foggy days and the densely foggy regions could be observed on the inland mountainous areas, basins, and on the Pacific coast of Japan; furthermore, it was also found that the most common fog type was radiation fog. They also asserted that the number of foggy days decreased at most of observation sites in Japan during the studied period. Different trends for the number of foggy days were found in different regions of Japan. While in inland sites decreasing trend was reported, at some area located on coastal region the decreasing trend was not obvious. Furthermore, increasing trends were recorded at some locations (e.g., Miyako). No physical explanation was found for the diversity of the trends in the different geographical regions.

Satellites data has been affirmed to be useful for fog observation, because of their large temporal and spatial resolution. Therefore, surface observation can be completed with satellite observation about low clouds (*Avotniece et al.*, 2015). The fog is similar to low stratus cloud in many respects, the main difference between these phenomena is the altitude of ceiling (ceiling of fog is at the surface). Hence, the surface observation of fog can be compared to satellite data about low cloud. Atmospheric circulation patterns were also studied to find favorable atmospheric conditions for fog formation in Latvia. The results indicated that the high-pressure over the whole country was the most favorable criterion of fog formation. The trend about the number of foggy days has been descending in Latvia since the middle of the previous century.

Fog was found to depend on definite thresholds and regimes of meteorological variables (*Goswami and Sarkar*, 2015). To improve fog forecasting and modeling, they looked for relations between the meteorological variables (hourly temperature, dew point depression, wind, and relative humidity) and the formation of the fog. They asserted that the contrast between the meteorological variables characterizing the foggy and non-foggy days sometimes could be more significant at the 850 hPa level, than near-surface. They also suggested that the observation data from the surface should have been completed by satellite data to accomplish a comprehensive analysis of fog dynamic.

Cermak and Bendix (2008) also asserted that the data of surface observations at meteorological stations could not provide coherent overview about the distribution of fog/low stratus. Satellite data has been conceded to be useful to complement the incomplete data sets. In the earlier seventies the detection of fog by satellite was studied by *Hunt* (1973), who found that the small droplets (that fog contains) had smaller emissivity at the wavelength of 3.9 μm than at 10.8 μm . This dependence of the emissivity on the wavelength was negligible in case of larger droplets and cloud-free areas. As mentioned above, fog detection by satellites is usually based on the difference between the brightness temperatures observed at channels 3 and 4 of AVHRR (Advanced Very High Resolution Radiometer). The optical properties of fog droplets can be used to make distinction between the fog and the surface during both day and night. Using satellite data, *Bendix* (2002) investigated the frequency of fog occurrence in Germany and in adjacent areas. While the frequency of fog occurrence was found to be the largest at the Lake Constance area, it was much smaller over elevated terrains (e.g., Alps) and at the top of lower mountains (e.g., Vosges, Harz Mountain). New detection technology was worked out by *Bendix et al.* (2006) to improve the distinction between the fog and several cloud types. This method was called radiative transfer-based classification scheme. It was implemented into the Moderate Resolution Imaging Spectroradiometer (MODIS) gauge that was installed on board of Terra and Aqua platform as well. This method was not efficient enough to distinguish the fog from several other cloud types, if their optical properties were similar to those of fog. *Cermak and Bendix* (2008) developed a new fog/low stratus detection algorithm to

improve daytime detection of fog and low stratus from geostationary platforms. This scheme involves the sequence of spectral and spatial fog/low stratus property complementary tests.

Using satellite data, *Cermak et al.* (2009) published the fog and low stratus (FLS) climatology of Europe. The results showed that the frequency of FLS occurrence reduces from North toward South. This study based on satellite-derived maps of fog and low stratus. The applied method involves both the spectral and the spatial tests. These tests allow us to assess the characteristics of fog and its environment (Satellite-based Operational Fog Observation Scheme – SOFOS, *Cermak*, 2006). Ground-based observation data set and satellite data set were synchronized in this study. The satellite maps have larger spatial resolution, and as a consequence of this, several small-scale patterns can be detected only on the satellite-derived maps. Compared to surface observation data, the satellite data have higher temporal resolution as well. However, the satellites are not able to detect fog or low stratus if another opaque cloud layer is located above them, and similarly to the surface observation, satellites are not able to detect the fog patches with very small spatial extension (sub-pixel size). *Wang et al.* (2010) investigated the frequency of heavy fog in Beijing area using the indicator of fog frequency distribution intensity. This indicated the area weighted averages of foggy days based on data which were observed by some polar orbit meteorological satellites. The results showed that the southeastern, eastern, and central parts of Beijing were foggier than the western area.

Egli et al. (2017) evolved fog and low stratus climatology of Europe using geostationary satellite data. The FLS detection scheme (*Cermak and Bendix*, 2008) was improved by the moving-window technique, which allows us to avoid inaccuracies derived from changing of geographic location of pixels (illumination variation) and differences of surface types (shifts in spectral band differences). In addition, the discrimination between small and large droplets of clouds at daytime was improved by observations of the reflection of solar radiance at 3.9 μm . The results showed that the maximum values of FLS in units [h day^{-1}] occurred in winter months accompanied by the latitudinal gradient. Interannual trend of FLS-occurrence was also investigated by involving air temperature and wind speed. They found that frequency of fog showed decreasing trend mainly over Central Europe in winter months.

As it was mentioned previously, the fog has been studied in only few research programs in Hungary. *Antal and Péczely* (1956) investigated the cloud features in the case of different macrosynoptic situations over Hungary. The results of statistical analysis proved that from late autumn to early spring, the atmospheric conditions characterize the anticyclone promoted the formation of fog. Mainly the radiation and advection types of fog are frequent at this condition. *Lépp and Rajkay* (1957) dealt with horizontal visibility and cloud height data to improve the safety of aviation at several airports in Hungary. The data of two winter seasons indicated that data of visibility during the night was slightly smaller than during the day. To

increase the reliability of fog forecasting, *Antal* (1958) studied the climatology of fog at 11 meteorological stations (mainly at airports). Data observed during 11 years in winter seasons were analyzed. The author asserted, that the frequency of the fog was the highest in December, furthermore, the comparison of fog frequency at different locations showed that the frequency of fog was the smallest in Győr, and it was the largest in Budapest and Miskolc. Fog cases with different macrosynoptic situations and different duration were studied. It was found that in October and March, the most favorable macrosynoptic condition of the occurrence of fog is the cyclonic warm or occluded front. In the other months, the high pressure center of anticyclones or the presence of divergences zone can contribute to the formation of fog, which can last all day. The frequency of the short term fog was found to be significantly higher than that of the long term fog. The predominance of the short term fog stems from the fact that the radiation fog – which is the most typical form of fog in Hungary – generally disappears shortly after the sunrise. *Kéri* (1965) studied the characteristics of fog in urban regions by comparing the data which were observed in Budapest and Kalocsa. The analysis of observed data (from 1901 to 1960) revealed that at the start of the period, the number of foggy days was 48 in Budapest, and it increased by about 10 % by the end of the investigated period. The contrast between the urban and rural areas was established by the fact, that in the Budapest region, the number of foggy days was 8 days larger than in the country sides. *Probáld* (1965) also investigated the urban effect on the visibility related to the air pollution. The author analyzed the annual trend of the visibility and the relation between the fog and wind direction. The conclusion of the research was that the horizontal visibility in Budapest depends on the wind direction, because the transport of the air pollution was sensitive to that. *Wantuch* (2001) proposed a nowcasting method for forecast fog formation and visibility. The author evolved the fog stability index (FOGSI) and fog decision tree method, which involved observed data and derived physical parameters. The atmospheric conditions have been classified into normal and cold air pool categories. The classification was based on the observed humidity, wind speed, and radiative cooling. *Tuba* and *Bottyán* (2018) suggested a more reliable method to forecast the horizontal visibility focusing on airports in Hungary. The authors developed a new hybrid forecast model based on combining fuzzy logic-based analogue and output of numerical forecasts.

In the current study, we focus on the statistical analysis of long-term data series of reduced visibility in Hungary. We investigate: (i) the duration and frequency of fog and mist over the last six decades; (ii) the occurrence and characteristics of fog in different regions in Hungary; (iii) the relation between the air pollution and the frequency of fog.

The data and methods applied in this study are described in Section 2. The results will be published in Section 3, and finally, the last section involves the conclusions and outlook.

2. Data and methods

Data about reduced visibility for the period of 1956–2017 have been collected from 8 meteorological synoptic weather stations (see *Fig. 1*). These stations were chosen, because data series for this long period are available at these locations. The observation frequency was 3 hours between 1956 and 2017. This study is mostly based on the evaluation of fog events instead of foggy days to give a more accurate description of fog frequency. The raw data of reduced visibility have been distributed into 5 categories according to the spatial extent of horizontal visibility (mist; and four visibility categories for fog: 1000–700 m, 700–500 m, 500–300 m, <300 m). To reduce the uncertainty caused by the inaccuracy of observed visibility, these categories were regrouped into 3 categories: mist, fog (1000 m–300 m), and dense fog (less than 300 m). Because the reported time period of mist and that of fog generally included the duration of fog and dense fog, the raw data needed some preprocessing to avoid overestimation of the duration of mist and fog periods. Foggy and mist events duration of which were reported longer than 240 hours were rejected.

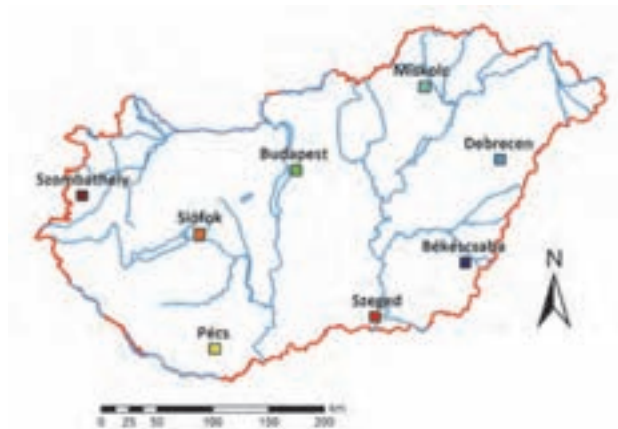


Fig. 1. The current locations of meteorological stations where data about mist and fog were observed.

Locations of the meteorological observation stations where data have been observed are plotted in *Fig. 1*. The relocation of few stations (see *Table 1*) may cause some inhomogeneity in the database. Besides the operating dates of the stations, the elevation and the type of the landform of station locations are summarized in *Table 1*. Most of the stations (except Siófok and Budapest) were moved during the past decades from one location to another; however, significant

change occurred only in the case of the station in Miskolc. During the first decades of the studied period (until 1990), the observations were taken at the airport nearby to Miskolc on 118 m ASL. In 1990, the meteorological station was moved into the city area with elevation of 231 m ASL. The station was moved further in 1997. Although it stayed in the city area, the elevation of the new position was 231.8 m ASL. The last relocation of the station occurred in 2013, and it is currently operated in Diósgyőr at elevation of 161 m. The station of Békéscsaba was also replaced many times in the past decades. The observation was taken in the suburb area of the city except between 1947–1964 and 2002–2010. Stations of Szombathely, Pécs, Szeged, and Debrecen are located in the surrounding area of the cities, furthermore, the station in Siófok is located on the shore of Lake Balaton. The station in Budapest is at the edge of a suburb area of the city.

Table 1. The location of the stations over the period from 1950s to present days

Designation of the meteorological observation stations	Location (and elevation) of the stations from the 1950s to 1990	Location (and elevation) of the stations from 1990 to nowadays
Budapest	06.15. 1953.: <u>Budapest-Pestszentlőrinc (138.1 m) (plain)</u>	<u>Budapest-Pestszentlőrinc (same before 1990.)</u>
Békéscsaba	09.01.1947.–02.29.1964.: Kazinczy str. (87 m) and 06.01.1951.–07.31.1957.: Airport (84 m) 06.01.1961.–06.27.1985.: Fényes (87 m) 06.28.1985.–06.30.1994.: Nagyréti (Ionosphere Research Observatory) (84,5 m)	07.01.1994.–12.05.2002.: Airport 2. (86.1 m) 10.09.2002.–11.05.2010.: Waterworks (85.2 m) 10.29.2010.: <u>Békés Airport (86.8 m)</u> (all of the locations: plain)
Debrecen	01.01.1950.–04.19.1960.: Airport (110 m) 04.20. 1960.–07.31.1995.: Airport (104 m)	08.01.1995.– <u>Airport</u> (Mikepércsi str.) (106.6 m) (all of the locations: plain)
Miskolc (the station is inside in the city)	08.01.1950.–06.01.1990.: Airport (118 m) (plain)	06.02.1990.–06.24.1997.: Avás (231 m) (hilltop area) 06.24.1997.–06.27.2013.: Avás (231.8 m) (hilltop area) 06.27.2013.– <u>Diósgyőr: Fire-fighter barrack (161 m) (valley area)</u>
Pécs	02.19.1946.–03.31.1957.: Uránváros – Airport (124 m) (plain) 06.02.1956.–03.03.1969.: Pogány Airport (Harkányi str.) (201 m) 03.04.1969.–03.24.1998.: Pogány Airport (near the airport building) (206 m)	03.24.1998.–03.31.2004.: Pogány Airport (Harkányi str.) (201.8 m) 03.31.2004.– <u>Pogány Airport (199.2 m)</u> (all of the locations: hilly area)
Siófok	1956.– <u>on the shore of Lake Balaton (108 m) (plain)</u>	<u>on the shore of Lake Balaton (same before 1990.)</u>
Szeged	01.01.1951.–07.31.1965.: Airport (82 m) 08.01.1965.–05.05.2004.: Airport (Radiosounding Observatory) (81 m)	05.05.2004.: <u>Airport (80.8 m)</u> (all of the locations: plain)
Szombathely	01.01.1950.–12.31.1964.: Airport (224 m) 01.01.1965.–04.24.2002.: Airport (220 m)	02.27.2002.– <u>Komárom str. (200.1 m)</u> (all of the locations: hilly area)

Format of the date: mm.dd.yyyy.

3. Results

The duration and frequency of reduced visibility categories have been analyzed to investigate their time series during the last six decades in Hungary.

The frequencies of durations for three types of reduced visibility were plotted by histograms. The frequency categories were determined by intervals of 10 hours (except the first interval, where boundaries are 3 and 9 hours). The results show the frequency of events with different lifetimes in the different visibility categories at different cities, which characterize the different regions in Hungary. The columns with different colors represent the data related to different cities (see *Fig. 1*). The categories on the x axis are the intervals for duration.

The year-to-year variation of the seasonally summarized (from October to March – winter half-year) durations of different types of reduced visibility events are also plotted and analyzed. The strong fluctuations of the data were smoothed by using moving average. Data have been depicted on some graphs, the spots represent the seasonally summarized durations of each types of events, the solid lines reveal the 10 years moving average. The application of moving average method allows us to calculate the mean values of consecutive 10 years from data base and to emphasize the long-term trends by smoothing of the year-to-year fluctuations.

3.1. Analysis of data

3.1.1. Mist (horizontal visibility is between 5000 m – 1000 m)

The distribution of durations of mist events can be seen in *Fig. 2*. The number of events decreases nearly exponentially as the duration increases. Most of the events are included in the shortest duration category (3 – 9 hour). While in the shortest duration category the largest number of the events was observed at Szeged, from the third category (duration is longer than 20 hours) the largest number of the events was reported at Miskolc. Note, also, that in the first two duration categories, the smallest numbers of events were observed in Pécs and Siófok. While the largest numbers of events in the second category are related to Békéscsaba and Szombathely, from the third category the largest numbers of events were observed in the northeast part of the Hungary (Miskolc and Debrecen). This may stem from the fact that while the formation of mist (or fog) with shorter lifetime can be related or partly related to local conditions, the formation of mist with longer lifetime is mostly the consequence of macroscale processes.

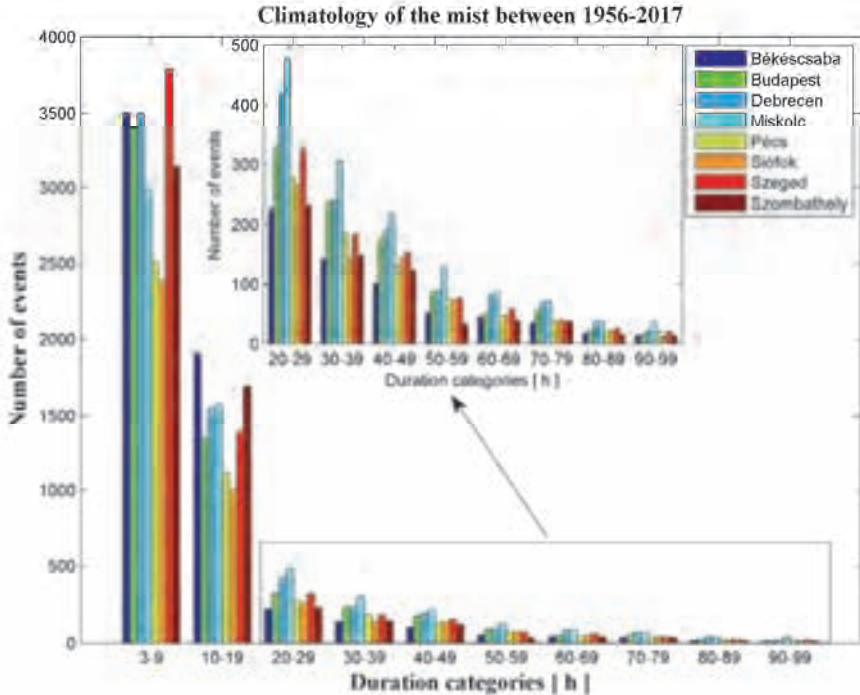


Fig. 2. The distribution of the duration of mist events at different cities. The different colors represent the data related to different cities (see Fig. 1). The categories on the x axis are the intervals for the duration of mist.

The seasonally summarized durations of mist events at the different cities, furthermore, the moving averages have been depicted in Fig. 3. At most of the stations, the seasonally summarized duration reached its maximum values between 1980 and 1990. However, due to the strong year-to-year oscillation, the duration of the mist changed between 1000 and 2000 hours at most of the stations before the 90s. The maximum values at the northeastern part of Hungary (Debrecen Fig. 3(c) and Miskolc Fig. 3(d)) were about 50% larger than in the other regions. If the values after 2000 are compared, no significant difference can be noticed between the regions, the seasonally summarized durations have been between 500 and 1000 hours. Trends of the moving average show decreasing tendency after the 80s at each station. The seasonally summarized durations of the mist significantly decreased everywhere in the country between the 80s and the early years of 2000. The steepness of the decrease changes between factor of two (Szeged Fig. 3(g)) and factor of five

(Debrecen Fig. 3.(c)). After 2000, the trend lines show that the seasonally summarized durations of the mist remain near constant. Before the 80s, the trends show rather distinct characteristics at the different cities. While in Szeged (Fig. 3(g)) the seasonally summarized durations of the mist were nearly constant, in one group of the cities (Budapest Fig. 3(b), Miskolc Fig. 3(d), and Pécs Fig. 3(e)), a steep increase occurred before the 60s, and in the other group of the cities (Békéscsaba Fig. 3.(a), Debrecen Fig. 3(c), and Siófok Fig. 3.(f)), a gradual increase of the duration can be observed.

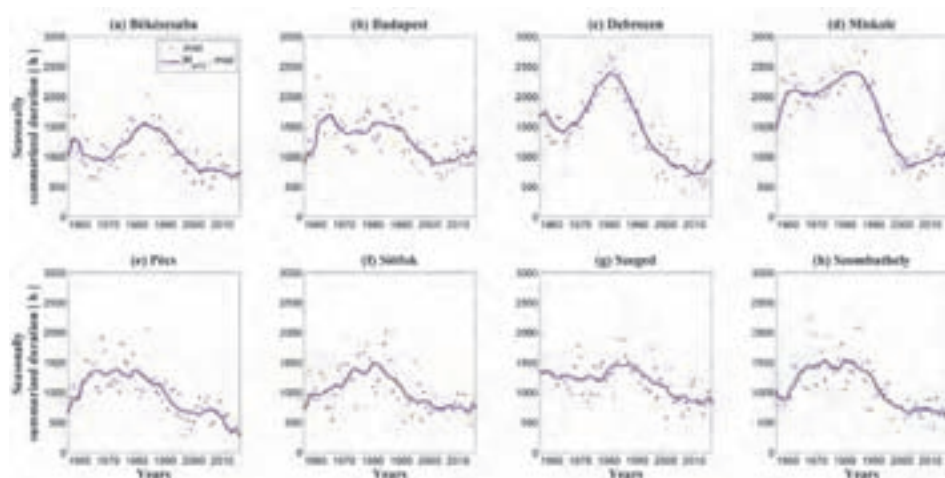


Fig. 3. Variation of the seasonally summarized durations of mist events (blue dots mean seasonally summarized duration of mist events) and the 10 years moving averages (blue solid lines) for all stations between 1956 and 2017.

3.1.2. Fog (horizontal visibility is between 1000 m – 300 m) and dense fog (horizontal visibility is less than 300 m)

The distribution of durations of fog and dense fog events are shown in Figs. 4 and 5, respectively. Similarly to mist, the number of events exponentially decreases as the duration increases. The largest number of events for both fog and dense fog cases were reported at Miskolc in each duration category. In these cases, contrary to the mist events, the number of events has been significantly larger (two or three times) at Miskolc in each duration category than at any other cities. This significant difference between Miskolc and the group of other cities can be explained by the unique environmental conditions characterizing the

meteorological station in Miskolc. Although the station was outside of the city until the 90s, the high level of industrial pollution must have promoted the fog (smoke) formation. Note that at Miskolc and Debrecen, in the last four duration categories, more dense fog events were reported than fog events (compare *Fig. 4* to *Fig. 5*). It means that if the lifetime of the fog is large enough, the chance of the formation of dense fog is relatively large in this region of the country.

Comparison of the histograms of fog (*Fig. 4*) and that of mist (*Fig. 2*) shows that while in the first duration category (3–9 hours), the number of fog events is similar to that of mist events at each station, in the cases of longer duration categories, the differences are more significant. This suggests that the mist-fog transition is more frequent if the lifetime of these events is relatively short.

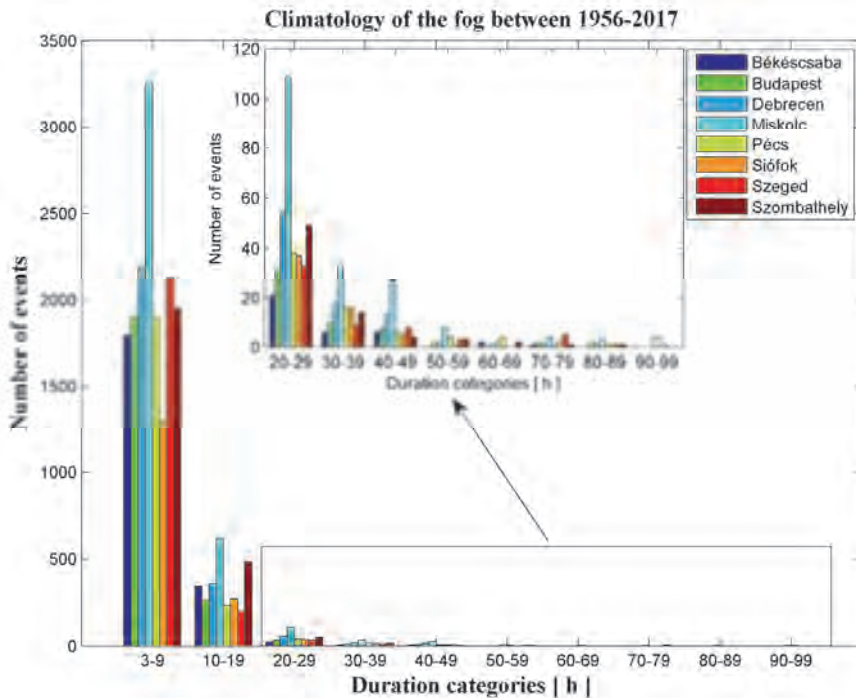


Fig. 4. The distribution of the duration of fog events at different cities. The different colors represent the data related to different cities (see *Fig. 1*). The categories on the x axis are the intervals for the duration of fog.

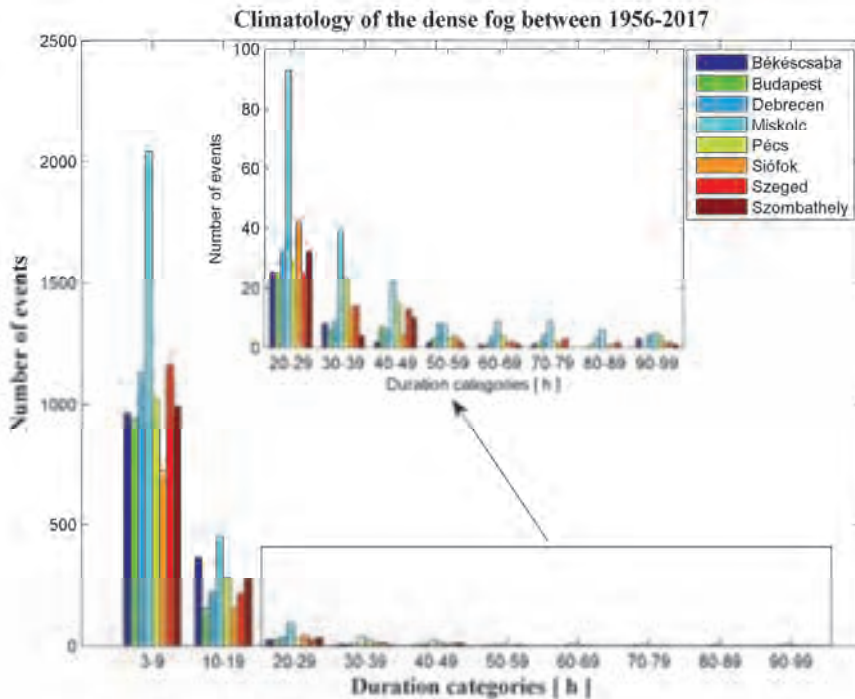


Fig. 5. The distribution of the duration of dense fog events at different cities. The different colors represent the data related to different cities (see Fig. 1). The categories on the x axis are the intervals for the duration of dense fog.

The variations of the seasonally summarized durations of fog events at different cities are plotted in Fig. 6. The trends of the duration of fog events are more diverse than in the case of the mist. While at some of the stations (Békéscsaba Fig. 6(a), Budapest Fig. 6(b), Pécs Fig. 6(e), and Siófok Fig. 6(f)), the duration of fog remained near constant after the 80s, at another group of the stations (Debrecen Fig. 6(c), Miskolc Fig. 6(d) and Szeged Fig. 6(g)) significant reduction of the duration occurred. Unlike other regions in the country, a slight increase of duration occurred by the early 2000s at Szombathely (Fig. 6(h)). Note, that while the length of the mist periods was near the same at Miskolc (Fig. 3(d)) and Debrecen (Fig. 3(c)) in the 80s, the duration of fog was significantly smaller in Debrecen (Fig. 6(c)) than in Miskolc (Fig. 6(d)).

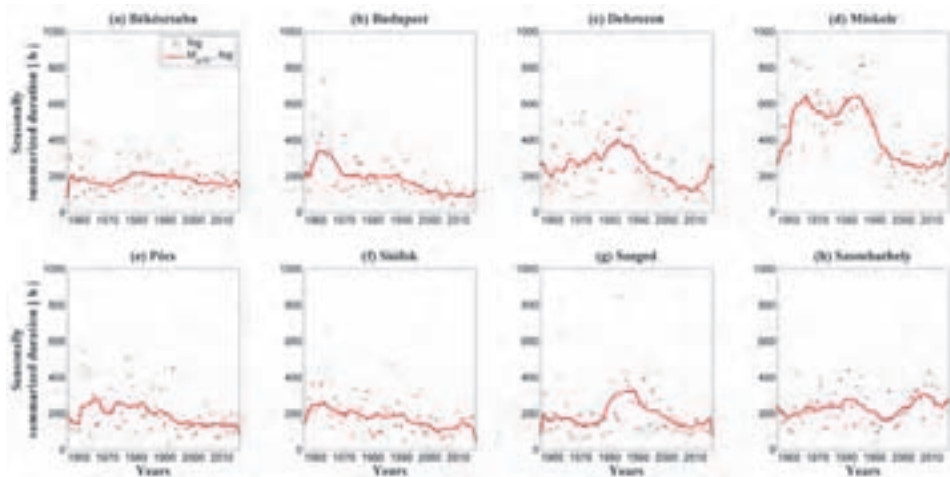


Fig. 6. Variation of the seasonally summarized durations of fog events (red dots represent seasonally summarized duration of fog events) and the 10 years moving averages (red solid lines) for all stations between 1956 and 2017.

Before the 90s of the last century, the seasonal duration of the dense fog was less than 400 hours except for few years and expect for Miskolc (Fig. 7). Similarly to the mist and fog in this time period, the longest seasonally summarized durations were reported at Miskolc (Fig. 7(d)). This is the only city, where the duration of dense fog has significantly decreased after the 80s. Due to the industrial emission, the air pollution in Miskolc was very high in the middle decades of the 20th century. From end of the 1980s, the pollution caused by this type of emission was significantly reduced (Kukely and Zábrádi, 2003), that might have contributed to the improvement of the air quality and to the reduction of the frequency of the fog and mist.

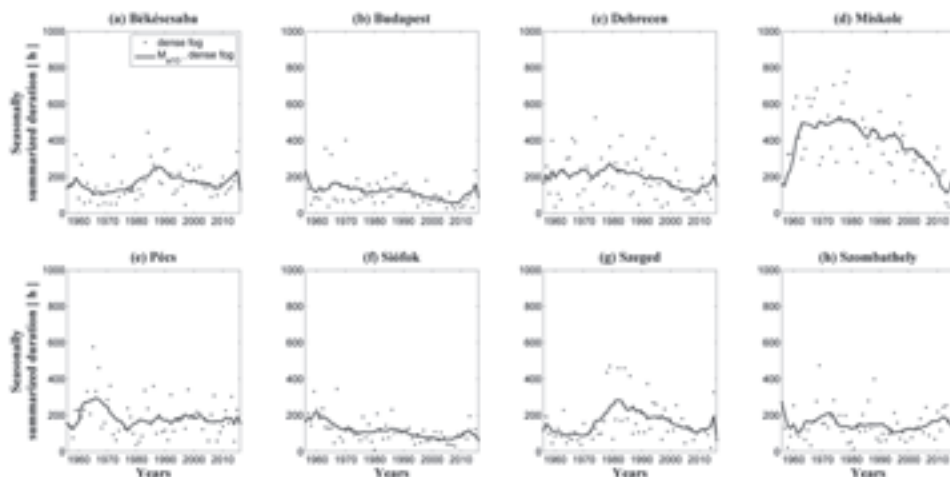


Fig. 7. Variation of the seasonally summarized durations of dense fog events (black dots visualize the seasonally summarized duration of dense fog events) and the 10 years moving averages (black solid lines) for all stations between 1956 and 2017.

3.2. Analysis of the relation between wind and reduced visibility based on climatological data

Wind has a strong impact on the evolution of the fog. The turbulence enhanced by the wind can mitigate the fog formation or destroy the fog by reducing the vapor content near to the surface (Cotton and Anthes, 1989). However, sometimes the turbulence can promote the fog formation by lowering the stratus clouds (Cotton and Anthes, 1989). Because currently only the daily climatological data are available for the wind, the detailed discussion about the relation between the fog and wind speed is not possible. The statistical characteristics of the wind speed related to different types of reduced visibility categories and to high visibility (visibility is larger than 5 km) are summarized in Table 2. The average daily values of wind speed measured at 10 m above the surface were retrieved from the CARPATCLIM database (Szalai et al., 2013) covering the period from 1961 to 2010. In the line with the previously mentioned assumption, the mean, median, and mode of the distributions are significantly smaller in the case of the reduced visibility than in the case of the high visibility (Table 2). The smaller values of the standard deviation in the case of the reduced visibility (Table 2) mean lower frequency of the wind speeds above the value of 5 m s^{-1} (Fig. 8). The distributions of the wind speed in

different cases for Debrecen (a), Miskolc (b), Pécs (c), and Siófok (d) are plotted in Fig. 8. The shapes of the distributions suggest that the wind speed shows gamma distribution (Fig. 8). The smaller value of the skewness parameter in the case of the high visibility also means the higher frequency of the larger wind speed (Table 2).

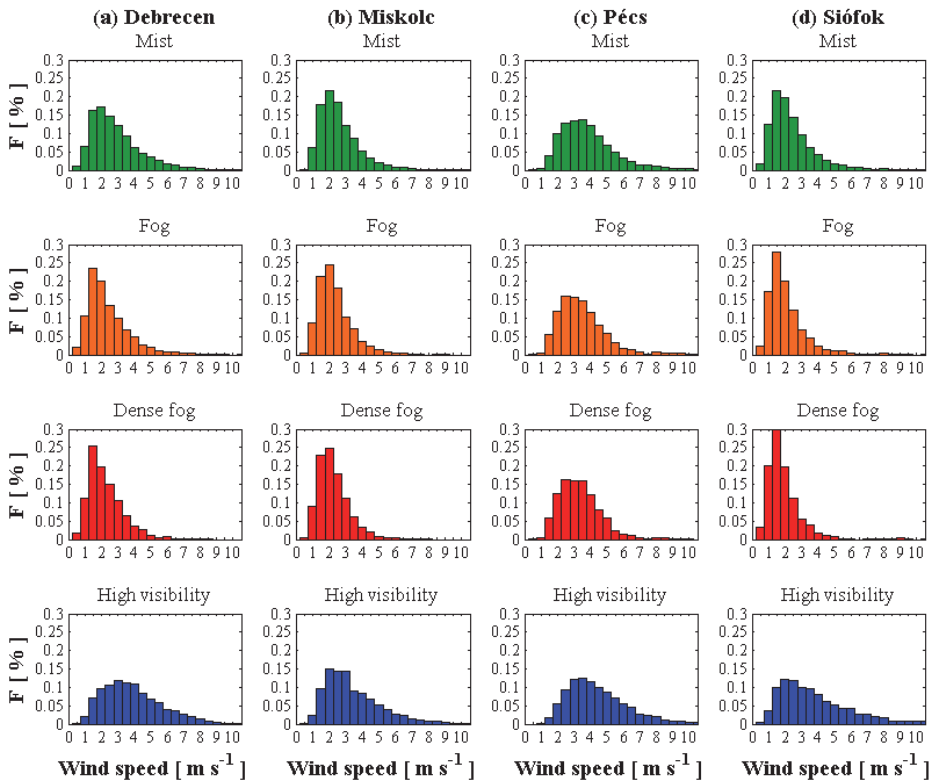


Fig. 8. Distribution of the wind speed at 10 m elevation Pécs level in case of different horizontal visibility at different stations ((a): Debrecen, (b): Miskolc, (c): Pécs, and (d): Siófok)). Values of „F” denote frequency of wind speed for each wind speed interval.

Analysis of the wind speed data related to mist, fog, dense fog events and high visibility suggested an assumption about the difference of the wind speed related to different cases. The assumption declared that the wind speeds were different during the days related to reduced visibility events and to high visibility. Wind speed data of Budapest (form 1961 to 2010) were investigated

by chi-squared probe to demonstrate or reject this assumption. The distribution of daily wind speed was analyzed between high visibility and mist events; between mist and fog events, and between fog and dense fog events. The results of the test showed that the null-hypothesis (there is no difference between the distributions of the wind speed between foggy days and related to high visibility) can be rejected even at significance level of 0.01.

Table 2. Statistical characteristics of the wind speed for all of the stations. The table contains values about all types of reduced visibility and high visibility (visibility is larger than 5000 m). (Data from: CARPATCLIM database, *Szalai et al.*, 2013)

Mist	Békéscsaba	Budapest	Debrecen	Miskolc	Pécs	Siófok	Szeged	Szombathely
Min (ms ⁻¹)	0.24	0.22	0.05	0.32	0.48	0.18	0.2	0.3
Max (ms ⁻¹)	15.22	11.48	14.4	11.95	16.3	13.41	14.82	17.41
Mean (ms ⁻¹)	2.8	2.32	2.68	2.36	3.64	2.25	2.7	2.8
Deviation	1.57	1.3	1.61	1.22	1.74	1.57	1.31	1.8
Median (ms ⁻¹)	2.44	1.99	2.27	2.1	3.33	1.83	2.46	2.35
Mode (ms ⁻¹)	1.63	1.49	1.42	1.61	3.03	1.3	2.26	1.97
Skewness	1.56	1.95	1.61	1.69	1.41	2.43	1.5	2.33

Fog	Békéscsaba	Budapest	Debrecen	Miskolc	Pécs	Siófok	Szeged	Szombathely
Min (ms ⁻¹)	0.28	0.23	0.07	0.32	0.48	0.18	0.2	0.35
Max (ms ⁻¹)	15.22	10.24	14.4	12.21	12.29	10.06	14.82	14.6
Mean (ms ⁻¹)	2.34	2	2.2	2.13	3.26	1.91	2.42	2.58
Deviation	1.38	1.13	1.43	1.12	1.48	1.33	1.29	1.79
Median (ms ⁻¹)	2.04	1.76	1.83	1.88	3.02	1.55	2.16	2.13
Mode (ms ⁻¹)	1.48	1.24	1.42	1.76	2.17	1.19	1.49	1.97
Skewness	2.09	2.44	2.35	2.19	1.47	2.43	2.07	2.77

Dense fog	Békéscsaba	Budapest	Debrecen	Miskolc	Pécs	Siófok	Szeged	Szombathely
Min (ms ⁻¹)	0.29	0.23	0.07	0.32	0.48	0.18	0.2	0.41
Max (ms ⁻¹)	9.07	10.24	11.64	7.82	12.29	11.21	14.82	14.6
Mean (ms ⁻¹)	2.17	1.85	2.04	2.03	3.13	1.74	2.19	2.46
Deviation	1.16	0.98	1.15	0.96	1.33	1.26	1.08	1.68
Median (ms ⁻¹)	1.89	1.65	1.78	1.83	2.97	1.44	1.99	2.05
Mode (ms ⁻¹)	1.26	1.59	1.42	1.76	2.84	1.44	1.49	1.97
Skewness	1.40	2.52	1.82	1.41	1.42	3.20	2.48	2.98

High visibility	Békéscsaba	Budapest	Debrecen	Miskolc	Pécs	Siófok	Szeged	Szombathely
Min (m s ⁻¹)	0.24	0.2	0.1	0.25	0.65	0.28	0.42	0.25
Max (m s ⁻¹)	14.56	14.09	13.01	15.62	14.22	15.37	12.64	20.09
Mean (m s ⁻¹)	4.07	3.28	3.69	3.23	4.21	3.65	3.82	3.72
Deviation	1.96	1.85	1.87	1.8	1.87	2.29	1.72	2.22
Median (m s ⁻¹)	3.82	2.82	3.38	2.79	3.86	3.1	3.56	3.12
Mode (m s ⁻¹)	3.81	1.55	2.82	2.54	2.39	1.99	2.55	2.15
Skewness	0.95	1.28	0.94	1.41	1.07	1.33	0.99	1.63

3.3. Frequency of the occurrence of the reduced visibility events

Fig. 9 shows the daily distribution of the different types of reduced visibility for the period from October 1956 to March 2017. The relative frequency of the mist, fog, and dense fog reports are plotted in *Fig. 9(a)*, *(b)*, and *(c)*, respectively. In each case the relative frequency has its maximum at 6 am. This means that most of the reports about reduced visibility were issued at 6 UTC. A secondary maximum in the case of mist can be found at 18 UTC (*Fig. 9(a)*). This stems from the fact, the radiative cooling is the strongest near to the sunrise, and in the winter season the temperature can decrease significantly after the sunset. The strong reduction of the temperature increases the relative humidity near to 100% (see *Geresdi*, 2004). The relation between the radiation and the relative humidity explains why the numbers of reports have their minimum values at noon and early afternoon. Compared to the mist (*Fig. 9(a)*), the number of the fog reports (*Fig. 9(b)*) and especially that of the dense fog reports (*Fig. 9(c)*) are relatively high in the second half of the night (between midnight and 6 UTC). The consecutive secondary maximums of the mist and that of fog and dense fog suggest that the midnight fog has frequently evolved from the mist formed late afternoon or evening due to the radiative cooling. The high frequency of the fog in the morning (before 6 or 9 UTC) and the increase of the fog frequency next to the secondary maximum of the mist frequency at 18 UTC suggest that radiation fog is the most common type of fog in Hungary. (Unfortunately, no direct information is available to make distinction between the different types of fogs formed in Hungary.)

The reports were also categorized on the base of the month they were issued (*Fig. 10*). This type of plots shows less sensitivity to the location of stations. The monthly distribution of the reduced visibility is almost the same in each region of the country. However, the monthly distribution of the mist (*Fig. 10(a)*) is rather different to that of the fog (*Fig. 10(b)*) and dense fog (*Fig. 10(c)*). While the monthly distribution of the mist is rather uniform in the investigated season (from October to March), the monthly distribution of the fog and that of the dense fog have a significant maximum in December/January. That is the ratio of the maximum and minimum frequencies is about 1.5 in the case of the mist, and this ratio is 4–5 in the case of fog and dense fog. Near half of the fog events occur in December and January, and just 5% of the events can be observed in March.

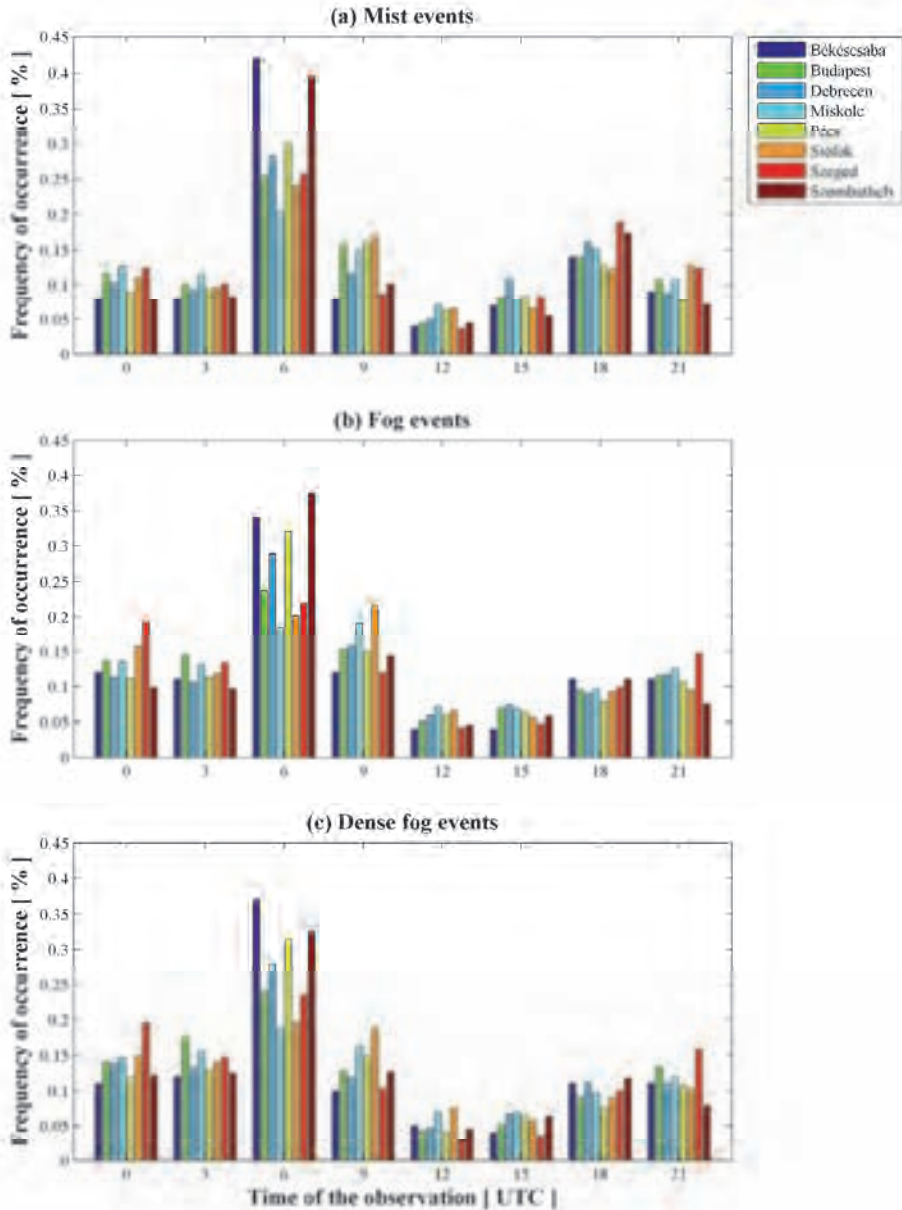


Fig. 9. Frequency of reports issued for mist, fog, and dense fog for three hours intervals for the period from October in 1956 to March in 2017. E.g., 0 means that the report was issued between midnight and 3 UTC, etc. The different colors represent the data related to different cities (see Fig. 1).

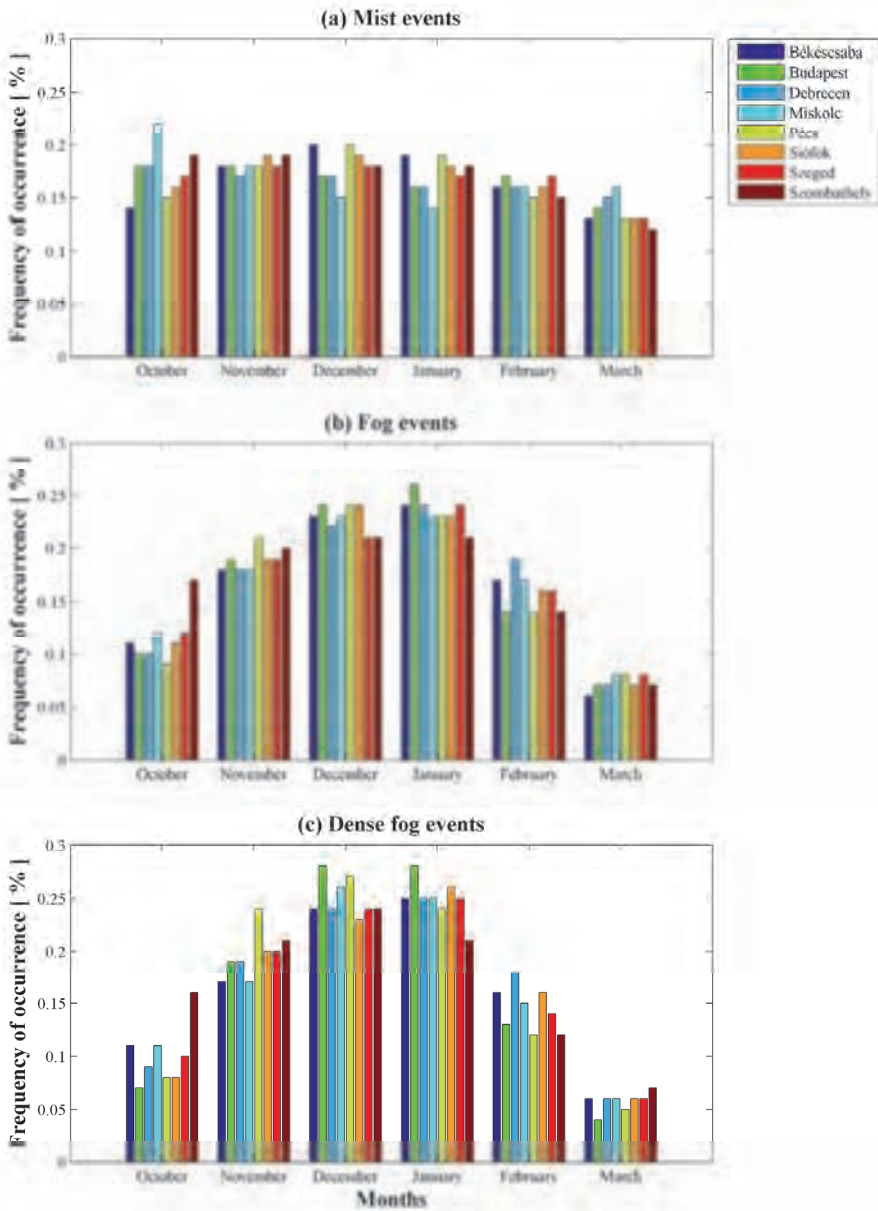


Fig. 10. Monthly frequency of occurrence of events related to different reduced visibility categories at different cities. The different colors represent the data related to different cities (see Fig. 1).

4. Conclusions

The fog climatology in Hungary has been compiled. The sources of the data were surface observations at eight meteorological stations in different regions of the country. The number of events, the seasonally summarized durations and frequency of reduced horizontal visibility events were evaluated. The results show that (i) the most reduced horizontal visibility events were reported from Miskolc and the least were observed at Siófok; (ii) the seasonally summarized duration of mist events decreased significantly in the last two decades of the previous century in Hungary with the largest steepness in the northeastern part of the country (see in *Fig. 3* at Debrecen (c) and Miskolc (d)); (iii) the number of events (mist, fog, and dense fog) exponentially decreases as the duration increases (see *Figs. 2, 4, and 5*); (iv) most of the reports about fog have been issued at 6 UTC (see *Fig. 9.(b)*), this fact indirectly supports the idea that the most fog and mist events occurred due to the radiative cooling in Hungary; (v) while the monthly distribution of the mist (see *Fig. 10(a)*) follows uniform distribution, the monthly distribution of fog (see *Fig. 10(b)*) and that of dense fog (*Fig. 10(c)*) follow normal distribution with maximum in December and January.

Analyses of the climatological data about the wind support the well-known fact, that low wind speed is necessary for the fog formation, because the absence of the vertical mixing between the polluted air mass near the surface and the cleaner air above promote the fog formation. However, in some cases, the strong turbulence caused by the larger wind speed can result in fog formation by lowering the stratus clouds (*Cotton and Anthes, 1989*). Analysis of the wind data suggests that this type of fog is rare in Hungary.

Some authors investigated the impact of the decreasing concentration of the sulfate emission in the last decades in the previous century in Hungary (e.g., *Havasi et al., 2001* and *Geresdi et al., 2006*). It was found that the reduced emission of SO₂ significantly resulted in a decrease of the number concentration of water drops in stratocumulus clouds. Both the theoretical consideration and coincidence of reduction of industrial air pollution and decrease of the frequency of mist and fog events suggest that the decrease of the SO₂ amount in the atmosphere mitigate the mist and fog formation. This hypothesis is supported by our finding that the most dramatic decrease of the reports about the mist and fog events occurred in the northeastern region of Hungary (at Miskolc and at Debrecen), where the air pollution was rather significant.

Acknowledgements: The present study was supported by Economic development and innovation operational program (project number: GINOP 2.3.2-15-2016-00055). The authors are indebted to the Hungarian Meteorological Service for data utilized this study.

References

- Akimoto, Y. and Kusaka, H., 2015: A climatological study of fog in Japan based on event data. *Atmos. Res.* 151, 200–211. <https://doi.org/10.1016/j.atmosres.2014.04.003>
- Antal, E., 1958: A köd gyakorisága és tartama a különböző makroszinoptikus helyzetekben. *Időjárás* 62, 39–45. (In Hungarian)
- Antal, E. and Péczely, Gy., 1956: Adalékok Magyarország makroszinoptikus helyzeteinek felhőzeti viszonyaihoz. *Időjárás* 60, 277–286. (In Hungarian)
- Avotniece, Z., Klavins, M., and Lizuma, L., 2015: Fog climatology in Latvia. *Theor. Appl. Climatol.* 122, 97–109. <https://doi.org/10.1007/s00704-014-1270-4>
- Bendix, J., 1994: Fog climatology of the Po Valley. *Riv Meteorol Aeronaut. V. LIV*, 25–36.
- Bendix, J., 2002: A satellite-based climatology of fog and low-level stratus in Germany and adjacent areas. *Atmos. Res.* 64, 3–18. [https://doi.org/10.1016/S0169-8095\(02\)00075-3](https://doi.org/10.1016/S0169-8095(02)00075-3)
- Bendix, J., Thies, B., Nauß, T., and Cermak, J., 2006: A feasibility study of daytime fog and low stratus detection with TERRA/AQUA-MODIS over land. *Meteorol. Appl.* 13, 111–125. <https://doi.org/10.1017/S1350482706002180>
- Blas, M., Sobik, M., Quiel, F., and Netzel, P., 2002: Temporal and spatial variations of fog in the Western Subety Mts., Poland. *Atmos. Res.* 64, 19–28. [https://doi.org/10.1016/S0169-8095\(02\)00076-5](https://doi.org/10.1016/S0169-8095(02)00076-5)
- Cermak, J., 2006: SOFOS - A new Satellite-based Operational Fog Observation Scheme. Dissertation zur Erlangung des Doktorgrades der Naturwissenschaften dem Fachbereich Geographie der Philipps-Universität Marburg. (In German)
- Cermak, J. and Bendix, J., 2008: A novel approach to fog/low stratus detection using Meteosat 8 data. *Atmos. Res.* 87, 279–292. <https://doi.org/10.1016/j.atmosres.2007.11.009>
- Cermak, J., Eastman, R.M., Bendix, J., and Warren, S.G., 2009: European climatology of fog and low stratus based on geostationary satellite observations. *Q. J. Royal Meteorol. Soc.* 135, 2125–2130. <https://doi.org/10.1002/qj.503>
- Cotton, W.R. and Anthes, R.A., 1989: Storm and Cloud Dynamic. Academic Press, San Diego.
- Egli, S., Thies, B., Drönner, J., Cermak, J., and Bendix, J., 2017: A 10 year fog and low stratus climatology for Europe based on Meteosat Second Generation data. *Q. J. Royal Meteorol. Soc.* 143, 530–541. <https://doi.org/10.1002/qj.2941>
- Fisk, C.J., 2004: Two-Way (Hour-Month) Time-Section Plots as a Tool For Climatological Visualization and Summarization, 14th Conf. Appl. Climatology, Am. Meteor. Soc. 11–15 January 2004, Seattle, Washington.
- Geresdi, I., 2004: Felhőfizika. Dialóg Campus Press, Budapest-Pécs. (In Hungarian)
- Geresdi, I., Mészáros, E., and Molnár, A., 2006: The effect of chemical composition and size distribution of aerosol particles on droplet formation and albedo of stratocumulus clouds. *Atmos. Environ.* 40, 1845–1855. <https://doi.org/10.1016/j.atmosenv.2005.11.012>
- Goswami, P. and Sarkar, S., 2015: Analysis and quantification of contrasts in observed meteorological fields for foggy and non-foggy days. *Meteorol. Atmos. Phys.* 127, 605–623. <https://doi.org/10.1007/s00703-015-0384-2>
- Gultepe, I., Tardif, R., Michaelides, S.C., Cermak, J., Bott, A., Bendix, J., Müller, M.D., Pagowski, M., Hansen, B., Ellrod, G., Jacobs, W., Toth, G., and Cober, S.G., 2007: Fog Research: A Review of Past Achievements and Future Perspectives. *Pure Appl. Geophys.* 164, 1121–1159. <https://doi.org/10.1007/s00024-007-0211-x>
- Hardwick, W.C., 1973: Monthly Fog Frequency in the continental United States. *Mon. Weather Rev.* 101, 763–766. [https://doi.org/10.1175/1520-0493\(1973\)101<0763:MFFITC>2.3.CO;2](https://doi.org/10.1175/1520-0493(1973)101<0763:MFFITC>2.3.CO;2)
- Havasi, Á., Bozó, L., and Zlatev, Z., 2001: Model simulation on the transboundary contribution to the atmospheric sulfur concentration and deposition in Hungary. *Időjárás* 105, 135–144.
- Hunt, G.E., 1973: Radiative properties of terrestrial clouds at visible and infra-red thermal window wavelengths. *Q. J. Roy. Meteorol. Soc.* 99, 346–369. <https://doi.org/10.1002/qj.49709942013>
- Kéri, M., 1965: A nagyvárosi jelleg tükröződése Budapest ködviszonyaiban. *Időjárás* 69, 265–270. (In Hungarian)
- Kukely, Gy. and Zábrádi, Zs., 2003: Az ipar szerepe vidéki nagyvárosaink rendszerváltozás utáni fejlődésében. Magyar Tudományos Művek Tára (In Hungarian).

- LaDochy, S., 2005: The disappearance of dense fog in Los Angeles: Another urban impact? *Phys. Geogr.* 26(3), 177–191. <https://doi.org/10.2747/0272-3646.26.3.177>
- Lépp, I. and Rajkay, Ö., 1957: Repülőterei éjszakai alkalmasságának kérdései. *Időjárás* 61, 278–284. (In Hungarian)
- Martin, D.E., 1972: Climatic Presentations for Short-Range Forecasting Based on Event Occurrence and Reoccurrence Profiles, *J. Appl. Meteor.* 11, 1212–1223. [https://doi.org/10.1175/1520-0450\(1972\)011<1212:CPFSRF>2.0.CO;2](https://doi.org/10.1175/1520-0450(1972)011<1212:CPFSRF>2.0.CO;2)
- Meyer, M.B. and Lala, G.G., 1990: Climatological Aspects of Radiation Fog Occurrence at Albany, New York. *J. Climate* 3, 577–586. [https://doi.org/10.1175/1520-0442\(1990\)003<0577:CAORFO>2.0.CO;2](https://doi.org/10.1175/1520-0442(1990)003<0577:CAORFO>2.0.CO;2)
- National Oceanic and Atmospheric Administration, 1995: Surface weather observations and reports. Federal Meteorological Handbook No. 1.
- Peace, R.L. Jr., 1969: Heavy-Fog Regions In The Conterminous United States. *Mon. Weather Rev.* 97, 116–123. [https://doi.org/10.1175/1520-0493\(1969\)097<0116:HRITCU>2.3.CO;2](https://doi.org/10.1175/1520-0493(1969)097<0116:HRITCU>2.3.CO;2)
- Probáld, F., 1965: Városi hatások a látástávolságra Budapest. *Időjárás* 69, 370–374. (In Hungarian)
- Scherrer, S.C. and Appenzeller, C., 2014: Fog and low stratus over the Swiss Plateau—a climatological study. *Int. J. Climatol.* 34, 678–686. <https://doi.org/10.1002/joc.3714>
- Shanyengana, E.S., Henschel, J.R., Seely, M.K., and Sanderson, R.D., 2002: Exploring fog as a supplementary water source in Namibia. *Atmos. Res.* 64, 251–259. [https://doi.org/10.1016/S0169-8095\(02\)00096-0](https://doi.org/10.1016/S0169-8095(02)00096-0)
- Szalai, S., Auer, I., Hiebl, J., Milkovich, J., Radim, T., Stepanek, P., Zahradnicek, P., Bihari, Z., Lakatos, M., Szentimrey, T., Limanowka, D., Kilar, P., Cheval, S., Deak, Gy., Mihic, D., Antolovic, I., Mihajlovic, V., Nejedlik, P., Stastny, P., Mikulova, K., Nabyvantes, I., Skyryk, O., Krakovskaya, S., Vogt, J., Antofie, T., and Spinoni, J., 2013: Climate of the Greater Carpathian Region. Final Technical Report. <http://www.carpatclim-eu.org/pages/home/> . CARPATCLIM Database © European Commission – JRC.
- Tardif, R. and Rasmussen, R.M., 2007: Event-Based Climatology and Typology of Fog in the New York City Region. *J. Appl. Meteorol. Climatol.* 46, 1141–1168. <https://doi.org/10.1175/JAM2516.1>
- Tuba, Z. and Botyán, Zs., 2018: Fuzzy logic-based analogue forecasting and hybrid modelling of horizontal visibility. *Meteorol. Atmosph. Phys.* 130, 265–277. <https://doi.org/10.1007/s00703-017-0513-1>
- Wang, J.L., Li, S.M., Liu, X.L., and Wu, X.J., 2010: An analysis of the fog distribution in Beijing for the 2001–2005 period using NOAA and FY data. *Atmos. Res.* 96, 575–589. <https://doi.org/10.1016/j.atmosres.2010.01.007>
- Wantuch, F., 2001: Visibility and fog forecasting based on decision tree method. *Időjárás* 105, 29–38.
- Witiw, M.R. and Baars, J.A., Terabeam Corporation, 2003: Long Term Climatological Changes In Fog Intensity And Coverage. Proc. 14th Symp. Global Change and Climate Variations, Am. Meteor. Soc., Long Beach, CA.
- WMO, 2011: Manual on codes, international codes. Technical Report, World Meteorological Organization, Geneva Switzerland.

INSTRUCTIONS TO AUTHORS OF *IDŐJÁRÁS*

The purpose of the journal is to publish papers in any field of meteorology and atmosphere related scientific areas. These may be

- research papers on new results of scientific investigations,
- critical review articles summarizing the current state of art of a certain topic,
- short contributions dealing with a particular question.

Some issues contain “News” and “Book review”, therefore, such contributions are also welcome. The papers must be in American English and should be checked by a native speaker if necessary.

Authors are requested to send their manuscripts to

Editor-in Chief of IDŐJÁRÁS
P.O. Box 38, H-1525 Budapest, Hungary
E-mail: journal.idojaras@met.hu

including all illustrations. MS Word format is preferred in electronic submission. Papers will then be reviewed normally by two independent referees, who remain unidentified for the author(s). The Editor-in-Chief will inform the author(s) whether or not the paper is acceptable for publication, and what modifications, if any, are necessary.

Please, follow the order given below when typing manuscripts.

Title page should consist of the title, the name(s) of the author(s), their affiliation(s) including full postal and e-mail address(es). In case of more than one author, the corresponding author must be identified.

Abstract: should contain the purpose, the applied data and methods as well as the basic conclusion(s) of the paper.

Key-words: must be included (from 5 to 10) to help to classify the topic.

Text: has to be typed in single spacing on an A4 size paper using 14 pt Times New Roman font if possible. Use of S.I.

units are expected, and the use of negative exponent is preferred to fractional sign. Mathematical formulae are expected to be as simple as possible and numbered in parentheses at the right margin.

All publications cited in the text should be presented in the *list of references*, arranged in alphabetical order. For an article: name(s) of author(s) in Italics, year, title of article, name of journal, volume, number (the latter two in Italics) and pages. E.g., *Nathan, K.K.*, 1986: A note on the relationship between photo-synthetically active radiation and cloud amount. *Időjárás* 90, 10–13. For a book: name(s) of author(s), year, title of the book (all in Italics except the year), publisher and place of publication. E.g., *Junge, C.E.*, 1963: *Air Chemistry and Radioactivity*. Academic Press, New York and London. Reference in the text should contain the name(s) of the author(s) in Italics and year of publication. E.g., in the case of one author: *Miller* (1989); in the case of two authors: *Gamov* and *Cleveland* (1973); and if there are more than two authors: *Smith et al.* (1990). If the name of the author cannot be fitted into the text: (*Miller*, 1989); etc. When referring papers published in the same year by the same author, letters a, b, c, etc. should follow the year of publication. DOI numbers of references should be provided if applicable.

Tables should be marked by Arabic numbers and printed in separate sheets with their numbers and legends given below them. Avoid too lengthy or complicated tables, or tables duplicating results given in other form in the manuscript (e.g., graphs). *Figures* should also be marked with Arabic numbers and printed in black and white or color (under special arrangement) in separate sheets with their numbers and captions given below them. JPG, TIF, GIF, BMP or PNG formats should be used for electronic artwork submission.

More information for authors is available: journal.idojaras@met.hu

Published by the Hungarian Meteorological Service

Budapest, Hungary

INDEX 26 361

HU ISSN 0324-6329